TÉCNICO LISBOA

Development and testing of a novel tri-rotor configuration for application in a fixed wing VTOL aircraft

António Augusto Lopes do Arco

Thesis to obtain the Master of Science Degree in

Aerospace Engineering

Supervisors: Dr. José Lobo do Vale
Prof. Afzal Suleman

Examination Committee

Chairperson: Prof. Filipe Szolnoky Cunha
Supervisor: Prof. Afzal Suleman
Member of the Committee: Prof. Pedro Vieira Gamboa

December 2022

”The higher we soar, the smaller we appear to those who cannot fly.”

Friedrich Nietzsche

Acknowledgments

This thesis marks the ending of a five year journey to obtain my degree in aerospace engineering. Although many times the challenges were intense, I was fortunate enough to have never walked alone.

I would first like to thank Professor Afzal Suleman, who gave me the opportunity to do my thesis research at the Center for Aerospace Research of the University of Victoria in Canada. It was truly an unique opportunity and a privilege to take part in such an exciting project and to work alongside an amazing team, who helped me not only throughout the various stages of my research but also to grow as an engineer and as an individual. I would like to thank particularly to John Rafaelli, for accepting the responsibility of piloting the test vehicle and for all of the valuable inputs throughout its development, and to Sean Bazzocchi for helping me to get started in the field of system identification.

A special thank you goes to my thesis co-supervisor, Dr. José Vale, not only for sharing his vast knowledge on the various matters of aircraft development with me, allowing me to become a better engineer, but mostly for his orientation and dedication in making sure that my thesis project was successful and that I learned as much as possible in the process. It was a true privilege.

Thank you to all of my friends, from the ones which have been with me for years to the ones I made in Canada and that will accompany me for life. This journey would not have been the same without you.

I would like to thank my girlfriend, for always pushing me to challenge myself, to go further, to grow and for the unconditional love and support. I am a better person because of you.

Finally, I have to thank my family: my cousin, my uncles, my grandparents and specially my brother, for always being there for me and helping me realize that there is more to life than black and white.

A special thank you is due to my parents for they have raised me to be the person I am today, with unwavering kindness and support, always allowing me to fly as high as I want.

Declaration

I declare that this document is an original work of my own authorship and that it fulfills all the requirements of the Code of Conduct and Good Practices of the Universidade de Lisboa.

Resumo

A versatilidade das aeronaves de descolagem e aterragem vertical (VTOL) tem levado a um aumento da procura de novas configurações destes veículos, nomeadamente nas áreas de Mobilidade Aérea Urbana e militar. Nesta última, os sistemas VTOL são particularmente interessantes quando aplicados a Veículos Aéreos Não Tripulados (VANTs), permitindo a sua operação independentemente da localização ou infraestruturas existentes.

Nesta tese, é apresentada uma nova configuração de aeronave tri-rotor, sendo feita a prova de conceito das capacidades de voo pairado e horizontal, de modo a determinar a sua aeronavegabilidade e a viabilidade da sua aplicação num futuro VANT VTOL de asa fixa.

Primeiramente, o modelo da dinâmica de voo (FDM) do veículo foi deduzido, um controlador projetado em Simulink e estudos paramétricos realizados para determinar condições de trim em voo pairado. Seguidamente, um controlador foi obtido em PX4 e afinado. Depois, foi projetado um veículo de teste, com enfoque nos mecanismos de inclinação dos rotores dianteiros e traseiro, cujo desempenho foi depois avaliado e a sua atuação mapeada. Foi também feito um estudo sobre a perda de eficiência ($\sim 19\%$ em voo pairado) decorrente da introdução de uma caixa de velocidades no sistema do rotor traseiro. Posteriormente, testes de voo que levaram à prova de conceito e à recolha de dados foram feitos.

Por fim, dois métodos de identificação de sistemas (abordagem baseada em tempo e em resposta em frequência) foram usados para obter modelos. A primeira abordagem conseguiu replicar apenas $2s$ do voo de validação, enquanto a posterior conseguiu replicá-lo inteiramente.

Palavras-chave: Descolagem e Aterragem Vertical, Veículo Aéreo Não Tripulado, Nova configuração, Modelo da Dinâmica de Voo, Identificação de sistema

Abstract

The versatility of Vertical Take-Off and Landing (VTOL) aircraft has led to an increase in demand for such configurations for Urban Air Mobility and military applications. For the latter, VTOL systems are particularly interesting when applied to Unmanned Aerial Vehicles (UAVs), allowing for their deployment irrespective of location and existent infrastructure.

In this thesis, a new configuration of tri-rotor aircraft is presented and the proof of concept for hovering and forward flight capabilities has been performed to determine its airworthiness and the feasibility of applying the concept to a fixed-wing VTOL UAV.

First, the flight dynamics model (FDM) of the vehicle configuration was developed, a Simulink controller was designed, and parametric studies were conducted to determine the trim conditions in hover. Later, a PX4 autopilot was obtained and tuned. Then, the test vehicle was designed, with particular focus on the tilting mechanisms of the front and rear rotors, which were tested to access their performance and map their actuation. A study on the loss of efficiency ($\sim 19\%$ in hover) arising from introducing a gearbox in the rear rotor system was performed. Next, flight tests were performed for evaluation and validation of the proposed concept.

Finally, two system identification methods (time-based and frequency-response approaches) were used to obtain dynamic models for model validation. The first approach was able to replicate $2s$ of the flight while the latter was able to replicate it entirely.

Keywords: Vertical Take-Off and Landing, Unmanned Aerial Vehicle, Novel configuration, Flight Dynamics Model, System Identification

Contents

List of Tables

List of Figures

Nomenclature

Greek symbols

α	Angle of attack.
δ	Control actuator/surface angle.
η	Efficiency.
Γ	Frontal arms' opening angle.
μ	Rear tilt angle.
Ω	Angular velocity.
ω	Angular rates vector.
Φ	Attitude vector.
ϕ	Roll angle.
ψ	Yaw angle.
ρ	Density.
σ	Normal stress.
τ	Shear stress.
θ	Pitch angle.

Roman symbols

b	Wing span.
c	Chord.
C_D	Coefficient of drag.
C_L	Coefficient of lift.
C_M	Coefficient of moment.
D	Drag.

D Lift.

F Force.

f Coefficient of friction.

g Acceleration of gravity.

h Angular momentum.

I Inertia tensor.

k_T Thrust constant.

k_τ Torque constant.

M Moment.

m Mass.

P Power.

S Surface area.

X, Y, Z Position in the inertial frame.

C_{L_α} Lift curve slope.

$C_{L_{i_c}}$ Canard lift curve slope.

$C_{l_{rudder}}$ Roll moment coefficient due to rudder action.

C_{M_α} Pitching moment curve slope.

$C_{M_{i_c}}$ Pitching moment curve slope due to canard incidence.

$C_{N_{rudder}}$ Yaw moment coefficient due to rudder action.

p, q, r Angular velocity Cartesian components.

u, v, w Velocity Cartesian components.

V Velocity vector.

Subscripts

0 Zero angle of attack conditions.

a Aerodynamic.

$arms$ Frontal arms.

b Body.

c Canard.

f Fuselage.

g Gravity.

$gust$ Gust.

$gyro$ Gyroscopic.

L, M, N Cartesian moment components.

p Propulsion.

r Rudder, rear.

w Wing.

x, y, z Cartesian components.

Superscripts

– Average.

T Transpose.

Glossary

CAD	Computer-Aided Design
CCW	Counterclockwise
CG	Center of Gravity
CIFER	Comprehensive Identification from Frequency Responses
CW	Clockwise
CfAR	Center for Aerospace Research
DOF	Degrees of Freedom
DRDC	Defense Research and Development Canada
ESC	Electronic Speed Controller
FC	Flight Controller
FDM	Flight Dynamics Model
ICE	Internal Combustion Engine
LTI	Linear Time Invariant
MAD	Magnetic Anomaly Detection
MIMO	Multiple Input Multiple Output
MTOM	Maximum Take-Off Mass
MTOW	Maximum Take-Off Weight
NED	North East Down
PWM	Pulse-Width Modulation
QA	Quaternion Aerospace
QGC	QGroundControl
RC	Remote Control
ROV	Remotely Operated Vehicle
SID	System Identification
SISO	Single Input Single Output
UAV	Unmanned Aerial Vehicle
UVic	University of Victoria
VTOL	Vertical Take-Off and Landing

Chapter 1

Introduction

1.1 Topic Overview

The term UAV (Unmanned Aerial Vehicle) is used, according to the United States Department of Defense [1], to describe *"aerial vehicles that do not carry a human operator, use aerodynamic forces to provide vehicle lift, can fly autonomously or be piloted remotely, can be expendable or recoverable, and can carry a lethal or nonlethal payload."*

Historically, times of conflict are usually associated with times of great technological advancement. This is true for the case of unmanned aerial vehicles, with the first prototypes being dated to the beginning of Wold War I, in the beginning of the 20^{th} century. This global conflict emerged just a few years after the first recorded flight of an heavier than air aircraft, the Wright Flyer, in 1903, which meant that aircraft technology was still fairly recent and with limited robustness. Nevertheless it became clear, from an early stage of the war, that a great military advantage could be gained from employing aerial vehicles, both manned and unmanned. These first UAVs were developed with the objective of flying towards their targets carrying explosive loads [2]. One example of this kind of aircraft was the Ruston Proctor Aerial Target, created in 1916 by a team led by Archibald Low and tested in 1917. This prototype managed to perform a brief, radio-controlled flight before crashing [3]. Another promising project in the area of UAV development that was developed in the US during 1917 was the Kettering Bug. About fifty exemplars of this aircraft were developed, however it was never used in warfare scenario as it was designed to. In the years that followed the Armistice, the US Army Air Service conducted several tests but further development of this technology was halted due to lack of funding [4].

Meanwhile, the first multi-rotor VTOL aircraft were already being developed, with the first successful manned flight being performed with the Bréguet-Richet Gyroplane No. 1 (Fig. 1.1) in 1907. This vehicle however did not present any type of attitude control, thus being unable to perform free flight [5].

With the end of the first World War the development of unmanned aerial vehicles for military purposes slowed down [6] but some advances were made in the years between the first and the second World Wars. These advances were possible mostly due to the strong development that was being made in the transport aviation industry and that was then used in other areas such as UAV development.

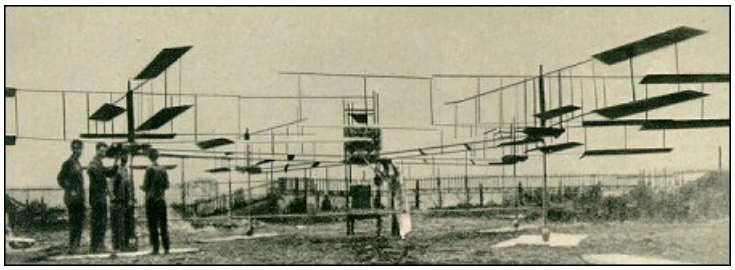

Figure 1.1: Bréguet-Richet Gyroplane No. 1.

Some of these advances were related to radio technology and made the development of more radio-controlled aircraft possible, namely for use as aerial targets for military exercises. One of these projects was the De Havilland DH82B ”Queen Bee”, designed to be a low-cost, radio-controlled, target aircraft with the purpose of providing a realistic scenario for anti-aircraft gunnery training.

During World War II, further advances were made when it comes to UAV technology, namely in the field of guided missiles. However, it was during the Cold War which followed that UAVs gained importance and became paramount in military operations.

With the need to obtain detailed intelligence above hostile territory, countries usually deployed manned aircraft to make stealth reconnaissance missions on hostile airspace. This was common practice for both sides of this conflict. However, it soon became clear, due to situations such as the capture of Captain Francis Gary Powers [7], that the development of unmanned aerial vehicles could help provide intelligence without the need to risk the lives of the pilots which flew reconnaissance aircraft.

Since the Cold War, drone development has experienced several advances, largely due to the ever increasing funding that these projects have attained. However, nowadays, UAVs are no longer a technology used exclusively for military purposes. With the development of new UAV configurations and with the increasing access of the general public to these technologies, the uses for drones are growing every day. Civil applications of drones include aerial photography and videography, transport of cargo, fire detection missions, mine clearing missions [8], search and rescue [9], agriculture and scientific research [10]. Nevertheless, military applications are still the main driver for the development of UAV technology, with the main goal being the gathering of intelligence in the most distinct areas of the world.

When it comes to the existent configurations of VTOL UAVs, nowadays, these can typically be classified according to the number of rotors and their use in the different flight phases. When it comes to number of rotors the most conventional configurations are tri-rotors [11–15], the most common quadcopters [16–21], hexacopters [22] and octacopters [23], with the most various geometries. In terms of use in the different flight phases and way of actuation the classifications for hybrid aircraft usually employed are *tilt-rotor* [14, 24] for aircraft where thrust vectoring is performed through the movement of rotors according to the needs, *tilt-wing* [18], where the rotors are fixed to the wing and rotate in solidarity with it or *Lift+Cruise* [16, 17, 19–21, 23] where the rotors used for the vertical stints are powered off during forward flight, where only the rotors which provide horizontal thrust are used and vice-versa. Nowadays some concepts present hybrid designs as will be the case of the presented vehicle.

1.2 Motivation

One of the hottest topics in the current aerospace engineering paradigm is the development of hybrid configuration aircraft which combine the horizontal flight efficiency of a fixed wing aircraft with the flexibility of performing VTOL and steady hovering manoeuvres that was until recently reserved for rotary wing vehicles such as helicopters and multicopters. With the advent of Urban Air Mobility and the increasing demand, specially by the military, of primarily unmanned aircraft which incorporate the aforementioned characteristics, investigation on the development of novel configurations of VTOL aircraft designs presents an unprecedented level of relevance.

Nevertheless, aircraft design is still a complex task which often relies on the creativity of the designers to obtain new strategies that allow to push the boundaries of aircraft efficiency and versatility to new levels. As so, the main goal of this work is to perform the proof of concept of a ground breaking multi-rotor design that, when applied to an already existent aircraft, will allow for the optimization of its aerodynamic characteristics when in fixed wing mode, while equipping it with the versatility of a VTOL vehicle through the use of thrust vectoring.

1.3 Project Overview and Requirements

This thesis primary purpose is to design, build and fly a novel configuration, tri-rotor, Vertical Take-Off and Landing (VTOL) Unmanned Aerial Vehicle (UAV), proving the airworthiness of the concept. The secondary objective is to apply two system identification (SID) methodologies to the data collected during flight testing, compare the results and obtain a dynamic model from these techniques.

This project is part of the larger Mini-E project which is currently being developed by Quaternion Aerospace (QA) and the Center for Aerospace Research of the University of Victoria (CfAR) through a partnership with the Defense Research and Development Canada (DRDC). Such aircraft is being designed with the ultimate purpose of performing surveillance flights carrying a Magnetic Anomaly Detection sensor (MAD-XR) to detect magnetic anomalies occurring at sea, such as those caused by manned submarines or underwater Remotely Operated Vehicles (ROVs). Since the primary use of this aircraft will be in maritime environment, being deployed from ships, one of the most critical aspects of its design is the requirement of being able to perform VTOL manoeuvres while also maximizing the aircraft's range through the maximization of the L/D (Lift/Drag) ratio and minimization of the vehicle's weight.

Similarly to the fixed wing design, where the main wing was designed to carry around 80% of the aircraft's weight in cruise conditions while the canard holds the remaining 20%, so does the VTOL system present such weight distribution (Fig. 1.2), with each of the frontal rotors being responsible for providing a thrust that accounts for 10% of the overall aircraft's weight while the rear rotor, which will also be providing thrust in horizontal flight, will be responsible for developing 80% of the thrust required to hover. The rear rotor, with its dual purpose, will present a pusher configuration in horizontal flight and a fully upright position in the vertical stints of the mission, thus requiring a custom tilting mechanism to be developed. Furthermore, this tilting mechanism should be designed in a way that it ensures that the

motor itself remains fixed throughout the entire operation of the aircraft since in its final version the rear rotor will be powered by an Internal Combustion Engine (ICE). The tilting action of the rear rotor will also be used to perform the transition between vertical and horizontal flight conditions, a task which will also be addressed in this thesis.

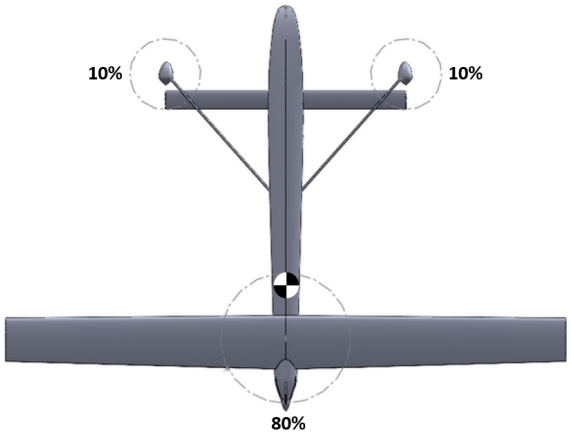

Figure 1.2: Schematic representation of the tri-rotor configuration's thrust distribution under nominal hovering conditions for the Mini-E aircraft.

Meanwhile, the front rotors shall be powered, in all versions, by electric motors, in a way that the final aircraft will most likely present an hybrid propulsion system. These rotors will also be required to tilt in an effort to obtain the thrust vectoring necessary to stabilize this multi-rotor aircraft along the yaw axis in vertical flight conditions, thus requiring the design of a second tilting mechanism.

1.4 Objectives

The present work aims to fulfill the following objectives:

- Physically model the dynamics of a $20/80$ weight distribution tri-rotor, obtaining a preliminary Flight Dynamics Model (FDM);
- Perform trim condition parametric studies using the deduced equations to understand what the aircraft's attitude should be in hovering flight;
- Conceptualize, model, build and test the frontal tilt mechanism for a test vehicle;
- Conceptualize, model, build and test the rear tilt mechanism for a test vehicle, investigating the loss of performance suffered from introducing a gearbox in the system;
- Design and build an appropriate structure for the test vehicle;
- Develop a custom autopilot solution using PX4 [25] for the proposed multi-rotor configuration;
- Perform test-flights to prove the airworthiness of the concept and ability to initiate forward flight;

- Perform test-flights with maneuvering in all axis to collect data from the dynamic behaviour of the aircraft in real world conditions;
- Perform system identification (SID) using two distinct parametric approaches.

1.5 Thesis Outline

Chapter 2

In the theoretical background chapter, a brief overview of the concepts required to develop the presented work will be performed. Firstly, the fundamentals required to develop the preliminary flight dynamics model will be addressed, followed by a short review of tilting mechanisms design penalties (namely loss of efficiency associated to the use of gearboxes) and of some SID methodologies.

Chapter 3

In this chapter, the derivation of the equations that comprise the Flight Dynamics Model is performed and all of the assumptions made are explained. Then, the parametric studies developed to understand the expected trimmed attitude of the aircraft under several flight conditions are presented and discussed. Finally, the development of the custom airframe model for the autopilot using PX4 is addressed.

Chapter 4

This chapter presents the reasoning behind the choices made when it comes to the design of the different mechanisms necessary to fly this aircraft configuration, namely when it came to develop the test vehicle designed to perform the proof of concept flights. The airframe design is also briefly discussed as well as the tests performed to assess both the performance and manner of actuation of both the front and rear tilt mechanisms. A discussion on the loss of efficiency that derives from the introduction of a gearbox between the rear motor and the output (propeller) shaft is also presented.

Chapter 5

In this chapter, the succession of indoor test flights, respective results, and changes made to the vehicle in between them are initially analysed. Then, an overview on the topic of aircraft commissioning and development of test flight and safety procedures is done, describing the steps taken to obtain the required permission to fly the experimental aircraft that was developed outdoors. Finally, an analysis of the different flights performed and respective results is done.

Chapter 6

In this chapter, two distinct system identification (SID) techniques will be used to obtain dynamic models. Both will be parametric methods, with the first, time-based one, being used to further develop the existent, physics based, flight dynamics model. Then a different, transfer-function based, approach

will be followed to obtain an alternative model. A comparison of the dynamic behaviour of the two models against true flight data will also be conducted.

Chapter 7

In the final chapter, a global revision of the work done is presented as well as a final balance of the achievements, discussing possible improvements on the concept and some of the future work that may follow.

Chapter 2

Theoretical Background

In this chapter some theoretical notions needed to better comprehend the problem at hands shall be explored. Firstly the methodology used to develop the flight dynamics model of the tri-rotor will be addressed, followed by a brief approach to possible performance penalties associated to the introduction of a gearbox in the design and finally a brief introduction to the topic of system identification will be done.

2.1 Flight Dynamics Model

2.1.1 Reference Frames

The topic of flight dynamics is related to the study of an aircraft's behaviour when flying. This behaviour, translated into movement, is dependent on the different forces and moments that act upon said aircraft, influencing its velocity and attitude throughout time. In order to facilitate this analysis, the first step is to define reference frames. An usual approach is to use a body reference frame and an Earth reference frame. The later (Earth reference frame) is usually defined using the NED convention (North-East-Down) and is taken as a fixed, inertial frame. The body frame on the other hand is taken as a moving frame with the origin placed on the center of gravity of the aircraft under analysis, the x-axis coinciding with the aircraft's longitudinal axis (pointing forward) and the y-axis pointing to the right. Being a right-hand orthogonal frame, the z-axis points downwards.

The aircraft's position in the world frame is given by a vector of three coordinates, $\mathbf{P_w} = [X\ Y\ Z]^T$ and its attitude is provided by three angular coordinates. This last characterization can be done using either quaternions, which have the advantage of being continuous or the more common Euler angles which present discontinuities but can be more intuitive when dealing with small angles. In this work the latter ones shall be used and thus the aircraft's attitude can be provided by the vector $\mathbf{\Phi} = [\phi\ \theta\ \psi]^T$, where ϕ represents the roll angle, θ the pitch angle and ψ the yaw angle. These angles, when known, allow us to make a transformation of vectors from one reference frame to the other by applying a rotation matrix. For the case of a vector transformation from the Earth reference frame to the body frame the following matrix (2.1), which will be named $\mathbf{R}$, can be applied:

$$\mathbf{R} = \begin{bmatrix} \cos\theta cos\psi & \cos\theta\sin\psi & -\sin\theta \\ \sin\phi\sin\theta\cos\psi - \cos\phi\sin\psi & \sin\phi\sin\theta\sin\psi + \cos\phi\cos\psi & \sin\phi\cos\theta \\ \cos\phi\sin\theta\cos\psi + \sin\phi\sin\psi & \cos\phi\sin\theta\sin\psi - \sin\phi\cos\psi & \cos\phi\cos\theta \end{bmatrix} \tag{2.1}$$

To perform a transformation in the opposite direction the transpose matrix, $\mathbf{R^T}$ should be used.

As for the rotational velocity of the aircraft, this can be described in the body reference frame by $\boldsymbol{\omega} = [p\ q\ r]^T$, where p stands for the roll rate, q for the pitch rate and r for the yaw rate, respectively. These angular rates are related to the Euler angle rates, $\mathbf{\Omega_w} = [\dot{\phi}\ \dot{\theta}\ \dot{\psi}]^T$ (measured in the inertial reference frame) by a rotation matrix, $\mathbf{E}$ (2.2), that allows to transform, once more, from the Earth reference frame to the body reference frame:

$$\mathbf{E} = \begin{bmatrix} 1 & 0 & -\sin\theta \\ 0 & \cos\phi & \sin\phi\cos\theta \\ 0 & -\sin\phi & \cos\phi\cos\theta \end{bmatrix} \tag{2.2}$$

When it comes to linear velocities, the nomenclature of $\mathbf{V} = [u\ v\ w]^T$ shall be used to describe the relative airspeed in the body reference frame and $\dot{\mathbf{P}}_\mathbf{w} = [\dot{X}\ \dot{Y}\ \dot{Z}]^T$ for the aircraft velocity in the inertial reference frame. These vectors can be related to one another by applying the rotational matrix $\mathbf{R}$ previously presented.

2.1.2 Dynamics Equations

In order to characterize the dynamics of the aircraft, some assumptions are made, namely that the aircraft is a rigid body with y-symmetry and that both the total mass and the inertia tensor are constants, assumption which is consistent with the fact that the designed UAV shall have electric propulsion. This allows us to derive the dynamic equations from the Newton-Euler equations for both linear (2.3) and angular momentum (2.4). These equations shall be taken on the body reference frame.

$$\mathbf{F_t} = m\left(\frac{d}{dt}\mathbf{V} + \boldsymbol{\omega}\times\mathbf{V}\right) \tag{2.3}$$

$$\mathbf{M_t} = \mathbf{I_b}\left(\frac{d}{dt}\boldsymbol{\omega} + \boldsymbol{\omega}\times\boldsymbol{\omega}\right) \tag{2.4}$$

In the above equations, $\mathbf{F_t}$ is a vector which stands for the summation of the forces acting upon the body and $\mathbf{M_t}$ for the moments, while m represents the aircraft's mass and $\mathbf{I_b}$ its inertia tensor.

The total force acting upon the body includes the contributions of gravity and aerodynamic forces, as well as the thrust forces generated by the rotors. The total moment vector also accounts for the aerodynamic moments and for the torques that are associated with not only the thrust generated by the rotating propellers in combination with their distance to the aircraft's CG but also with the aerodynamic drag that arises from this rotational motion (drag torque).

In order to obtain both the thrust force generated by each rotor and the torque created due to aerodynamic drag of the rotating propeller, a commonly used assumption [13, 26] was made in which it

was considered that these quantities were related to the square of the angular speed (Ω_n) by the thrust (k_T) and torque (k_τ) constants, which are obtained experimentally. As so, the thrust force and the drag torque magnitudes for a given n motor-propeller pair can be obtained, respectively, with the following expressions:

$$F_{Tn} = k_T {\Omega_n}^2 \tag{2.5}$$

$$M_{\tau n} = k_\tau {\Omega_n}^2 \tag{2.6}$$

2.1.3 Linearization

In an effort to simplify nonlinear physical problems such as the one at hands, a common method is to linearize the dynamic equations. This approach is applicable when one wants to study a body's dynamics around a known equilibrium condition (such as hovering flight), considering that only small perturbations act upon the aircraft. The small perturbation theory states that any given variable of our problem ($\mathbf{X}$) can be taken as the sum of two quantities (2.7), $\mathbf{X_0}$, which is the value that such variable presents when the body is at the equilibrium condition and $\mathbf{\Delta X}$, the perturbation, which is considered to be of a much smaller magnitude than the first.

$$\mathbf{X} = \mathbf{X_0} + \mathbf{\Delta X} \tag{2.7}$$

Despite the obvious advantage of simplifying the problem this approach is not ideal for all applications as linearizing the equations around a certain equilibrium point limits their solutions validity to only the vicinity of said equilibrium point.

2.1.4 State Space Formulation

One of the ways to represent the dynamics of a multi-variable system such as the complex motion of an UAV is to use a state space equation. This is a first order differential equation which for Linear Time Invariant (LTI) systems such as the one that shall be considered, and when disturbances and noise are neglected, can assume the following form:

$$\dot{\mathbf{x}} = \mathbf{A}\mathbf{x} + \mathbf{B}\mathbf{u} \tag{2.8}$$

The studied system is considered as Time Invariant as its response (output) to a given input signal does not vary with time, i.e., a given input provided at a given moment will cause the exact same output to an input of the same kind given at a different moment in time, providing all the conditions are the same. The system is also deemed to be Linear (after performing a linearization of the dynamics equations) since its response for a linear combination of inputs is the same as a linear combination of individual responses to those same, individually provided, inputs.

In equation 2.8, $\mathbf{A}$ represents the dynamics matrix, $\mathbf{x}$ the state vector (2.9), $\mathbf{B}$ the input matrix and $\mathbf{u}$ the input vector. The 12 states considered in the state vector describe the aircraft's linear and angular

velocities ($\mathbf{V}$ and $\boldsymbol{\omega}$, respectively), position ($\mathbf{P_w}$) and attitude ($\mathbf{\Phi}$) in a way that:

$$\mathbf{x} = [\mathbf{V}^T \ \boldsymbol{\omega}^T \ \mathbf{P_w}^T \ \mathbf{\Phi}^T]^T = [u \ v \ w \ p \ q \ r \ X \ Y \ Z \ \phi \ \theta \ \psi]^T \tag{2.9}$$

As for the input vector, this will be defined by the tri-rotor configuration, as it depends on the actuators used. Since the tri-rotor configuration that shall be the target of this work is based on the fourth configuration described in [27], there will be 4 actuation inputs in action during the early VTOL stage of the UAV's mission. These actuation inputs are associated to the three rotors, two at the front and one at the rear and the tilting mechanism of the front rotors, needed to balance the yaw moment generated by having an odd number on propellers. As so, the input vector will have 4 entries, one associated to each actuation input, which are the rotational speed (Ω_n) of each of the three motors (see numbering of figure 2.1), and the tilting angle of the frontal arms (δ_{arms}). This angle is considered to be null when the rotors are pointing upwards and assumes a positive value when tilting in a way that a positive thrust component is created in the y direction (see Figure 3.2). The input vector $\mathbf{u}$ will then be given by:

$$\mathbf{u} = [\Omega_1 \ \Omega_2 \ \Omega_3 \ \delta_{arms}] \tag{2.10}$$

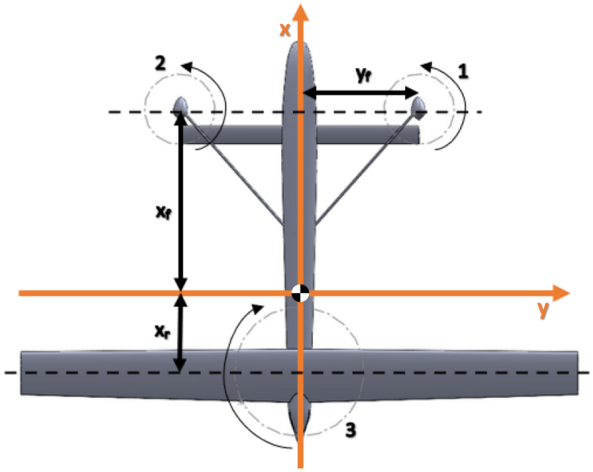

Figure 2.1: Tri-rotor configuration [27].

The propellers' sense of rotation and positioning relative to the aircraft's CG provided in [27] and shown in figure 2.1 shall be used throughout this work, with, x_f and x_r standing for the longitudinal (x) coordinates of the front and rear rotors, respectively and y_f for the y coordinate of rotor 1 in the provided referential. Rotor 2 shall have a y coordinate of $-y_f$ given that the aircraft is symmetric.

2.2 Gearbox Efficiency

Gearboxes allow for the transmission of mechanical power, being commonly used to change the torque or rotational speed of the output shaft relative to the input. Moreover, in some cases, these can also suit the purpose of transmitting power between shafts which are not aligned between them.

Nevertheless, and although indispensable in many applications, gearboxes, as all mechanical systems, present losses. The detailed study of gear and gearbox efficiency is extensive and outside the scope of this document, however, the evolution of gearbox efficiency with the supplied load will need to be addressed in order to better comprehend some of the results that shall be presented later on.

A general trend of increasing gearbox efficiency with the increase in loading has been verified by a large number of researchers [28–35] for various types of gears, gear material and levels of lubrication. This result is mostly related to the reduction of the friction coefficient that usually arises with increasing load and sliding speed of the gear's teeth [36, 37] as a gear system's efficiency and material friction can be related through equation 2.11, where η stands for the efficiency, f for the friction coefficient [38], α for the pressure angle, R_i for the pitch radius of the i gear, l_a for the length of approach and l_f for the length of recess.

$$\eta = 1 - \frac{f}{2\cos\alpha}\left(\frac{1}{R_1} \pm \frac{1}{R_2}\right)\frac{l_a^2 + l_f^2}{l_a + l_f} \tag{2.11}$$

2.3 System Identification

Dynamic models can be classified either as MIMO (Multiple Input Multiple Output) or SISO (Single Input Single Output) and are particularly useful in the field of aerospace engineering as they empower the engineer to perform studies on the aircraft behaviour under different flight scenarios (to study, for example, the aircraft's stability characteristics), develop flight controllers or piloting simulators.

These models can either be obtained through the development of a physical FDM or through the use of SID techniques. These two options present themselves as alternative but also complementary FDM development strategies, particularly in the initial stages of aircraft development.

In the design phase, the creation of an initial physical FDM, even though laborious, is usually unavoidable as to perform preliminary studies on the dynamics of the developing aircraft. However, even in this stage, SID techniques can be used to model certain components such as servos or motors (when appropriate data is available) instead of manually modeling each actuator's dynamics. This can limit the amount of assumptions made, introducing "real world data" into this otherwise solely theoretical model, thus enhancing its validity towards simulating the actual aircraft while also reducing the time and effort required to obtain a satisfactory model. This is particularly relevant when dealing with a novel configuration, where the use of historic data is either impossible or at the very least provides coarse approximations, introducing uncertainty in the model.

Moreover, physics based FDMs are usually modular, being composed by the aggregate of several, smaller models (aerodynamics, structure, actuators, ...). While it is possible to relate such models among themselves, this is, once again, often based on assumptions and approximations which can bring further imprecision to the overall aircraft representation. The lumped models obtained through system identification on the other hand, by being obtained from the relation between the inputs and the outputs of the entire system, can provide an accurate description of the overall behaviour of the vehicle instead of focusing on the dynamics of each subsystem. As so, in the later stages of the project

development, SID techniques can still be used to further develop the physics based FDM or, instead, be used as an alternative method of relating, for example, the control inputs to the outputs, such as attitude change, of the aircraft.

In short and citing *Tischler* and *Remple*, in *Aircraft and Rotorcraft System Identification* [39]: *"Aircraft system identification is a highly versatile procedure for rapidly and efficiently extracting accurate dynamic models of the aircraft from the measured response to specific control inputs."*

In order to obtain the required data to perform system identification, test flights must be conducted, in a way that only an already airworthy aircraft can be the subject of SID techniques. These flights usually include certain sets of manoeuvres (Fig. 2.2) which are used to excite dynamics of interest. Usually such requests are applied to each individual attitude axis of the aircraft at a time in order to obtain separation between each axis' dynamics. However, this is sometimes not possible due to the occurrence of coupling between axis. The most commonly used manoeuvres are the *doublets* and the *chirps* (or *frequency sweeps*).

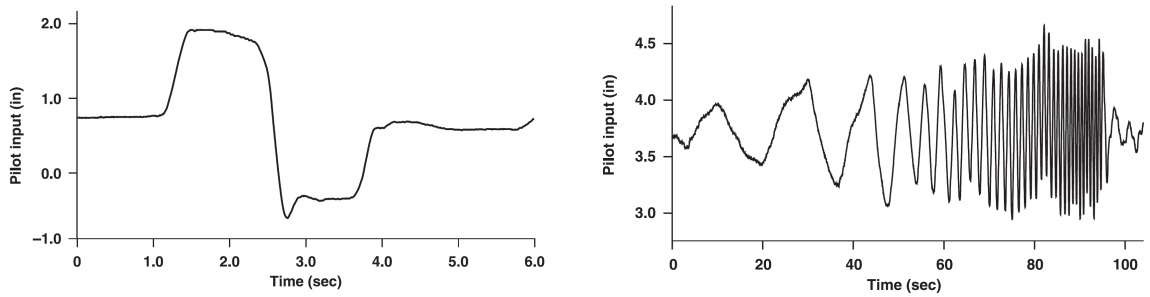

(a) Doublet (b) Chirp

Figure 2.2: Graphic representation of the typical *Doublet* and *Chirp* manoeuvres [39].

System identification can be performed using parametric or non-parametric methods. Parametric SID techniques provide parametric models, outputting values for a specific set of intelligible variables and being usually used when a physical flight dynamics model already exists or some preliminary insight into the dynamics of the vehicle is available. In this case, the inputs and outputs of the system are used to obtain values for unknowns defined by the user, hopefully enhancing the fitment of the FDM's simulated dynamics to a set of flight test results. Transfer-function, frequency-response, based system identification techniques are also included in this category. Meanwhile, non-parametric system identification techniques allow to obtain models which enclose the key aspects of the dynamics of the vehicle without providing intelligible values. This is useful for applications where the turnaround time is limited and the objective is to acquire a model which properly describes the dynamics of the aircraft in flight without the need to dive into the labour intensive task of elaborating the existing physical FDM.

Nowadays, system identification can be performed through various approaches, either parametric or non-parametric, using a wide variety of algorithms, from neural network based programs [40, 41], where a black box model is obtained, to comprehensive algorithms which provide state space or transfer function estimations that can be interpreted by the engineer [42, 43].

Chapter 3

Flight Dynamics Model

When presenting a novel configuration for an aircraft, such as the one at hands, a thorough study of the expected dynamics is an unavoidable step. It is also important to take into account the type of mission for which the developed aircraft is designed for. In our case, the conceptualized vehicle is a Vertical Take-Off and Landing UAV, with a tri-rotor configuration. The dynamics of the aircraft in horizontal flight conditions have already been studied before by Diogo Tomás in [44]. The vertical flight stages dynamics have also been addressed previously by Sara Pedro in [27] but for the current $50/50$ quadrotor configuration (Figure 3.1).

Figure 3.1: Current iteration of the Mini-E aircraft (configuration 1).

In this chapter the development of the flight dynamics model for the future tri-rotor configuration shall be explored. The development process will be explained, as well as the choices made when it comes to approximations and assumptions. Afterwards, the implementation of a custom configuration controller in $PX4$ will be addressed. This implementation is necessary because of the unconventional configuration being developed, which prevents the use of a pre-made aircraft airframe model such as the ones already available in the $PX4$ GitHub repository.

3.1 Dynamics Equations

As stated before, the object of this study is a novel VTOL UAV configuration. As so, it is not possible to analyze the dynamics of the vehicle in the vertical stages of flight in the same way as it is commonly

done for other multi-rotor aircraft. More conventional multi-rotor aircraft, namely tri-rotors, present slender airframes which usually allow for neglecting the influence of aerodynamic forces in their dynamic behaviour. However, for the vehicle in analysis, this is not the case. Since it was designed for long range flight, it presents aerodynamic surfaces, such as a wing, canard, and aerodynamic control surfaces that can influence the aircraft's behavior even in vertical flight mode. The influence of the fuselage's area is also not negligible, in a way that all of the contributions of aerodynamic forces and moments acting on the aircraft need to be taken into account in the final dynamics model.

It shall then be considered that the aircraft is subjected to three types of forces - Aerodynamic, Propulsive and Gravitational - and also to the associated moments. Gyroscopic effects due to rotation of the rotors and the aircraft's change in attitude will also be taken into account.

By taking equations 2.3 and 2.4 and considering the aforementioned contributions of forces and moments, one can obtain the following set of equations:

$$\begin{cases} F_{x_a} + F_{x_{prop}} + F_{x_g} = m(\dot{u} + qw - rv) \\ F_{y_a} + F_{y_{prop}} + F_{y_g} = m(\dot{v} + ru - pw) \\ F_{z_a} + F_{z_{prop}} + F_{z_g} = m(\dot{w} + pv - uq) \\ M_{x_a} + M_{x_{prop}} + M_{x_{gyro}} = I_{xx}\dot{p} - I_{xz}(\dot{r} + pq) + qr(I_{zz} - I_{yy}) \\ M_{y_a} + M_{y_{prop}} + M_{y_{gyro}} = I_{yy}\dot{q} + I_{xz}(p^2 - r^2) + pr(I_{xx} - I_{zz}) \\ M_{z_a} + M_{z_{prop}} + M_{z_{gyro}} = I_{zz}\dot{r} + I_{xz}(qr - \dot{p}) + pq(I_{yy} - I_{xx}) \end{cases} \tag{3.1}$$

where subscript "a" indicates the contribution of aerodynamic forces and moments, "$prop$" the contributions due to the propulsive system, "g" the contribution of gravity and "$gyro$" the moments due to gyroscopic effects. The remaining variables follow the conventions defined earlier in 2.1.

3.1.1 Propulsive Forces and Moments

The forces and moments which relate to the generation of thrust by the rotors (identified earlier with subscript $prop$) are considered to be a function of the motor/propeller pair rotational speed, Ω_n, as defined in equations 2.5 and 2.6. It is important to note that when one defines a moment as being related to the "generation of thrust", this can apply not only to a torque caused by the application of a thrust force at a given distance from the center of gravity but also to the torque that is generated by the aerodynamic drag of the rotating propellers.

In order to define these contributions, it is important to once again consider the rotor layout as well as the sense of rotation of each propeller as this will influence the sense of the drag torque generated by each rotor. Thus, the layout provided in 2.1.4 will be considered. It is also important to carefully analyze the rotation mechanism of the front rotors as well as the arms' orientation since variations in this layout can greatly influence the tri-rotor's dynamics. A schematic representation of the right frontal arm configuration is provided in Figure 3.2, with the three coordinate axis (X', Y' and Z') being aligned with the respective axis (X, Y and Z) of the body reference frame. Note that both the left and right arms

rotate simultaneously in the same direction with the axis of rotation being contained in the $X'Y'$ plane.

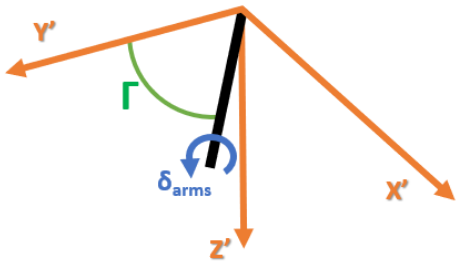

Figure 3.2: Right frontal arm rotation angles.

Contrarily to what is verified for a non-tilt multi-rotor configuration, it is possible to have thrust force contributions in both the X and Y directions with this configuration. Thus, the following expressions can be derived to obtain the different components of forces and moments generated by tilting the rotors and taking Figure 2.1 as a reference. Note that in the equations presented in 3.2 it was considered that the CG of the aircraft and the three rotors are contained in the same *XY* plane.

$$\begin{cases} F_{x_{prop}} = (-k_{T1}\Omega_1^2 + k_{T2}\Omega_2^2)\sin\delta_{arms}\cos\Gamma + (k_{T3}\Omega_3^2)\cos\mu \\ F_{y_{prop}} = (k_{T1}\Omega_1^2 + k_{T2}\Omega_2^2)\sin\delta_{arms}\sin\Gamma \\ F_{z_{prop}} = -(k_{T1}\Omega_1^2 + k_{T2}\Omega_2^2)\cos\delta_{arms} - (k_{T3}\Omega_3^2)\sin\mu \\ M_{x_{prop}} = (-k_{T1}\Omega_1^2 + k_{T2}\Omega_2^2)y_f\cos\delta_{arms} + (k_{\tau 1}\Omega_1^2 - k_{\tau 2}\Omega_2^2)\sin\delta_{arms}\cos\Gamma + (k_{\tau 3}\Omega_3^2)\cos\mu \\ M_{y_{prop}} = (k_{T1}\Omega_1^2 + k_{T2}\Omega_2^2)x_f\cos\delta_{arms} - (k_{T3}\Omega_3^2)x_r\sin\mu - (k_{\tau 1}\Omega_1^2 + k_{\tau 2}\Omega_2^2)\sin\delta_{arms}\sin\Gamma \\ M_{z_{prop}} = (k_{T1}\Omega_1^2 + k_{T2}\Omega_2^2)x_f\sin\delta_{arms}\sin\Gamma + (k_{T1}\Omega_1^2 + k_{T2}\Omega_2^2)y_f\sin\delta_{arms}\cos\Gamma + \\ \qquad +(k_{\tau 1}\Omega_1^2 + k_{\tau 2}\Omega_2^2)\cos\delta_{arms} - (k_{\tau 3}\Omega_3^2)\sin\mu \end{cases} \tag{3.2}$$

In addition to the variables already mentioned, the tilting angle of the rear rotor is also taken into account in these equations, being represented by the letter μ. In vertical flight mode this variable shall assume the value of $90°$ (or $\frac{\pi}{2}$ in rad) and in horizontal flight mode $0°$ (or $0\,rad$).

In these equations, the distances x_f, x_r and y_r will be the ones already defined by Sara Pedro in [27], who mentioned that these measurements should be the same as the ones defined for configurations 2 and 3 of the Mini-E UAV. As so, the values provided in Table 3.1 were considered:

Table 3.1: Rotor distances from the center of gravity of the aircraft [27].

Distance [m]	
x_f	0.891
x_r	0.222
y_f	0.483

3.1.2 Aerodynamic Forces and Moments

As referred earlier in this chapter, the vehicle in analysis has a configuration which prevents one from neglecting the influence of aerodynamic forces and moments on its dynamics. However, only a simplified analysis will be done, neglecting for example the influence of ground effect on the aircraft's dynamics in VTOL maneuvers. Nevertheless, the contribution of the lifting surfaces and fuselage to the overall lift and drag forces will be taken into account, since one of the objectives of this work is to perform a parametric analysis on the behavior of the aircraft in hover when exposed to constant gusts and initiating forward flight, rendering it necessary to take into account such aerodynamic contributions to the general dynamics of the vehicle.

The drag force estimation was divided into three components, one aligned with each of the body's reference frame axis. Along the longitudinal direction, the value of C_{D_0} already determined in [44] for the 4^{th} configuration of the proposed UAV was used. The induced drag was also considered since the generation of lift by the aerodynamics surfaces is not negligible when dealing with gust speeds close to the stall speed of the aircraft. For determining the lateral drag coefficient the assumptions that the wing and canard contributions were negligible and that the fuselage could be approximated to a cylinder were made. For the vertical component the fuselage contribution was considered as well as the wings and canard's by considering that these surfaces could be approximated by flat plates perpendicular to the direction of the flow.

As for the reference areas used in these computations, these were the canard and wing's projected area and half of the surface area of a cylinder with the length and approximate radius of the designed fuselage [27, 44]. These reference areas are provided in Table 3.2 where S_c, S_w and S_f are the canard's, wing's and fuselage's reference areas used in the computation of the drag and lift contributions, respectively.

Table 3.2: Reference surface areas.

Component	**Surface area [m^2]**
Canard	0.08
Wings	0.50
Fuselage	0.61

When it comes to lift, it was considered to have a contribution in the body frame's z-axis negative direction whenever the aircraft faced frontal gusts. A similar approach was considered when dealing with the pitching moment since the data available only allowed to characterize the aircraft's behaviour in these limited conditions. All of the other gust components, when present, were considered to contribute solely with drag to the model, with the possibility of generating some moments according to the direction of the gust.

Starting by the definition of the lift coefficient, this was computed using the following formula:

$$C_L = C_{L0} + C_{L\alpha}\alpha + C_{Li_c}\delta_c \tag{3.3}$$

where C_{L0} is the lift coefficient of the aircraft at a null angle of attack, $C_{L\alpha}$ the lift curve slope in the linear region, α the angle of attack, C_{Li_c} the slope of the curve which denotes the lift generated by the canard with varying incidence and δ_c the canard's incidence.

As for the drag coefficient of the aircraft when facing frontal gusts, the general expression usually employed for forward flight [45] was considered:

$$C_D = C_{D0} + \left(\frac{{C_{L\alpha}}^2}{\pi e \frac{b^2}{S_w}} \right) \alpha^2 + C_{Di_c} \delta_c \tag{3.4}$$

where C_{D0} is the drag coefficient of the aircraft at a null angle of attack, e the Oswald efficiency factor, considered to be 0.8 [46], b stands for the aircraft's wing span and S_w for the wing's area as mentioned above. By knowing C_{Di_c} and δ_c, it is also possible to determine the canard's contribution to the total drag coefficient.

As referred, these formulas can be used in the case of frontal gusts. However, gust components from other directions must also be taken into account. For those, the value of C_{D0} considered was 0.04, $C_{Dw} = C_{Dc} = 1.28$, which denote the drag coefficient of a flat plate perpendicular to the flow, and that shall be used in the computation of drag developed by the wings and canard exposed to vertical components of gusts [47] and C_{Df}, denoting the drag coefficient of the fuselage exposed to a perpendicular flow was taken as 1.2 [48].

Having defined these constants, it is now possible to compute the drag components. In Table 3.3 the formulas employed to determine the magnitude of the drag force according to the type of gust affecting the aircraft in hover can be consulted.

Table 3.3: Drag equation used according to the gust directions.

Direction of the gust	**Equation**
Frontal	$D = \frac{1}{2}\rho S_w {u_{gust}}^2 C_D$
Rear	$D = \frac{1}{2}\rho S_w {u_{gust}}^2 C_{D0}$
Upward	$D = \frac{1}{2}\rho {w_{gust}}^2 \left((S_w + S_c) C_{Dw} + S_f C_{Df} \right)$
Downward	
Left	$D = \frac{1}{2}\rho S_f {v_{gust}}^2 C_{Df}$
Right	

In these equations u_{gust}, v_{gust} and w_{gust} stand for the decomposition of components of the gusts according to the three coordinate axis of the body's reference frame.

As previously mentioned in this text, the lift force contribution was only considered under the circumstance of a frontal gust component existing. In that case, the following formula was employed:

$$L = \frac{1}{2}\rho S_w u_{gust}^2 C_L \tag{3.5}$$

where C_L comes from equation 3.3, ρ is the air density, S_w the wing area and u_{gust} the gust magnitude along x.

When it comes to the moments due to aerodynamic forces acting upon the aircraft, the analysis made considered that in the case of longitudinal gusts the drag forces would not generate any moment upon the body due to symmetry. Nevertheless, for frontal gusts the usual formulas for computing the pitching moment in forward flight were used (3.6, 3.7), where $\overline{c}$ represents the average wing chord.

$$C_M = C_{M0} + C_{M\alpha}\alpha + C_{M_{i_c}}\delta_c \tag{3.6}$$

$$M = \frac{1}{2}\rho {u_{gust}}^2 S_w \overline{c} C_M \tag{3.7}$$

For the case of lateral gusts, a yaw moment was considered to be developed under the premise that the drag force generated acted at the center of the fuselage's lateral area, whereas the center of gravity of the aircraft is to be located further aft. This way, an arm develops between these two point and the drag force acting on the fuselage ultimately causes a yaw moment around the $z-axis$ to occur, in a way that:

$$M_{DN} = \frac{1}{2}\rho v_{gust}^2 C_{Df} S_f d_f \tag{3.8}$$

where d_f stands for the longitudinal distance between the point of application of the resultant of the drag forces acting on the fuselage and the aircraft's CG, which assumes a value of $0.438\,m$.

In the case of vertical gusts a similar approach was considered, but this time also taking into account the contribution of the lifting surfaces (considered as flat plates) to the development of a pitching moment:

$$M_{DM} = \frac{1}{2}\rho w_{gust}^2 \left((S_c d_c - S_w d_w) C_{Dw} + C_{Df} S_f d_f\right) \tag{3.9}$$

where d_c and d_w are the analogue quantities of d_f but for the distances between the canard and wing's mid chord and the aircraft's CG, assuming values of $0.802\,m$ and $0.190\,m$, respectively.

Two systems of equations were then considered to compute these aerodynamic contributions. The distinctive characteristics are related to the direction of the x gust component relative to the aircraft, as this direction will influence the drag model used and also the contribution of lift being present or not, as well as the contribution of the pitching moment due to this generation of lift. The following equations (3.10) represent the aerodynamic contribution to the general force and moment balance when the gusts have a longitudinal null or frontal component, relative to the aircraft.

$$\begin{cases} F_{xa} = -\frac{1}{2}\rho S_w u_{gust}^2 C_D \\ F_{y_a} = -\frac{1}{2}\rho S_f v_{gust}|v_{gust}| C_{Df} \\ F_{za} = -\frac{1}{2}\rho w_{gust}|w_{gust}| \left((S_w + S_c) C_{Dw} + S_F C_{Df}\right) - \frac{1}{2}\rho S_w u_{gust}^2 C_L \\ M_{xa} = 0 \\ M_{y_a} = \frac{1}{2}\rho w_{gust}|w_{gust}| \left((S_c d_c - S_w d_w) C_{Dw} + C_{Df} S_f d_f\right) + \frac{1}{2}\rho {u_{gust}}^2 S_w \overline{c} C_M \\ M_{za} = -\frac{1}{2}\rho v_{gust}|v_{gust}| C_{Df} S_f d_f \end{cases} \tag{3.10}$$

where v_{gust} is positive for gusts hitting the aircraft's right flank and negative for the opposite sense and w_{gust} is positive for vertical, upward gusts and negative for downward gusts. Moreover, for the case of aerodynamic contributions when the gusts have a positive longitudinal component (from the rear), the following set of equations is used:

$$\begin{cases} F_{x_a} = \frac{1}{2}\rho S_w u_{gust}^2 C_{D0} \\ F_{y_a} = -\frac{1}{2}\rho S_f v_{gust}|v_{gust}|C_{Df} \\ F_{z_a} = -\frac{1}{2}\rho w_{gust}|w_{gust}|\left((S_w + S_c)C_{Dw} + S_F C_{Df}\right) \\ M_{x_a} = 0 \\ M_{y_a} = \frac{1}{2}\rho w_{gust}|w_{gust}|\left((S_c d_c - S_w d_w)C_{Dw} + C_{Df} S_f d_f\right) \\ M_{z_a} = -\frac{1}{2}\rho v_{gust}|v_{gust}|C_{Df} S_f d_f \end{cases} \tag{3.11}$$

3.1.3 Gravitational Forces

When it comes to accounting for the influence of gravity upon the vehicle's dynamics, it is necessary to define the three components of the gravitational force (one in each coordinate axis of the body frame). These components depend on the aircraft's mass (m), on its attitude ($\Phi = [\phi\ \theta\ \psi]^T$) and on the acceleration of gravity (g) only, yielding the following expressions:

$$\begin{cases} F_{x_g} = -mg\sin\theta \\ F_{y_g} = mg\cos\theta\sin\phi \\ F_{z_g} = mg\cos\theta\cos\phi \end{cases} \tag{3.12}$$

3.1.4 Gyroscopic Moments

In order to take the gyroscopic effects into consideration, a different equation will then be used when it comes to the angular momentum. As so, instead of equation 2.4, another expression shall arise, with the ever-present assumption of a constant inertia tensor as well as of constant rotational speed of the different rotors relative to the aircraft's reference frame [46]:

$$\mathbf{M_t} = \frac{d}{dt}\mathbf{I_b}\boldsymbol{\omega} + \boldsymbol{\omega} \times (\mathbf{I_b}\boldsymbol{\omega} + \mathbf{h}) \tag{3.13}$$

where $\mathbf{h}$ stands for the total angular momentum of all spinning rotors (with the assumption of constant rotational speed) relative to the body reference frame.

Furthermore, from this expression, one can obtain a set of equations which provide the components of the moment in the three body frame's directions due to the existence of such gyroscopic effects [46]:

$$\begin{cases} M_{x_{gyro}} = -h_z q + h_y r \\ M_{y_{gyro}} = h_z p - h_x r \\ M_{z_{gyro}} = -h_y p + h_x q \end{cases} \tag{3.14}$$

In the aforementioned equations (3.14) p, q and r are the angular rates and the h_x, h_y and h_z elements denote the angular momentum of the rotors in the three directions of the local referential. These can be obtained by knowing the rotor's inertia, rotational velocity, orientation and sense of rotation.

In order to obtain said inertia values, some simplifications were made regarding the propellers and the electric motor's rotors. As so, from the data available from the motor and propellers suppliers, an estimation of said inertial values was performed. The propeller's moment of inertia determination was based on the assumption that the blades could be taken as slender rods with a fraction of the propeller's mass (for example in a 3 bladed propeller, 3 rods each with $1/3$ of its total mass) and with the length of the propeller's radius. As for the electric motors moving parts (bell or rotor), they were taken as a hollow cylinder with dimensions and mass given by the supplier's spec sheets.

From these inertial values, and in order to obtain the angular momentum of each propeller-bell pair it is just a matter of multiplying the moment of inertia by the angular velocity of that rotor. This way, one can obtain h_{fr}, h_{fl} and h_r, the angular momentum of the frontal right, left and rear pairs from:

$$h_{nn} = I_{nn}\Omega_i \tag{3.15}$$

With the angular momentum of each rotor defined, it is just a matter of computing the total angular momentum by taking into account the orientation and sense of rotation of the propellers. Hence, the following expressions emerge, employing the same notation as before:

$$\begin{cases} h_x = (h_{fl} - h_{fr})\sin(\delta_{arms})\cos(\Gamma) - h_r cos(\mu) \\ h_y = (h_{fl} + h_{fr})\sin(\delta_{arms})\sin(\Gamma) \\ h_z = -(h_{fl} + h_{fr})\cos(\delta_{arms}) + h_r \sin(\mu) \end{cases} \tag{3.16}$$

3.1.5 Linearization

As previously mentioned in subsection 2.1.3, performing a linearization of nonlinear equations can greatly simplify the resolution of problems such as the study of the aircraft's dynamics around a certain equilibrium point. This is a reasonable approximation for stability studies. As so, in the studied example of hovering flight it is perfectly reasonable to apply the small perturbation theory and thus linearize the equations as the states variations around the equilibrium condition are assumed to be small, i.e., while hovering, the aircraft's attitude variation should be limited to reasonably small angle changes, flight speed should be null or very close to it (considering that gusts may exist), the aircraft's position shall be approximately constant and the angular rates should also remain small.

By applying this small perturbation theory to the dynamics equations introduced in 2.1.2 for the three

directions of the body reference frame, the following expressions arise [49]:

$$\begin{cases} \Delta F_{x_a} + \Delta F_{x_{prop}} + \Delta F_{x_g} = m(\Delta\dot{u} + q_0\Delta w + w_0\Delta q - v_0\Delta r - r_0\Delta v) \\ \Delta F_{y_a} + \Delta F_{y_{prop}} + \Delta F_{y_g} = m(\Delta\dot{v} + u_0\Delta r + r_0\Delta u - p_0\Delta w - w_0\Delta p) \\ \Delta F_{z_a} + \Delta F_{z_{prop}} + \Delta F_{z_g} = m(\Delta\dot{w} + v_0\Delta p + p_0\Delta v - u_0\Delta q - q_0\Delta u) \\ \Delta M_{x_a} + \Delta M_{x_{prop}} + \Delta M_{x_{gyro}} = I_{xx}\Delta\dot{p} - I_{xz}(\Delta\dot{r} + p_0\Delta q + q_0\Delta p) + (I_{zz} - I_{yy})(q_0\Delta r + r_0\Delta q) \\ \Delta M_{y_a} + \Delta M_{y_{prop}} + \Delta M_{y_{gyro}} = I_{yy}\Delta\dot{q} + 2I_{xz}(p_0\Delta p - r_0\Delta r) + (I_{xx} - I_{zz})(p_0\Delta r + r_0\Delta p) \\ \Delta M_{z_a} + \Delta M_{z_{prop}} + \Delta M_{z_{gyro}} = I_{zz}\Delta\dot{r} - I_{xz}\Delta\dot{p} + I_{xz}(q_0\Delta r + r_0\Delta q) + (I_{yy} - I_{xx})(p_0\Delta q + q_0\Delta p) \end{cases} \tag{3.17}$$

where the subscripts a, $prop$ and $gyro$ denote aerodynamic, propulsion and gyroscopic forces and moments respectively and the subscript 0 denotes the value of a given state variable in equilibrium conditions.

However, given that the small perturbation theory is being used, most of the terms in 3.17 will disappear since in hovering conditions (equilibrium state), u_0, v_0, w_0, p_0, q_0 and r_0 are considered as having a magnitude of 0. Therefore, equations 3.17 can be simplified as:

$$\begin{cases} \Delta F_{x_a} + \Delta F_{x_{prop}} + \Delta F_{x_g} = m\Delta\dot{u} \\ \Delta F_{y_a} + \Delta F_{y_{prop}} + \Delta F_{y_g} = m\Delta\dot{v} \\ \Delta F_{z_a} + \Delta F_{z_{prop}} + \Delta F_{z_g} = m\Delta\dot{w} \\ \Delta M_{x_a} + \Delta M_{x_{prop}} + \Delta M_{x_{gyro}} = I_{xx}\Delta\dot{p} - I_{xz}\Delta\dot{r} \\ \Delta M_{y_a} + \Delta M_{y_{prop}} + \Delta M_{y_{gyro}} = I_{yy}\Delta\dot{q} \\ \Delta M_{z_a} + \Delta M_{z_{prop}} + \Delta M_{z_{gyro}} = I_{zz}\Delta\dot{r} - I_{xz}\Delta\dot{p} \end{cases} \tag{3.18}$$

In the case of the propulsive forces and moments equations provided in 3.2, these can also be linearized by the use of the small perturbation theory. In the equations 3.21 that follow, k_{Tn} and $k_{\tau n}$ denote the thrust and torque constant of each n motor and Ω_{0n} the rotational speed of each motor in hovering conditions. These speeds in hovering conditions can be determined based on the desired CG position. Since the designed aircraft should have a $20/80$ thrust distribution, this means that each of the front rotors, under hovering conditions, should produce enough thrust to balance 10% of the aircraft's weight and the rear rotor 80%, in a way that the rotational speed of the front and rear rotors can be given, respectively, by:

$$\Omega_{01} = \Omega_{02} = \sqrt{\frac{0.1mg}{k_{T1,2}}} \tag{3.19}$$

$$\Omega_{03} = \sqrt{\frac{0.8mg}{k_{T3}}} \tag{3.20}$$

As so, the linearized equations for the propulsive forces and moments can assume the following

form:

$$
\begin{cases}
\Delta F_{x_{prop}} = (-2k_{T1}\Omega_{01}\Delta\Omega_1 + 2k_{T2}\Omega_{02}\Delta\Omega_2)(\sin\delta_{arms0}\cos\Gamma)+ \\
\qquad +(-k_{T1}\Omega_{01}^2 + k_{T2}\Omega_{02}^2)(\Delta\delta_{arms}\cos\delta_{arms0}\cos\Gamma) + (2k_{T3}\Omega_{03}\Delta\Omega_3\cos\mu) \\
\Delta F_{y_{prop}} = (2k_{T1}\Omega_{01}\Delta\Omega_1 + 2k_{T2}\Omega_{02}\Delta\Omega_2)(\sin\delta_{arms0}\sin\Gamma)+ \\
\qquad +(k_{T1}\Omega_{01}^2 + k_{T2}\Omega_{02}^2)(\Delta\delta_{arms}\cos\delta_{arms0}\sin\Gamma) \\
\Delta F_{z_{prop}} = -(2k_{T1}\Omega_{01}\Delta\Omega_1 + 2k_{T2}\Omega_{02}\Delta\Omega_2)(\cos\delta_{arms0}) - (2k_{T3}\Omega_{03}\Delta\Omega_3\sin\mu)+ \\
\qquad +(k_{T1}\Omega_{01}^2 + k_{T2}\Omega_{02}^2)(\Delta\delta_{arms}\sin\delta_{arms0}) \\
\Delta M_{x_{prop}} = (-2k_{T1}\Omega_{01}\Delta\Omega_1 + 2k_{T2}\Omega_{02}\Delta\Omega_2)y_f(\cos\delta_{arms0})- \\
\qquad -(-k_{T1}\Omega_{01}^2 + k_{T2}\Omega_{02}^2)y_f(\Delta\delta_{arms}\sin\delta_{arms0})+ \\
\qquad +(2k_{\tau1}\Omega_{01}\Delta\Omega_1 - 2k_{\tau2}\Omega_{02}\Delta\Omega_2)(\sin\delta_{arms0}\cos\Gamma)+ \\
\qquad +(k_{\tau1}\Omega_{01}^2 - k_{\tau2}\Omega_{02}^2)(\Delta\delta_{arms}\cos\delta_{arms0}\cos\Gamma)+ \\
\qquad +(2k_{\tau3}\Omega_{03}\Delta\Omega_3)(\cos\mu) \\
\Delta M_{y_{prop}} = (2k_{T1}\Omega_{01}\Delta\Omega_1 + 2k_{T2}\Omega_{02}\Delta\Omega_2)x_f(\cos\delta_{arms0})- \\
\qquad -(k_{T1}\Omega_{01}^2 + k_{T2}\Omega_{02}^2)x_f(\Delta\delta_{arms}\sin\delta_{arms0})- \\
\qquad -(2k_{T3}\Omega_{03}\Delta\Omega_3)x_r(\sin\mu) - (2k_{\tau1}\Omega_{01}\Delta\Omega_1 + 2k_{\tau2}\Omega_{02}\Delta\Omega_2)(\sin\delta_{arms0}\sin\Gamma)- \\
\qquad -(k_{\tau1}\Omega_{01}^2 + k_{\tau2}\Omega_{02}^2)(\Delta\delta_{arms}\cos\delta_{arms0}\sin\Gamma) \\
\Delta M_{z_{prop}} = (2k_{T1}\Omega_{01}\Delta\Omega_1 + 2k_{T2}\Omega_{02}\Delta\Omega_2)x_f(\sin\delta_{arms0}\sin\Gamma)+ \\
\qquad +(k_{T1}\Omega_{01}^2 + k_{T2}\Omega_{02}^2)x_f(\Delta\delta_{arms}\cos\delta_{arms0}\sin\Gamma)+ \\
\qquad +(2k_{T1}\Omega_{01}\Delta\Omega_1 + 2k_{T2}\Omega_{02}\Delta\Omega_2)y_f(\sin\delta_{arms0}\cos\Gamma)+ \\
\qquad +(k_{T1}\Omega_{01}^2 + k_{T2}\Omega_{02}^2)y_f(\Delta\delta_{arms}\cos\delta_{arms0}\cos\Gamma)+ \\
\qquad +(2k_{\tau1}\Omega_{01}\Delta\Omega_1 + 2k_{\tau2}\Omega_{02}\Delta\Omega_2)(\cos\delta_{arms0}) - (k_{\tau1}\Omega_{01}^2 + k_{\tau2}\Omega_{02}^2)(\Delta\delta_{arms}\sin\delta_{arms0})- \\
\qquad -(2k_{\tau3}\Omega_{03}\Delta\Omega_3)(\sin\mu)
\end{cases}
\tag{3.21}
$$

Up until this point the linearization procedure used is based on the approximation of the equations using a Taylor series where terms of second and higher order were neglected. In the case of the aerodynamic contributions provided in 3.10 and 3.11, the linearization of such equations around the equilibrium condition of hovering without gusts would not be possible as the magnitude of the disturbances (Δu_g, Δv_g, Δw_g) would always surpass the one of the steady state condition ($u_g = v_g = w_g = 0$). However, despite the aerodynamic contributions in steady state being negligible, fully neglecting them might render the solutions obtained somewhat incorrect, in a way that a decision was made to exceptionally consider the second order terms of the disturbances for the aerodynamic equations. Hence, the equations shown in 3.22 and 3.23 can be obtained from the 3.10 and 3.11 systems of equations, respectively:

$$\begin{cases} \Delta F_{x_a} = -\frac{1}{2}\rho S_w \Delta {u_{gust}}^2 C_D \\ \Delta F_{y_a} = -\frac{1}{2}\rho S_f \Delta v_{gust} |\Delta v_{gust}| C_{Df} \\ \Delta F_{z_a} = -\frac{1}{2}\rho \Delta w_{gust} |\Delta w_{gust}| \left((S_w + S_c) C_{Dw} + S_F C_{Df}\right) - \frac{1}{2}\rho S_w \Delta {u_{gust}}^2 C_L \\ \Delta M_{x_a} = 0 \\ \Delta M_{y_a} = \frac{1}{2}\rho \Delta w_{gust} |\Delta w_{gust}| \left((S_c d_c - S_w d_w) C_{Dw} + C_{Df} S_f d_f\right) + \frac{1}{2}\rho \Delta {u_{gust}}^2 S_w \bar{c} C_M \\ \Delta M_{z_a} = -\frac{1}{2}\rho \Delta v_{gust} |\Delta v_{gust}| C_{Df} S_f d_f \end{cases} \tag{3.22}$$

$$\begin{cases} \Delta F_{x_a} = \frac{1}{2}\rho S_w \Delta {u_{gust}}^2 C_{D0} \\ \Delta F_{y_a} = -\frac{1}{2}\rho S_f \Delta v_{gust} |\Delta v_{gust}| C_{Df} \\ \Delta F_{z_a} = -\frac{1}{2}\rho \Delta w_{gust} |\Delta w_{gust}| \left((S_w + S_c) C_{Dw} + S_F C_{Df}\right) \\ \Delta M_{x_a} = 0 \\ \Delta M_{y_a} = \frac{1}{2}\rho \Delta w_{gust} |\Delta w_{gust}| \left((S_c d_c - S_w d_w) C_{Dw} + C_{Df} S_f d_f\right) \\ \Delta M_{z_a} = -\frac{1}{2}\rho \Delta v_{gust} |\Delta v_{gust}| C_{Df} S_f d_f \end{cases} \tag{3.23}$$

As for the gravitational forces, and after employing the small angle assumption for the attitude angles in hovering conditions, the following system of equations arises:

$$\begin{cases} \Delta F_{x_g} = -mg \cos\theta_0 \Delta\theta \\ \Delta F_{y_g} = mg \left[(\cos\theta_0 \cos\phi_0)\, \Delta\phi - (\sin\theta_0 \sin\phi_0)\, \Delta\theta\right] \\ \Delta F_{z_g} = -mg \left[(\sin\theta_0 \cos\phi_0)\, \Delta\theta + (\cos\theta_0 \sin\phi_0)\, \Delta\phi\right] \end{cases} \tag{3.24}$$

Finally, the only contributions left to linearize are the ones from gyroscopic sources. This allows to derive the following systems of equations for the linearized moments:

$$\begin{cases} \Delta M_{x_{gyro}} = -h_z \Delta q + h_y \Delta r \\ \Delta M_{y_{gyro}} = h_z \Delta p - h_x \Delta r \\ \Delta M_{z_{gyro}} = -h_y \Delta p + h_x \Delta q \end{cases} \tag{3.25}$$

The equations presented so far can also be defined in matrix form. Although some of the derived equations present non-linear terms, it is still relevant to present the obtained system in a style similar to the one of a state space formulation as this formulation can facilitate future tasks such as the development of a computational tool to obtain the trim conditions or even the future definition of a mixer matrix which relates the actuator's inputs to the effect these actions have on the aircraft's dynamics. As so, it is useful do distinguish the previously derived dynamics equations into two groups, a first group which depends on the variation of the usually called "state variables" and a second which depends on the inputs variation. Both the state vector (2.9) and the input vector (2.10) were defined in 2.1.4.

In order for this simplified representation of the dynamics equations to be similar to the one provided

for the state space formulation, the matrix which addresses the contributions of aerodynamic, gravitational and gyroscopic sources to the general force/moment balance was defined as matrix $\mathbf{A}$. Similarly, the matrix which, when multiplied by the vector of the input variations, denotes the influence of the propulsive forces and moments to the general model was named matrix $\mathbf{B}$. As a result, the following formulation can be achieved, where $[\mathbf{\Delta F}\ \mathbf{\Delta M}]^T = [\Delta F_x\ \Delta F_y\ \Delta F_z\ \Delta M_x\ \Delta M_y\ \Delta M_z]^T$:

$$\begin{bmatrix} \mathbf{\Delta F} \\ \mathbf{\Delta M} \end{bmatrix} = \mathbf{A}\mathbf{\Delta x} + \mathbf{B}\mathbf{\Delta u} \tag{3.26}$$

with,

$$\mathbf{\Delta x} = [\Delta u_{gust}\ \Delta v_{gust}\ \Delta w_{gust}\ \Delta p\ \Delta q\ \Delta r\ \Delta X\ \Delta Y\ \Delta Z\ \Delta\phi\ \Delta\theta\ \Delta\psi]^T \tag{3.27}$$

and,

$$\mathbf{\Delta u} = [\Delta\Omega_1\ \Delta\Omega_2\ \Delta\Omega_3\ \Delta\delta_{arms}]^T \tag{3.28}$$

As explored earlier, two distinct aerodynamic models are used according to the x component of the gust or longitudinal velocity being positive/null or negative. As so, two $\mathbf{A}$ matrices must be defined. For an easier distinction, the one which uses the expressions given in 3.22 will be named $\mathbf{A_f}$ and the one derived front the aerodynamic model provided in equations 3.23 will be referred to as $\mathbf{A_r}$. These matrices can be defined as follows, with the $A_{f,r_{ij}}$ elements being used as a way to facilitate their representation.

$$\mathbf{A_{f,r}} = \begin{bmatrix} A_{f,r_{11}} & 0 & 0 & 0 & 0 & 0 & 0 & 0 & 0 & 0 & -mg\cos\theta_0 & 0 \\ 0 & A_{f,r_{22}} & 0 & 0 & 0 & 0 & 0 & 0 & 0 & mg\cos\phi_0\cos\theta_0 & -mg\sin\phi_0\sin\theta_0 & 0 \\ A_{f,r_{31}} & 0 & A_{f,r_{33}} & 0 & 0 & 0 & 0 & 0 & 0 & -mg\sin\phi_0\cos\theta_0 & -mg\cos\phi_0\sin\theta_0 & 0 \\ 0 & 0 & 0 & 0 & -h_z & h_y & 0 & 0 & 0 & 0 & 0 & 0 \\ A_{f,r_{51}} & 0 & A_{f,r_{53}} & h_z & 0 & -h_x & 0 & 0 & 0 & 0 & 0 & 0 \\ 0 & A_{f,r_{62}} & 0 & -h_y & h_x & 0 & 0 & 0 & 0 & 0 & 0 & 0 \end{bmatrix} \tag{3.29}$$

with,

$A_{f\,11} = -\frac{1}{2}\rho S_w \Delta u_{gust} C_D$
$A_{f\,22} = -\frac{1}{2}\rho S_f |\Delta v_{gust}| C_{Df}$
$A_{f\,31} = -\frac{1}{2}\rho S_w \Delta u_{gust} C_L$
$A_{f\,33} = -\frac{1}{2}\rho |\Delta w_{gust}| \left((S_w S_c) C_{Dw} + S_F C_{Df}\right)$
$A_{f\,51} = \frac{1}{2}\rho \Delta u_{gust} S_w \overline{c} C_M$
$A_{f\,53} = \frac{1}{2}\rho |\Delta w_{gust}| \left((S_c d_c - S_w d_w) C_{Dw} + C_{Df} S_f d_f\right)$
$A_{f\,62} = -\frac{1}{2}\rho |\Delta v_{gust}| C_{Df} S_f d_f$

and,

$$A_{r11} = -\tfrac{1}{2}\rho S_w \Delta u_{gust} C_{D0}$$
$$A_{r22} = -\tfrac{1}{2}\rho S_f |\Delta v_{gust}| C_{Df}$$
$$A_{r31} = 0$$
$$A_{r33} = -\tfrac{1}{2}\rho |\Delta w_{gust}| \left((S_w + S_c) C_{Dw} + S_F C_{Df}\right)$$
$$A_{r51} = 0$$
$$A_{r53} = \tfrac{1}{2}\rho |\Delta w_{gust}| \left((S_c d_c - S_w d_w) C_{Dw} + C_{Df} S_f d_f\right)$$
$$A_{r62} = -\tfrac{1}{2}\rho |\Delta v_{gust}| C_{Df} S_f d_f$$

The actuation matrix ($\mathbf{B}$), will be derived from the equations presented in 3.21 and take the form of a 6×4 matrix which is presented in appendix B.

3.1.6 Controller

In order to gain an initial understanding on the expected behaviour of the proposed configuration in flight a basic altitude and attitude controller was implemented in Simulink® with an FDM based on the equations previously deduced.

The controller developed (3.3) was then requested to maintain a given altitude while following null values of roll, pitch and yaw angles, with the main conclusion being that the aircraft could indeed assume such attitude at the expense of constantly drifting to the right. This is due to the thrust vectoring happening in the front rotors, which developed right pointing thrust components with the goal of maintaining an equilibrium of torques along the yaw axis.

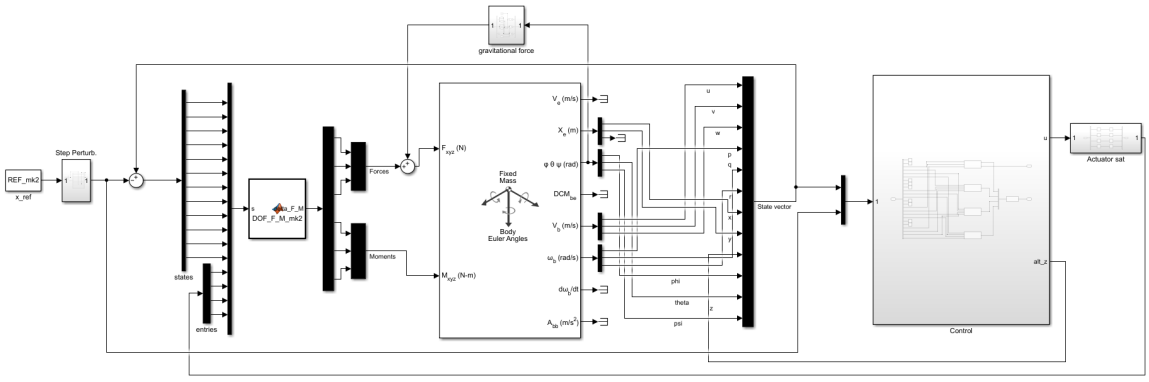

Figure 3.3: Preliminary controller developed to study the configuration's behaviour.

3.2 Trim Analysis and Parametric Studies

Having defined the dynamic equations and performed this preliminary study on how the configuration will behave, it made sense to assess what the aircraft's hovering attitude should be in order to maintain its position. Furthermore, it is also beneficial for future work to conduct studies on the dynamics of the aircraft when the rear propeller assumes a tilting angle such that the thrust vector created by it is no longer vertical and the aircraft assumes longitudinal speed.

In this section, the parametric studies performed for the Mini-E case will be analysed. However, since flight testing will be performed by a smaller test vehicle, with the objective of testing not only the developed controller but also the entire concept of this novel tri-rotor configuration, parametric studies were also performed for the latter.

In order for the test vehicle to serve as an adequate sample of what the behaviour of the actual aircraft would be in VTOL mode, it was designed in a way that the thrust force distribution was $20/80$, which is possible by having a longitudinal distance between the front rotors and the center of gravity of the aircraft that is four times larger than the longitudinal distance between the rear rotor (when fully vertical) and the CG. Additionally, the lateral distance between the front rotors and the longitudinal axis of the aircraft is such that the ratio of this distance to the longitudinal distance between front and rear rotors was equal for both aircraft.

However, since this test aircraft's airframe was developed to test the tri-rotor concept in vertical flight, and as it was designed to be as simple and light as possible, no aerodynamic surfaces were attached to it in a way that this multirotor does not have any wings nor a canard as the Mini-E does. As so, for the parametric studies involving the test aircraft, the aerodynamic contributions to the force and moment balances were simplified.

In the following subsections several parameters related with the two drones' attitude and actuation will be analysed. However, these parameters will not be exactly the same since, for example, in the Mini-E's analyses the rudder actuation will be considered while in the test tri-rotor such an analysis would be impossible due to the nonexistence of this actuator. Nevertheless, the analysis of several parameters such as the bank, pitch and frontal arms tilt angles as well as the rotors rotational speed are common to both aircraft.

Furthermore, and for the case of the Mini-E, an additional parametric study was carried out when it comes to the ideal opening angle of the frontal arms, Γ, that would allow to minimize the arm's rotation angle, δ_{arms}, in trim conditions with the rear rotor in a fully vertical position and without gusts.

In order to obtain such results, the chosen approach was to employ a non-linear constraints optimization algorithm by the use of the Matlab® function $fmincon$. This program is used as a tool to solve the non-linear trim equations while allowing for greater flexibility in the definition of acceptable tolerances in the residual linear and angular accelerations. The optimization problem was thus defined as follows:

$$min \sum_{i=1}^{3} P_i$$
$$\text{w.r.t. } [\phi, \theta, \Omega_1, \Omega_2, \Omega_3, \delta_{arms}, \delta_r]$$

subject to:

$$\begin{cases} F_{xa} + F_{xprop} + F_{xg} = 0 \\ F_{y_a} + F_{y_{prop}} + F_{y_g} = 0 \\ F_{za} + F_{zprop} + F_{zg} = 0 \\ M_{xa} + M_{xprop} = 0 \\ M_{y_a} + M_{y_{prop}} = 0 \\ M_{za} + M_{zprop} = 0 \end{cases} \tag{3.30}$$

Table 3.4: Study variables' boundaries.

Variable	**Lower Bound (Mini-E/Test vehicle)**	**Upper Bound (Mini-E/Test vehicle)**
ϕ	$-30°$	$30°$
θ	$-30°$	$30°$
Ω_1	$0\,rpm$	$8200\,rpm$ / $38400\,rpm$
Ω_2	$0\,rpm$	$8200\,rpm$ / $38400\,rpm$
Ω_3	$0\,rpm$	$6374\,rpm$ / $16640\,rpm$
δ_{arms}	$-15°$	$15°$
δ_r	$-30°/NA$	$30°/NA$

In this definition, three aspects must be taken into account. The first is related to the cost function, which should be minimized and that was defined as the sum of the mechanical power (P_i) developed by each of the rotors. It is important to realise that while in hovering conditions there is only one trimmed configuration possible but as the forward speed increases (through the existence of frontal gusts or horizontal movement of the aircraft), redundancies will arise in the force producing mechanisms (rotors and lifting surfaces), thus rendering it useful to apply an optimization procedure for power minimization.

The second point is related with the optimization variables as some of them will not be used in some of the analysis that will be presented. This will be justified when this is the case. An initial estimation of these variables' values is also required to run the algorithm.

Finally, the constraint equations obtained from the system presented in 3.1 will not take into account the gyroscopic effects as these only arise when the aircraft is subjected to angular rates, which will be null in trimmed conditions. The imposed constraints could also be defined as inequalities where a deviation factor would be defined for which the problem would be deemed as solved (for example if the resultant force in a given direction was less than 1% of the total gravitational force acting on the aircraft). However, there was no need to use inequalities, since the algorithm managed to solve the problem with the defined equations.

By applying the described tool to both the Mini-E and the test vehicle case studies, it was possible

to obtain the values presented in table 3.5 for the expected attitude and actuation required to maintain steady hovering flight in a gust free environment and with the rear rotor in its fully upright position.

Table 3.5: Values of the different optimization variables in trim conditions for both aircraft.

Variable	Mini-E	Test Vehicle
ϕ	$-0.338°$	$-0.700°$
θ	$0°$	$0°$
Ω_1	$6047\,rpm$	$21995\,rpm$
Ω_2	$6047\,rpm$	$21995\,rpm$
Ω_3	$4909\,rpm$	$11222\,rpm$
δ_{arms}	$2.484°$	$5.019°$
δ_r	$0°$	NA

By analysing the cases of two distinct vehicles with the same VTOL configuration it is possible to draw preliminary conclusions, namely when it comes to the attitude that such vehicles will present in hover. Starting by the tilting angle of the front tilting mechanism introduced in this configuration, it assumes, for both cases, a positive value. Since the simulated vehicles follow the configuration provided in 2.1 and in both the resultant drag torque developed by the three rotating propellers is negative (in z), the tilting action of the front rotors will result in the development, through the use of thrust vectoring, of a positive torque in the same axis, thus counteracting the existing drag torque. This counter torque is created due to the development of a lateral, positive thrust component which will then need to be compensated in order for the aircraft to be maintained in equilibrium in the y direction. This equilibrium is obtained through the introduction of a negative roll angle (ϕ) which will create a left pointing component of the gravitational force in the local reference frame. This coupling between roll and front tilting angle will be characteristic of any vehicle developed with this configuration, as long as a drag torque imbalance is verified.

3.2.1 Mini-E

A parametric study concerning the arms opening angle Γ was of interest, as even though the final front rotors position was already defined in [27] for the Mini-E design, this angle was not. This variable will have an influence on the dynamics of the aircraft given the fact that the frontal arms of the tri-rotor are capable of tilting, which means that depending on this angle's value a similar actuation of the tilting mechanism can have different effects on the aircraft global attitude in vertical flight as depicted in the previously derived equations concerning the forces and moments due to the propulsive system (3.2).

Nevertheless, the findings regarding the opening angle of the arms are not to be taken as a hard constraint for the final tri-rotor design, since other factors may arise in the mechanical design that limit the use of said results.

Arms' Opening Angle, Γ

The present parametric study simulated hovering conditions, without the presence of gusts and with the rear rotor in a fully vertical position. Since no gusts are present and the equations were resolved for steady hovering conditions, there should be no actuation of the aerodynamic control surfaces. As so, the rudder and the ailerons' deflection alongside the canard's incidence relative to cruise conditions were all set as null. Therefore, the variables in analysis are the pitch angle (θ), the roll angle (ϕ), the rotating speed of the three rotors (Ω_1, Ω_2, Ω_3) and the tilt angle of the frontal arms (δ_{arms}). The yaw angle is taken as null as it has no influence on the static behaviour of the aircraft in hover.

A range of values of the arms' opening angle was analysed, from $25°$ to $75°$. It was chosen not to analyse angles lower than $25°$ because, as the front rotors have longitudinal positions close to the one of the canard, by using low opening angles of the arms the tilting and retracting mechanism of such arms would be too close and possibly interfere with the incidence variation mechanism of the canard, thus the definition of this lower boundary. As for the upper bound, it was defined as a way of limiting the arm's length (for structural reasons) and to ensure that the previously mentioned mechanisms would not be located near the aft region of the aircraft, where most of the avionics are located. With this range defined, it was then possible to analyse the differences in the aircraft's attitude and required actuation in hover with the opening angle of the arms.

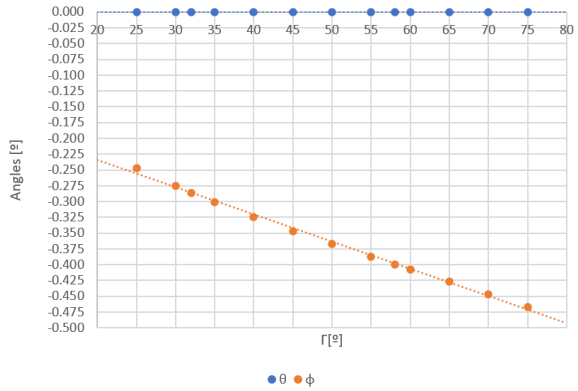

(a) Variation of the pitch (θ) and roll (ϕ) angles with the arms' opening angle (Γ).

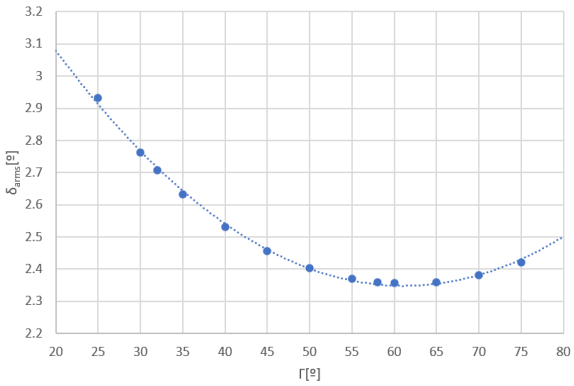

(b) Variation of the frontal arms' rotation angle (δ_{arms}) with the opening angle (Γ).

Figure 3.4: Results from the parametric study of the Mini-E's trim conditions with varying Γ.

When it comes to the pitch and roll angles, the results obtained showed that in trim conditions the aircraft's pitch angle is null regardless of the value of Γ as expected. As for the roll angle at which the equilibrium of forces and moments occurs, it does increase in magnitude somewhat linearly with the value of Γ between both ends of the considered range, but such changes are quite small with a maximum $\Delta\phi$ of $0.22°$ being registered between those two points.

When it comes to the rotational speed of the rotors it was found that the variation of speed with the opening angle was almost null, with both front rotors registering a value around $6000\,rpm$ and the rear rotor of $4900\,rpm$ throughout the entire range of the simulations. It was expected that these speeds would vary due to the aforementioned change in the roll angle throughout the analysis, however, given

the small variation registered, it is comprehensible that the rotor speed is maintained almost constant irrespective of the value of Γ. In fact, the largest variation registered was in the rotational speed of the frontal rotors, of 0.01% and therefore negligible.

As for the rotation angle of the frontal arms, it was defined that it would be desirable to minimize it in order to also reduce the required lateral components of the thrust force developed by the front rotors and the consequent reduction in vertical thrust which would require an increase in the front rotors power consumption. The obtained results were fitted with a quadratic curve (Figure 3.4) and it was determined that the arm's deflection would be minimized for an opening angle of $61.1°$.

From the results plotted above, one can deduce that even though the deflection in trim is minimized for a value of Γ equal to $61.1°$, the use of opening angles in the vicinity of this will result in a similar required rotation angle of the frontal arms in hovering conditions, thus having negligible effects in power consumption.

In fact, this value of $61.1°$ was initially used in the mechanical design that shall be presented later in this document. However, due to the fact that the longitudinal and lateral position of the rotors had already been defined in previous works, it was found that to meet those values while using a Γ of $61.1°$ the arms were longer than what was desired and susceptible to suffering considerable deflection when loaded. Moreover, the location of the root of the arms, where the tilting mechanism is located, was also further aft that what was desired, in a way that a trade-off needed to be made. By considering the results achieved in this parametric study alongside these other constraints, it was decided that a $43°$ opening angle should be used (the results presented in table 3.5 already consider this value of Γ). Even though there is a 29.6% difference between these values, it was found that the actual difference in the arms' tilting angle in trimmed conditions while hovering would be of just $0.14°$ ($\approx 6\%$), a reasonably small difference which will actually have little impact on the aircraft's global hovering attitude and power consumption while proving beneficial for the upcoming mechanical design of the tilting mechanism.

Gusts

With the geometry of the tri-rotor configuration being now completely defined, and a value of the arm's opening angle, Γ, of $43°$, it was now possible to perform additional parametric studies in order to understand what attitude the aircraft tends to acquire to achieve equilibrium while exposed to constant gusts of a certain magnitude and direction.

This trim analysis was performed by introducing gusts hitting the aircraft from 6 directions (front, back, left, right, up and down). However, in a real-world scenario, it is unlikely that the aircraft will face unidirectional gusts, but rather gusts with multiple components, which means that the present results were obtained with the objective of serving as an indicator of how this novel configuration aircraft reacts to the different components of the gust, rather than an effective representation of a real world scenario.

X-Wise Gusts

Firstly, the case of the Mini-E tri-rotor aircraft facing longitudinal frontal and rearward gusts will be taken into account. For this, the value of the longitudinal velocity of the aircraft was varied (considering

that the aircraft's reference frame was, initially, aligned with the earth reference frame), from $-10\,m/s$ to $10\,m/s$, where the positive values represent frontal gusts and negative values the opposite case.

For this analysis, the studied variables were the pitch and roll angles (θ and ϕ, respectively), the rotational velocities of the three rotors (Ω_1, Ω_2 and Ω_3) and the frontal arms tilting angle (δ_{arms}). The obtained results are represented below on Figure 3.5.

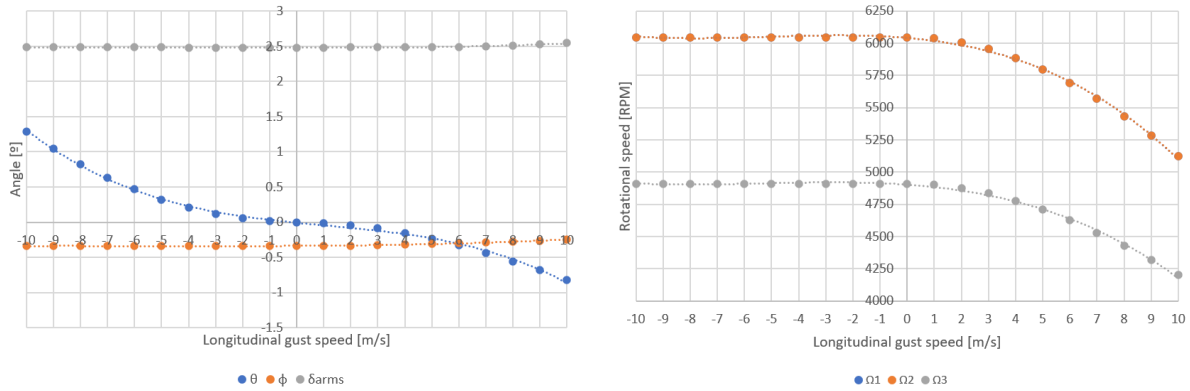

(a) Evolution of the pitch angle, roll angle and arms' tilting angle with the value of the longitudinal gust.

(b) Evolution of the rotors' rotating speeds with the value of the longitudinal gust.

Figure 3.5: Results from the parametric study of the Mini-E's behaviour under the influence of longitudinal gusts.

Starting with the analysis of the evolution of the aircraft's attitude with the gust speed, it becomes clear that, for stronger rear gusts, the aircraft tends to assume a positive pitch attitude, as expected, to counteract the developing drag, while denoting a (almost constant) tendency to roll in the negative direction, i.e., to the left. This rolling tendency can be explained by the fact that the rear propeller develops a larger drag torque than the frontal ones combined in a way that the frontal arms need to rotate in the positive sense to develop a counter torque and maintain an equilibrium of moments about the yaw axis. At the same time, this actuation leads to the development of a lateral, y positive, thrust force component, which will then be counteracted by the rolling attitude (to the left), i.e., the aircraft balances this lateral thrust force with a component of its own weight.

Meanwhile, with frontal gusts, as the speed increases the rotational speed of the rotors decreases, which is consistent with the fact that the aircraft possesses lifting surfaces (wing+canard), which provide lift with the increasing wind speed (note that $10\,m/s$ is already quite close to the theoretical stall speed of $13\,m/s$ that was determined for this aircraft in [44]). Furthermore, besides this reduction in all of the rotors' speed, it is also noticeable that the aircraft tends to assume a negative pitching angle, in order to use the vertical component of the thrust of its rotors to balance the developing drag force. A slight reduction of the still negative roll angle is also registered, and the rotation angle of the frontal arms is maintained approximately constant (with just a small increase for the $10\,m/s$ gust, which may be due to the necessity of balancing the torques around the yaw axis). The reason for the aircraft to assume this roll angle and to rotate the arms in such a way is the same as for the case of the rear gusts.

Y-Wise Gusts

In the case of lateral gusts occurring, where the positive sign denotes gusts coming from the right and a negative sign for the opposite direction, the obtained results are the ones shown in Figure 3.6. It is important to note that the range of velocities analysed, unlike in the previous case, is not from $-10\,m/s$ to $10\,m/s$. This is due to the fact that for gusts coming from the left with a magnitude of more than $4\,m/s$ the aircraft would assume a (negative) rotation angle of the frontal arms that exceeded the limit value of $15°$, while for right-coming gusts with a magnitude over $4\,m/s$ it was also impossible to obtain an equilibrium condition within the defined bounds as the rotation angle of the frontal arms (δ_{arms}) would exceed $15°$ (in the positive sense).

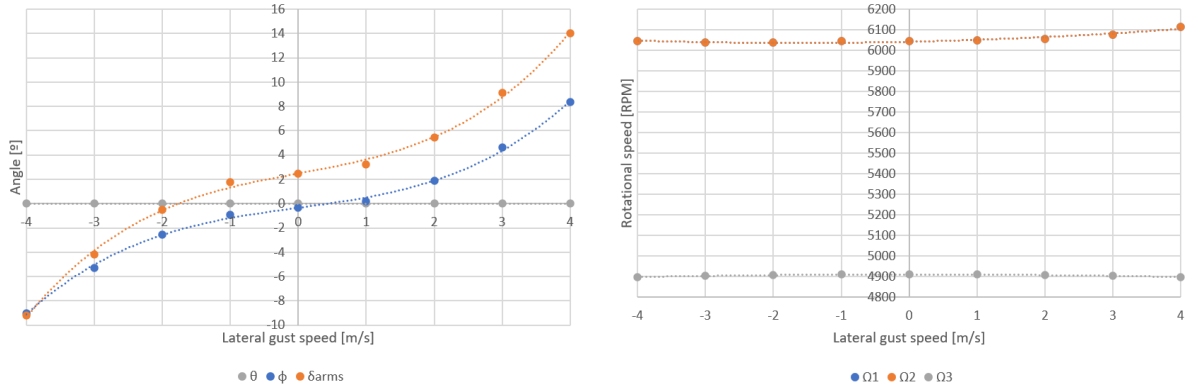

(a) Evolution of the roll and arms' tilting angle with the value of the lateral gust.

(b) Evolution of the rotors' rotating speeds with the value of the lateral gust.

Figure 3.6: Results from the parametric study of the Mini-E's behaviour under the influence of lateral gusts.

One of the distinctive features of this analysis in relation to the previous one is that the pitch angle is consistently null across all the analysis, reflecting that the aircraft, when exposed to lateral gusts, does not change it's longitudinal attitude. However, when it comes to the roll angle, the same does not happen, with considerable variations being registered across the range of analysis. For negative gusts, i.e., gusts coming from the left, the aircraft has a tendency to roll to the left. By doing so, the vertical component of the thrust developed by the rotors starts to counteract the positive lateral component of the drag that is developed. In order to maximize this effect, the δ_{arms} angle also decreases and even assumes negative values, creating a left-pointing thrust component meant to counteract the lateral drag that is developing. Meanwhile the rotational speed of the rotors experiences only small variations relative to the values that they usually assume for normal hovering conditions.

For positive (right-coming) gusts, the rotational speed of the front rotors increases slightly which may be due to the superior tilting of the frontal arms (relative to the previous case of left-coming gust) which leads to a decrease of the vertical component of the thrust developed by these rotors (for a similar rotation speed) thus resulting in an increase of the required thrust and consequently rotational speed to achieve equilibrium. In terms of variations in attitude, the aircraft has, this time, a tendency to bank to the right (rolling in the positive sense) to counteract the developing (y, negative) drag force

by using the developed, locally vertical, thrust. In order to minimize the required power to achieve the equilibrium condition, the aircraft tends to increase the δ_{arms} angle, enhancing the lateral, y positive, thrust component developed, in order to once again, counteract the drag force that acts in the same direction but in the opposite sense.

Z-Wise Gusts

Finally, it is time to analyse the behaviour of the aircraft in hovering conditions when exposed to vertical gusts, where positive values refer to upward gusts and negative values to downward gusts. Said results are therefore presented in the following figures:

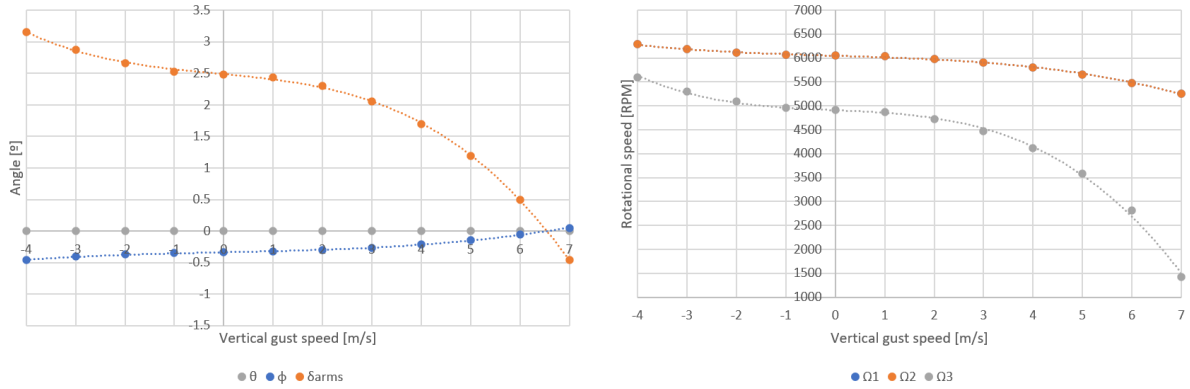

(a) Evolution of the roll and arms' tilting angle with the value of the vertical gust.

(b) Evolution of the rotors' rotating speeds with the value of the vertical gust.

Figure 3.7: Results from the parametric study of the Mini-E's behaviour under the influence of vertical gusts.

From these, and considering firstly the case of downward gusts, it is worth to mention that the aircraft can not handle, within the limits imposed, downward gusts with a magnitude over $4\,m/s$. This limitation occurs because, for wind speeds above this value, the rear motor surpasses the maximum rotational speed that it can achieve, which is a comprehensible result given that, in such a case, the rotors have to balance not only the local vertical component of the weight of the aircraft itself but also a positive z component of the drag force that arises under these conditions. When the downward gusts exhibit a magnitude equal to or bellow $4\,m/s$ however, the general trend is that the rotor speeds increase with the increasing magnitude of the gust's speed while the pitch angle remains approximately null and the roll angle tends to assume negative values to balance the locally positive y component of the thrust force, developed due to the tilting of the frontal arms in the positive sense. This angle increases with the increasing magnitude of said downward gusts.

For the opposite case of upward gusts, and since the developing drag force tends to be negative in the local body reference frame, the rotor speeds decrease, specially the one of the rear rotor, which results in the reduction of the need to balance the moments around the yaw axis due to its drag torque, thus leading the frontal arms to rotate in the negative sense with the increasing gust speed until eventually δ_{arms} becomes negative (counteracting now the thrust torque developed by the frontal rotors which

now surpasses the one developed by the rear one) for the case of an upward gust speed with a $7\,m/s$ magnitude. For this limit situation then, the frontal rotors tilting angle now balances the overall drag torque developed by the three rotors and since this tilting angle is quite reduced, thus developing a small y component of the thrust force, the aircraft tends to level itself until the roll angle is approximately null.

For magnitudes greater than $7\,m/s$ the aircraft will no longer maintain its altitude as the rear rotor speed falls bellow zero and it is not possible generate downward thrust with the rear rotor, at least with the proposed configuration.

With these results it is then possible to draft an initial flight envelope for the vehicle in hovering conditions under the influence of gusts, as presented in Table 3.6. It is important to draw attention once again to the fact that only a simplified, decoupled, aerodynamic model was used to obtain such values.

Table 3.6: Maximum allowable gust magnitude in each direction.

Gust direction	**Front**	**Rear**	**Left**	**Right**	**Up**	**Down**
Maximum allowable magnitude (m/s)	>10	>10	4	4	7	4

Rear Tilt Angle

In this parametric study, a study of the tri-rotor's attitude and actuation, this time including the rudder and rear tilting mechanism action, is performed where the forward speed of the aircraft was changed to find which rear tilting angle allowed to achieve a steady forward flight equilibrium (along with the other actuators). This analysis was done by providing forward velocities and analysing what the rear tilting angle would be such that an equilibrium condition was attained, i.e., that the aircraft maintained a null pitching angle and a constant altitude. However, the final objective of this analysis is to have an idea of how the tilting of the rear rotor will affect the evolution of the forward speed of the aircraft. This study is particularly relevant for the future implementation of a controller for the transition between VTOL mode and cruise mode as it allows to understand how the actuators used in the VTOL configuration behave under transition conditions. The variables considered in this parametric study were the value of the rear tilting angle (μ), the roll angle (ϕ), the three rotor's rotational speeds (Ω_1, Ω_2 and Ω_3), the frontal arms rotation angle (δ_{arms}) and the rudder deflection (δ_r). In order to consider the actuation of the rudder, the equations derived in 3.1.2 were modified to include this parameter, namely the influence of the rudder action in terms of rolling and yawing moments (3.31).

$$\begin{cases} M_{x_{rudder}} = \frac{1}{2}\rho u^2 S_w b C_{l_{rudder}} \delta_r \\ M_{z_{rudder}} = \frac{1}{2}\rho u^2 S_w b C_{N_{rudder}} \delta_r \end{cases} \tag{3.31}$$

The analysis was made with a range of velocities spanning from $0\,m/s$, consistent with a hovering condition without the presence of gusts until a velocity of $16\,m/s$, value which exceeds the one obtained for the stall speed, at $13\,m/s$. This velocity is still short of the cruise speed value of $20\,m/s$, however, this flight condition is already well outside the scope of the VTOL system in a way that the transition will

occur at a speed bellow the one at which the aircraft will fly at usual cruise conditions, but above the stall condition. The results yielding from the analysis are shown in Figure 3.8.

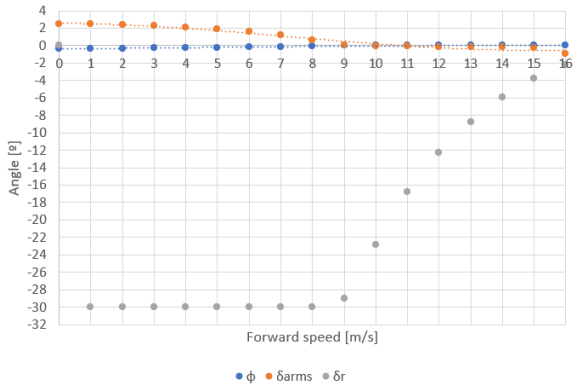

(a) Evolution of the roll angle, arms' tilting angle and rudder deflection with forward speed.

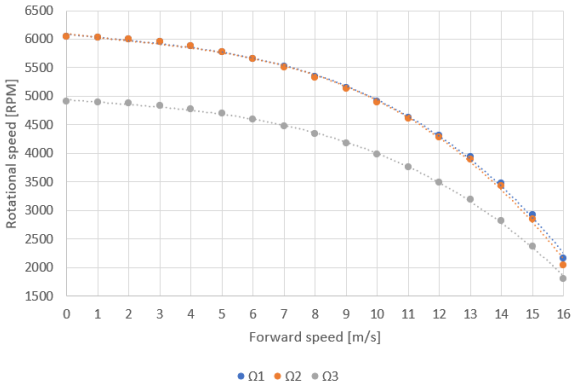

(b) Evolution of the rotors' rotating speeds with forward speed.

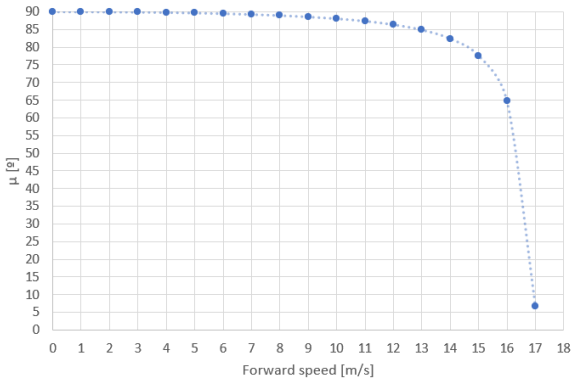

(c) Evolution of the rear tilting angle, μ, with forward speed.

Figure 3.8: Results from the parametric study of the Mini-E's behaviour under different forward speeds.

From the results shown in the first graph of Figure 3.8 in becomes clear that for the lower spectrum of velocities (ranging from about $1\,m/s$ up to $9\,m/s$) the aircraft assumes the maximum available value for the deflection of the rudder in order to aid the forward rotor's lateral thrust component and drag torque counteracting the drag torque developed by the rear propeller in VTOL mode. This maximum value of the rudder deflection is explained by the fact that, as patent in equations 3.31, this surface's action is dependent on the square of the forward velocity, which leads to a really low authority of said control surface at lower speeds. Given this low authority of the rudder in this lower range of forward speeds, it is therefore comprehensible that the frontal arms rotation angle (δ_{arms}) assumes roughly the same value as in hovering conditions in the lower end of the velocity spectrum, with a tendency to lower this tilting angle's value as speed increases. This diminishing of the tilting angle can be explained by two factors. The first is the increasing authority of the rudder as the forward speed increases and the second is related with the (z positive) drag torque developed by the rear propeller, which decreases with the increasing airspeed. This drag torque reduction can itself be attributed to two other factors. The first, although with small influence in the lower range of the velocity spectrum analysed, is the tilting angle of the rear rotor, which, when decreased (in the present analysis it was considered that when the rotor is in

a vertical position $\mu = 90°$) leads to a reduction in the drag torque component along the yaw axis (for a constant rotational speed). The second, more relevant, factor is that with the increasing forward velocity the aircraft's lifting surfaces start generating lift, reducing the thrust that each rotor is required to provide and the accumulated drag torque in the process. This means that at one point ($\approx 10\,m/s$), the tilting angle of the front rotors approaches the value of $0°$ (as with the rotor speed decrease the authority of this actuator is also reduced) and the balance along the yaw axis can now be performed mainly by the action of the rudder (which authority, in its time, increases, thus the reduction in the required deflection that is patent in the first graph).

From the analysis of the evolution of the roll angle with forward speed, it becomes clear that, as expected for a forward flight condition, the aircraft assumes very low values of bank angle. Initially these values are negative ($\approx -0.4°$) in order to provide the trimmed conditions that were already referred earlier in this text but it tends to $0°$ as the aircraft gains velocity.

Finally, it is time to analyse the evolution of the tilting angle of the rear rotor with forward speed. In the vicinity of the μ value of $90°$, it becomes clear that very fine adjustments to the tilting angle will generate considerable variations in the forward speed, leading to the conclusion that the aircraft, while hovering, will be very sensitive to the tilting action of the rear rotor assembly. For example, to attain a flight speed of approximately $13\,m/s$ (stall speed of the aircraft), it is only necessary, according to the obtained results, to tilt the rear rotor by $5°$. After this stage, the variations in the tilting angle necessary to increase the flight speed while in equilibrium will become larger as the aircraft's lift generation will stop depending mainly on the rotors' thrust and starts depending primarily on the lift force generated by the lifting surfaces, thus allowing for the rear rotor to tilt further and start providing mostly horizontal thrust.

This relation between the evolution of forward speed with the tilting action of the rear rotor can be explained by the increasing contribution of the aerodynamic surfaces to the overall generation of lift against the reducing need to generate vertical thrust through the use of the rotors. Since the optimization goal is to reduce the power consumption through the minimization of the mechanical power developed, the rotors' speed will be reduced with the increasing forward speed and the rear rotor's thrust will start playing a more relevant role in the generation of forward than vertical thrust. However, with the reducing rotational speed that happens due to the diminishing need to generate vertical thrust, and to maintain the required level of forward thrust to balance the building drag force the tilting action will ramp up, as depicted in 3.8.

In this last figure, it is noticeable that the analysis was only made up until a forward flight speed of $16\,m/s$, as this was the last value for which the developed tool would find suitable equilibrium conditions (from $17\,m/s$ onward the analysis would already fall solely on the horizontal flight stage, with the actuation of control surfaces such as the ailerons and canard incidence being required, which is outside of this work's scope). Nevertheless, a predictive value was obtained for the required tilting at $17\,m/s$ as can be seen on the last graph, yielding that for such a forward velocity the rear tilting angle relative to the horizontal would be around $6.75°$, with this angle being null for forward speeds above $17.1\,m/s$.

3.2.2 Test Tri-rotor

As referred earlier, it is of interest to also analyse the vehicle that shall be used to test the concept of this novel configuration tri-rotor, as to have a better understanding of how the aircraft should behave under different flight conditions. This vehicle will present the same arm's opening angle (Γ) that will be used in the Mini-E $(43°)$ with this variable being fixed throughout the following studies. However, the comparison of some results, such as the dynamics when there is a tilting action of the rear mechanism cannot be compared to the ones found for the Mini-E case, as this test aircraft does not have lifting surfaces, in a way that only the VTOL configuration and the conceptual design of the tilting mechanisms may be assessed. An analysis on the influence of gust and on the effects of the tilting action of the rear rotor will, nevertheless, be conducted in order to obtain useful data on how the aircraft should perform in real world conditions such as the ones it will face in test flights.

It is also important to refer that some modifications had to be made to the code in order to simulate the test vehicle's behaviour, namely regarding the aerodynamic model used. To do so, the contributions of the lifting surfaces were removed from the model and the reference dimensions, namely surface areas of the airframe, were obtained from a detailed CAD model alongside the inertial data. Given the simplified design of the airframe the drag coefficient was taken as the one of a plate perpendicularly placed against the oncoming flow for all directions.

The location of the rotors in the test tri-rotor was chosen to meet the distance ratios verified in the Mini-E, with the values being available in Table 3.7.

Table 3.7: Rotor distances from the center of gravity of the aircraft.

Distance [m]	
x_f	0.375
x_r	0.094
y_f	0.207

Gusts

X-Wise Gusts

First, a study of the behaviour of the aircraft that allows to achieve equilibrium when facing longitudinal gust from both directions (front for positive values and back for negative ones) will be conducted. The range of gust velocities analysed was once more fixed between the values of $-10\,m/s$ and $10\,m/s$. The program did not find any issues solving the problem of achieving trim conditions with the imposed constraints, defined in Table 3.4. The motors that shall be utilized in this vehicle's development were characterized by performing static propulsion tests to know the thrust and torque they would develop (with the correct propellers assembled) as well as the rotational velocity throughout the throttle range. The assumption that both the thrust and drag torque vary quadratically with the angular velocity of the rotors was once more applied with the following values of the thrust and torque constants arising for both

the front and rear[1] rotors:

Table 3.8: Thrust and toque constants for the motors used in the test vehicle.

Motors	k_T	k_τ
1, 2	2.03738×10^{-7}	2.17124×10^{-9}
3	6.08091×10^{-6}	7.18907×10^{-8}

As so, the obtained results for the case of an hovering flight under longitudinal gusts were the ones presented bellow on Figure 3.9.

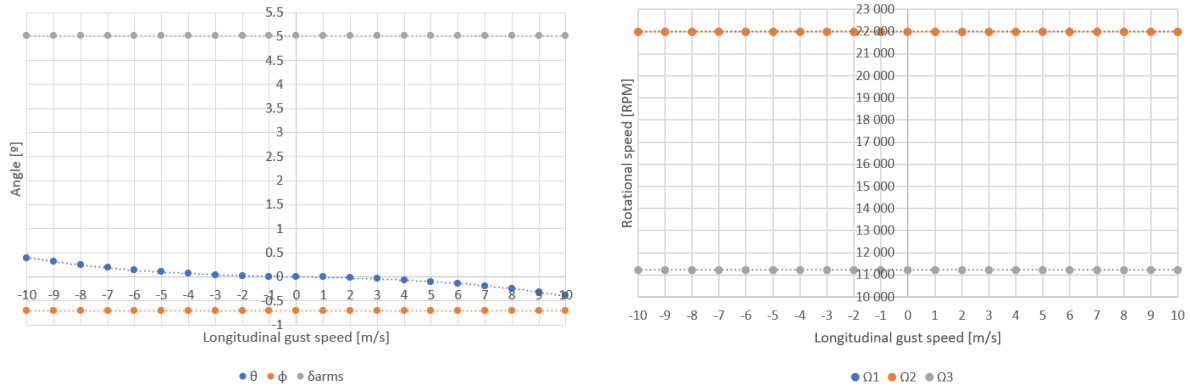

(a) Evolution of the pitch angle, roll angle and arms' tilting angle with the value of the longitudinal gust.

(b) Evolution of the rotors' rotating speeds with the value of the longitudinal gust.

Figure 3.9: Results from the trim analysis of the test vehicle's behaviour under the influence of longitudinal gusts.

From the first graph, the immediate perception is that both the roll angle and the tilt angle of the frontal arms are invariable throughout the entire range of flight conditions ($\phi = -0.7°$ and $\delta_{arms} = 5.019°$) which is consistent with the information portrait on the second graph (rotational speed of the rotors against gust speeds) where it becomes clear that, irrespective of the magnitude and direction of the longitudinal gusts, the rotational speed of the three rotors remains the same ($\Omega_1 = \Omega_2 = 21995\, rpm$ and $\Omega_3 = 11222\, rpm$), thus explaining the constant values of ϕ and δ_{arms}. The pitching angle changes along the range of gust velocities, assuming positive values (pitch-up) for rear coming gusts and negative values (pitch-down) for frontal gusts. This is consistent with the aircraft trying to counteract the drag force that develops in the same direction as the oncoming gust. These variations are, however, quite reduced (the range of θ for the entire analysis is only of $-0.4°$ to $0.4°$). This is due to the relatively small characteristic areas of the vehicle, particularly the frontal/rear one, which leads to the development of a rather small longitudinal drag force that requires small variations in the pitch angle to be balanced.

From these results, and when performing a brief comparison with the homologous results obtained for the case of the Mini-E, one can easily denote the rather different behaviour observed for the evolution

[1]For the rear rotor's static thrust tests it was not possible to obtain angular velocities due to technical problems related to the test bench. Furthermore this rotor's assembly was too large to perform the tests using the same test bench as the front rotors. As so, its k_T and k_τ values were estimated based on the relation found between the front motors' kV value, input voltage and rpm achieved for various values of throttle and applied to the rear rotor's thrust tests.

of the three rotors' speed with the longitudinal gust speed. Whereas for the test vehicle these speeds are approximately invariant throughout the range (the tilt angles are small and so are the consequent variations in vertical thrust requirements), for the Mini-E this was not the case, with a distinct reduction of the rotors' speed being verified with the increasing magnitude of the frontal gusts due to the action of its lifting surfaces.

Y-Wise Gusts

Next, the case of lateral gusts was analysed, with the following results respecting once more the reasoning that left-coming gusts are represented by the negative values of the lateral gust speed and right-coming gusts being associated to positive values. On this analysis a limitation in the range of gusts that was analysed was verified since for magnitudes over $9\,m/s$ of left-coming gusts the value defined as the maximum frontal arm's tilting angle ($\delta_{arms} = 15°$) was exceeded. These limits may be expanded if the final aircraft is able to tilt the front rotors over this value.

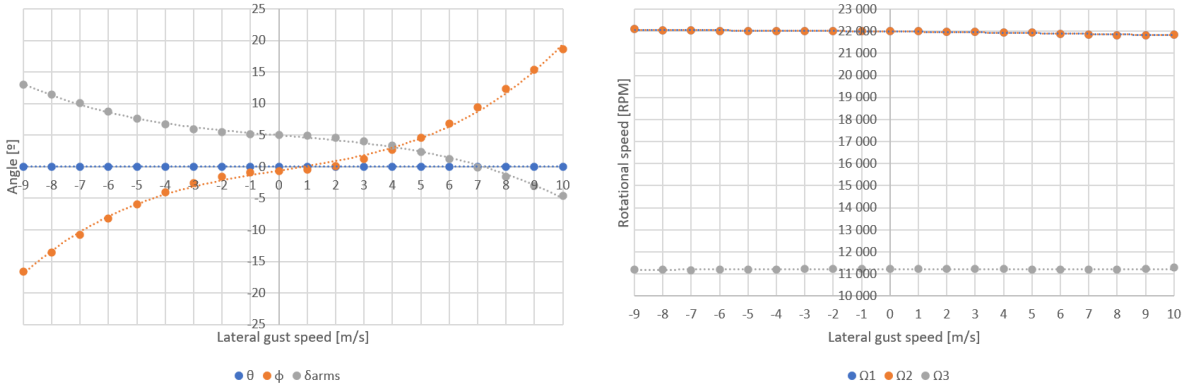

(a) Evolution of the roll and arms' tilting angle with the value of the lateral gust.

(b) Evolution of the rotors' rotating speeds with the value of the lateral gust.

Figure 3.10: Results from the parametric study of the test vehicle's behaviour under the influence of lateral gusts.

From the results shown (Fig. 3.10), one can start by examining the second graph, showing the evolution of the rotational speed of the rotors with the magnitude and direction of the lateral gusts. From this, it is possible to realize that the rear rotor speed remains approximately constant throughout the range of velocities analysed, whereas the frontal rotors' speed is approximately constant throughout the range of magnitudes of the left-coming gusts. For right-coming gusts there is a slight decrease in rotor speed with the increasing gust magnitude.

From the first graph, it is clear that the direction and magnitude of the lateral gusts has no effect on the pitching angle of the aircraft, which remains null throughout the range. The same cannot be said of the roll angle. For left-coming gusts the aircraft reveals a tendency to bank to the left and to do the contrary when dealing with right-coming gusts. This behaviour is expected, following the same line of thought as previously employed for the relation between longitudinal gusts and pitch angle. The roll angle assumed by the aircraft when the magnitude of the gusts approaches both limits of the analysed range

is, however, quite expressive, leading to the development of a considerable lateral local component of the gravitational force. To counteract it the frontal arms tilt in the opposite sense to the roll in order to generate a lateral thrust vector that balances this developing lateral component of the gravitational force. This evolution of δ_{arms} is approximately symmetric with a bias of $+5.0°$ for the value of δ_{arms} and $-0.7°$ for ϕ as these are the values assumed in trimmed conditions.

Z-Wise Gusts

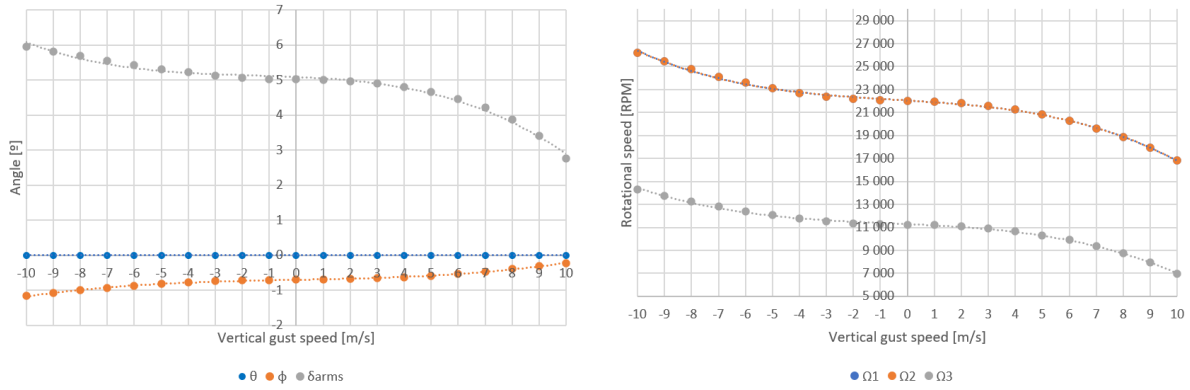

(a) Evolution of the roll and arms' tilting angle with the value of the vertical gust.

(b) Evolution of the rotors' rotating speeds with the value of the vertical gust.

Figure 3.11: Results from the parametric study of the test vehicle's behaviour under the influence of vertical gusts.

From the analysis of the graphs represented in Figure 3.11 it is possible to note that the pitch angle remains null throughout the entire range of vertical gust velocities analysed, whereas the roll angle presents relatively small changes. For upward gusts the bank angle magnitude tends to be reduced from $0.7°$ (in the negative sense), approaching $0°$ as the magnitude of the gusts increases. This is also associated to a reduction on the tilting angle of the frontal rotor arms (reducing the lateral contribution of thrust) which in turn is due to the noticeable reduction of all of the rotors' rotational speed since the developing drag force points upwards, resulting in less lift needed to be generated by the rotors, which leads to the drag torque developed by them to be reduced.

For the case of downward gusts, the resulting drag force will point downwards, alongside the aircraft's weight. As so, the rotors will need to generate more lift, their rotational speed increases and so does the overall drag torque developed by the rotating propellers. This results in a larger lateral thrust component being needed to balance the moments around the yaw axis and so δ_{arms} is increased. Simultaneously, to balance the forces in y, the roll angle increases (in the negative sense) as to increase the lateral contribution of gravity.

An initial flight envelope can also be drafted for this vehicle in hovering conditions, as presented in Table 3.9. The aerodynamics model used to obtain these results is, however, severely simplified, in a way that such values should be considered with caution in the development of future flight test plans.

Table 3.9: Maximum allowable gust magnitude in each direction.

Gust direction	**Front**	**Rear**	**Left**	**Right**	**Up**	**Down**
Maximum allowable magnitude (m/s)	>10	>10	9	>10	>10	>10

Rear Tilt Angle

This last analysis will be performed solely for purposes of understanding how the test vehicle will perform under a tilting action of the rear rotor. Since this vehicle does not have any lifting surfaces, there is no transition between flight modes to be performed in a way that this tilting action will only be performed to prove the concept of the rear rotor tilting mechanism and the ability of the developed autopilot to handle forward flight. As so, once more, the pitch angle was fixed at $0°$, simulating a leveled transition. This analysis was performed, as in 3.2.1, by feeding variable forward speeds to the optimization algorithm with the goal of determining the attitude and actuation (including the rear tilting angle, μ) that would provide an equilibrium condition of steady, leveled, forward flight. Unlike what was done for the case of the Mini-E, the rudder deflection angle was not considered since this control surface does not exist in the test vehicle.

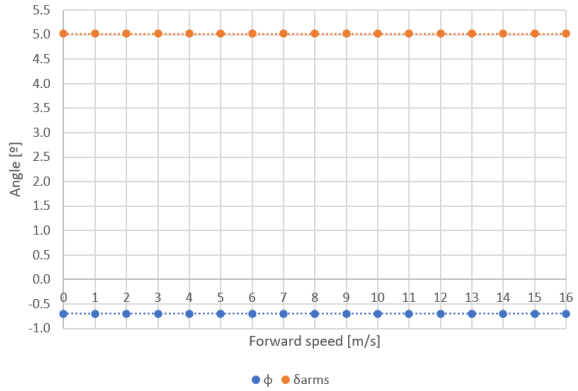

(a) Evolution of the roll and arms' tilting angle with the forward speed.

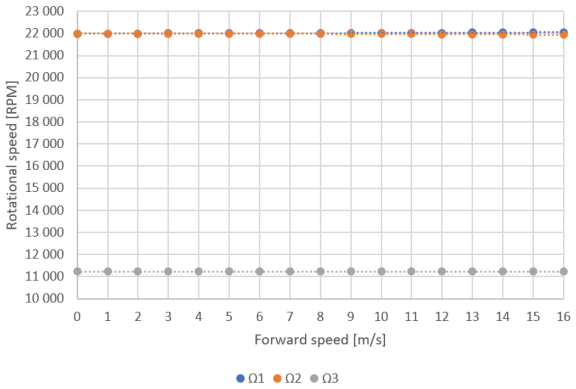

(b) Evolution of the rotors' rotating speeds with the forward speed.

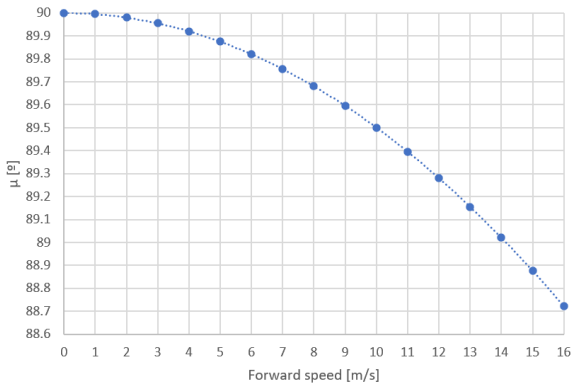

(c) Evolution of the rear tilting angle, μ, with forward speed.

Figure 3.12: Results from the parametric study of the test vehicle's behaviour under different forward speeds.

From the results provided in Figure 3.12, it is possible to understand that throughout the range of analysed forward velocities the vehicle's attitude, frontal arms tilting angle and rotor's rotational speed suffers little to no variation. From the analysis of the last graph it is possible to realize that the angle at which equilibrium is achieved throughout the range is relatively small, denoting that very small deflections of the rear tilting mechanism will result in quite expressive variations in the forward speed of the test aircraft. Due to the small deflections required to gain forward momentum, the rear thrust vector is always maintained close to vertical in a way that the increase in thrust required from it to maintain an equilibrium condition is negligible ($1.4\,rpm$ between the two limits of the range in this analysis). As so, almost no variation in attitude is recorded between hovering and forward flight. It is important to remember once more, that the aerodynamic model used is quite simple and may be underestimating the magnitude of the drag force being developed.

3.3 PixHawk® Controller Implementation

In order to achieve the stabilization and control required to fly this novel drone configuration, the $PixHawk$® 4 board [50] was elected running the $PX4$ flight controller firmware [25]. In order to communicate with the vehicle $QGroundControl$ [51] was used.

The first step that was taken in order to obtain an appropriate flight controller for our configuration was to investigate what had already been done in the field of tri-rotor control using the $PX4$ firmware. From this research, it was found that, as expected, no configuration such as the one analysed in this work had already been approached. Nevertheless, this firmware had already been used to control other, more common, configurations of tri-rotors.

As so, two tri-rotor airframes were already available in $QGroundControl$ (Figure 3.13): the *Tricopter Y+* and the *Tricopter Y-* [52]. These share the characteristic of all of the rotors being equidistant from the aircraft's CG, which means that, in leveled hovering conditions, all of the motors are equally loaded. These configurations also share the common characteristic of only one of the rotors tilting to achieve equilibrium in the yaw axis (due to the uneven number of propellers). Furthermore, after careful analysis of the $PX4$ firmware code in which these airframe configurations were defined it was found that all of the motors were also modeled as equal, as expected, and that the only difference between both configurations was related to the sense of rotation of the propellers, which in turn defined the primary tilting direction of the rear rotor. While all the propellers on the Y+ configuration rotate in a counterclockwise sense, in the Y- configuration all of them rotate clockwise. This means that without the action of the rear tilting mechanism, the Y+ configuration has a tendency of yawing in the positive sense of the z axis (clockwise) while the *Y-* tends to rotate in the negative sense (counterclockwise). This natural tendency of yawing in such directions defines that the rear rotor of the *Y+* configuration will mainly rotate to the right, in order to obtain a positive y thrust component which balances the existing sum of the drag torques of the three rotating propellers whereas for the *Y-* configuration the opposite will be true, with the rear rotor tilting primarily to the left.

After analysing the existing configurations it was defined that these would serve as a starting point

(a) Y+ tricopter configuration. (b) Y- tricopter configuration.

Figure 3.13: Pre-existing tri-rotor configurations in the $PX4$ Autopilot firmware.

for the custom controller required to fly our novel tri-rotor configuration.

The next step in the development of this custom flight controller was defining how to feed the characteristics of our custom configuration to the $PX4$ firmware in order for the flight controller to allocate the correct controls to the actuators. After some research, namely of the documentation curated by the original $PX4$ software developers and available in the $PX4$ User Guide [53], it was possible to identify two main paths that could be followed to obtain an Autopilot firmware that could be uploaded to the $PixHawk$ ® board and that would, theoretically, be able to control a custom configuration aircraft: overriding the existent mixer matrix file through the upload of a *.txt* file to the $PixHawk$'s ® SD card or developing a new, custom, $PX4$ airframe. The later path was followed since it provided the most intelligible and robust solution to the problem.

3.3.1 Custom Airframe Development

The pursued solution was then the development of a custom $PX4$ airframe to be flashed onto the $PixHawk$ ® 4 board through the $PX4$ autopilot firmware alongside the pre-existent ones. In order to do so, three files needed to be created, the first was the *configuration file*, where the default initialization parameters can be altered, namely the different flags that control the various properties of the flight controller and where the mixer matrix file of the airframe which control is required is called. Hence, it was also necessary to create a custom *mixer file* where the table of influence of the different actuators over the different control axis of the aircraft is provided. The $PX4$ autopilot code has the particularity of developing its own mixer matrix for any kind of conventional multirotor given that the geometry of such vehicle is provided. This means that, by providing a third file, where the *geometry* of the vehicle is depicted, the code will then take this geometry and derive a custom mixer matrix depending on the distance between the rotors and the CG of the aircraft, the sense of rotation of the propellers, the orientation of the rotors and two constants, Ct and Cm which translate the thrust developed by each rotor relative to a reference rotor (in the case of all being equal all of them have a Ct of 1) and the drag torque developed by such rotor where Cm is obtained by dividing a reference value of the drag torque developed by the rotor by the thrust provided by it for that regime.

It is important to note, however, that the code which interprets the geometry file is only able to develop a mixer matrix for multirotors with fixed rotors, i.e., it can not model the tilting of the rotors. As so, in the mixer matrix file, although this function which returns the mixer matrix based on the provided geometry

was called to create the mixer matrix of the three rotors, additional information was needed to model the influence of the tilting mechanism upon the dynamics of the aircraft, particularly its authority over the yaw axis of the vehicle.

The geometry code can also be manipulated with the intention of personalizing the way the flight controller (FC) interacts with the aircraft. In the case of the test vehicle developed it was found, through the calculation of the mixer matrix, that the action of varying the rotor speed to achieve control over the yaw axis of the aircraft was much less effective than the thrust vectorization that could be achieved by the action of the frontal tilt mechanism. Furthermore, taking into account the specificities of the configuration at hands, namely that the two front rotors rotate in the same direction, opposite to the one of the rear rotor, it became clear that, in the instance of the FC altering the rotational speed of the rotors relative to each other to achieve control in yaw by altering the accumulated drag torques developed by the rotating propellers, the aircraft would have an undesired coupled pitching action. In order to avoid this undesirable coupling of yawing and pitching motions, it was defined that, given the small relative weight of the action of the drag torques when compared to the tilting action of the front rotors, the yaw axis control would depend solely on the action of the tilting mechanism whereas the control of the roll and pitch axis would rest on the variation of the rotors' rotational speed. This was achieved by defining the Cm parameter of the three rotors as zero, which makes the controller assume that the variation of the rotational speed on the propellers will not take effect upon the yawing motion of the aircraft. In parallel, the frontal tilt mechanism's mixer matrix was defined in order for this system to deal solely with the control of the yaw axis. In order to achieve yawing stability in hover flight a trim value can be provided to the frontal tilt mechanism. This way, in nominal conditions, the aircraft will be balanced and a variation of the tilting angle will only be required when these conditions are altered.

The *configuration*, *mixer* and *geometry files* developed are available in appendix A and were based on the pre-existing files of tri-rotor configurations. In order to get these files to be read by the software when the controller was compiled it was also required to alter the *CMake* files present in the respective folders in order for the compiler to take into account the added files alongside the pre-existing ones.

When all the files were placed in the correct directories, and the respective CMake files altered, it was necessary to compile the $PX4$ autopilot code as to obtain a $.px4$ file that could be flashed onto the $PixHawk$® board through $QGroundControl$. This $.px4$ file is a zipped JSON file which contains the airframe metadata and is obtained by compiling the $PX4$ code in a Linux environment. For the case of our aircraft this was done by running the *Ubuntu 18.04* operating system on a virtual machine.

Upon obtaining the *.px4* file this was flashed to the board using $QGroundControl$ and the configuration became immediately available to be used on the "Airframe" tab.

In order to perform an initial assessment of the controller's performance prior to flight testing, the test vehicle was armed in a similar fashion as it would be in a real flight test (without the propellers being mounted on the motors) and inputs were provided both through the transmitter and through the manipulation of the aircraft (introduce pitch, roll or yaw) to see how the actuators behaved. This procedure allowed to confirm, even though only in a qualitative way, that the controller acted upon the correct actuators under the various circumstances.

Chapter 4

Airframe and Systems Sizing

From the beginning of the design of the novel VTOL aircraft configuration that serves as case study for this work it became clear that a new type of actuating systems needed to be developed. Analysing the suggested design it becomes evident that, by having an uneven number of rotors, it will be necessary to resort to a tilting action of some of the rotors to achieve an equilibrium condition for the moments acting upon the aircraft around the yaw axis. With an even number of rotors this is usually achieved by having the same number of rotors rotating in a clockwise (CW) sense as the number of rotors rotating counter-clockwise (CCW). This pairing allows for the drag torque developed by each propeller in hover to be balanced by an equal and opposite torque developed by a similar propeller rotating in the opposite sense. The management of the rotational speed of the propellers relative to each other is also used as a strategy to maneuver the aircraft around its yaw axis.

For the case of tri-rotors, and since it is quite difficult to guarantee an equilibrium of moments around the yaw axis with the use of fixed pitch propellers, given that it is not possible to implement such a pairing strategy, it becomes necessary to achieve this balance by other means. The most common approach [11–13] is to have two paired, ”frontal” rotors and the third, unpaired, ”aft” rotor, able to tilt laterally, i.e., around the arm on which it is mounted, in order to create a lateral component of thrust that allows the moments to be balanced around the yaw axis, as represented in Figure 4.1.

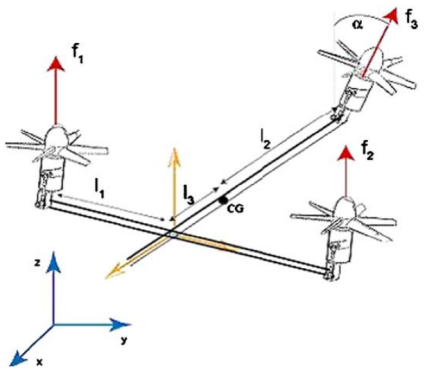

Figure 4.1: Previously studied tri-rotor configuration (S. Salazar-Cruz et al. 2009) [11].

Despite the existing research work that exists on such tri-rotor configuration, that design can not be applied to the intended aircraft for two main reasons. The first is related to the fact that the final version of the aircraft, for which the Mini-E is used as a prototype, will most likely have an hybrid propulsion system, with the frontal rotors being powered by electric motors and the rear propeller being driven by a combustion engine. As so, it was defined that this engine should be fixed to the aircraft's airframe, thus being unable to tilt in solidarity with the propeller. This however, does not serve as a reason for neglecting this pre-existing design right away, as a gearbox could be mounted between the fixed-position input shaft and propeller output shaft, which would be able to pivot to the left or to the right according to the demands of the controller. However, when combining this hard-constraint of having a fixed motor driving the rear propeller with the requirement of such rotor providing thrust in forward flight, the use of said design becomes quite difficult since the propeller axis would have to pivot now not only laterally but also between a vertical and an horizontal stance in order to provide thrust in both the vertical and horizontal sections of the flight. As so, it was determined that the rear rotor would only tilt from upright to horizontal.

Then, it was deemed necessary to equip the frontal arms with tilting abilities in order to manage the torque balance along the yaw axis. Both arms will be actuated since the frontal motors will be considerably less powerful than the rear one and therefore the required increase in the thrust output necessary to maintain an equilibrium of forces in the vertical direction while developing a lateral component of thrust should be shared between the two frontal motors. This way both frontal rotors will rotate simultaneously, by the same angle δ_{arms} around their respective arms' axis, developing similar lateral components of thrust and thus the desired moment around the aircraft's yaw axis. Since the arms have an opening angle relative to the local y axis (Γ), a longitudinal component of thrust will also be developed by the tilting rotors. However, the two components developed will, in normal conditions (both rotors having the same rotational speed), be canceled, as one will develop a positive component and the other a negative one, therefore maintaining an equilibrium of forces in x.

The behaviour of such an aircraft under different flight conditions was already studied in Chapter 3. Now, a description of the choices made during the process of designing the actuator mechanisms for this novel configuration, multi-rotor, aircraft will be made.

This VTOL propulsion system will have five distinct actuation inputs. In vertical flight mode only four will be used, the three, individually controllable, rotors' speed and the tilting of the frontal arms for the reasons enunciated previously. The fifth actuator, which will be used solely in the transition phase of vertical to forward flight will be the tilting action of the rear rotor.

An extra actuator may be considered in future iterations as, according to the initial concept, the frontal arms shall retract into the fuselage during forward flight, in order to minimize the overall drag developed in this flight stage. This way, this mechanism will also need to be modeled simultaneously to the final frontal tilt mechanism design. This actuator will not, however, have a direct influence on the aircraft's performance in hovering flight (considering that the weight of the aircraft is constant, i.e., the battery mass will change according to this mechanism's weight) unlike the other five, in a way that this will not be developed for the initial aircraft that shall be designed to test the conceptual design here explored.

The rear tilting mechanism, however, is considered to have influence in the vertical phase of the aircraft's mission, since power will need to be transmitted from the fixed motor to the propeller shaft by means of a gearbox, which can influence the performance of the aircraft in VTOL mode.

The conceptual design phase of the mechanisms that shall be presented next was lengthy and consisted of multiple iterations. To begin, the basic requirements were defined, namely that the obtained designs should be as simple and light as possible and that the systems designed for the test vehicle could later be scaled up for application in the Mini-E aircraft. Additionally, off-the-shelf parts were prioritized in relation to custom built ones due to the ease of buying replacements and to the fact that items such as the gearbox needed for the rear tilting mechanism would already have been tested in other applications, unlike a custom made gearbox which would have, itself, to be tested prior to assembly in the complete mechanism.

Therefore, some initial designs were proposed for both the front and rear tilt mechanisms and those were reviewed by several members of the team, with the various discussions resulting in the evolution of the initial designs until the ones that shall be presented next.

In the following sections a brief description of the most notorious constraints affecting each mechanism will be provided, as well as an explanation for the various design options taken. Some of the testing done during this phase will be presented as well as the mapping of the tilting mechanisms action. An analysis of the final weight of the systems will also be carried out.

4.1 MTOM Assumptions

In order to begin the sizing of the test vehicle, an initial MTOM value needed to be estimated. The first step towards obtaining this initial value was to estimate some preliminary masses of the major subsystems of the aircraft. As so, the values present in Table 4.1 were initially suggested, serving mostly as targets for the sizing of the motors and throughout the design of the different subsystems. Such masses were estimated based on preliminary weighing of some of the parts required to fly the aircraft, such as the autopilot components and available batteries, generic electric motors and Electronic Speed Controllers (ESCs) and also from empirical knowledge acquired from previous projects [54].

Table 4.1: Initial mass estimation.

Subsystem	**Mass (g)**
Airframe	100
Tilt mechanisms	500
Battery	200
Electronics	300
Total	1100

4.2 Procurement of Motors, Propellers and ESCs

From the suggested MTOM value, and under normal operating, hovering conditions, each front rotor will be responsible for managing around 10% of the overall weight whereas the rear one will carry 80% of it. A procurement of adequate components was then necessary to proceed with the sizing of the aircraft.

These components are meant to work alongside a *Turnigy Nano-Tech 1600 mAh, 4S, 50C* battery. This choice was made due to existing multiple batteries of such model available at CfAR, allowing to perform all the intended flight testing without the need to recharge or use different models, thus keeping the mass and inertial characteristics of the vehicle constant throughout the various tests.

4.2.1 Front Rotors

The location of the CG in the proposed concept, associated to the initial estimation of the MTOM, will result in the front rotors being required to generate around $110\,g$ of thrust in hovering conditions. Considering a safety factor of 1.5 to account for the needs of additional thrust to perform manoeuvres and for probable discrepancies between the data supplied by the manufacturer and the results indeed obtained, it was decided that the frontal motors should develop at least $165\,g$ of thrust. As so, it was decided to use a pair of *iFlight XING 1404 3000 KV* motors [55]. These power units were chosen due to their performance, low weight and availability in a short time frame.

According to the manufacturer's test reports the chosen motors can deliver, when used with a 4 cell battery (as intended) and a two blade propeller with a diameter of $4\,inches$ and a pitch of $2.5\,inches$ [56], a maximum thrust figure of $553\,g$.

When it came to the choice of Electronic Speed Controllers for the front motors, this rested on the *T-Motor Air 20A 4S* [57] due to the fact that such ESCs had a maximum allowable continuous current above the one required as well as an appropriate input voltage to run the chosen motors while only weighing $32g$ each. Furthermore, they were immediately available at CfAR.

Upon arrival of the motors and propellers, static thrust tests were conducted with the results being available in 4.5.1.

4.2.2 Rear Rotor

When it comes to the motor that was chosen to power the rear propeller, the chosen model was the *iFlight XING 2806.5 1300 KV* [58] due to the fact that, according to the manufacturer's specification sheets it provided more than enough thrust to sustain 80% of the aircraft's weight with a safety factor of 1.5 in place and to the immediate availability. The chosen three-bladed propeller had a diameter of $7\,in$ and $4\,in$ of pitch [59].

The ESC that was chosen to be paired with this motor was the *T-Motor T80A* [60], once again due to having an allowable output current above the required one while also being available at CfAR for immediate use. In terms of mass this ESC weighs in at $62g$.

In order to provide a comparison term between the power consumed to generate a specific thrust

figure for the rear rotor in direct drive (propeller directly mounted on the motor) against the performance verified when power is transmitted through the designed system, static thrust tests were performed. These obtained results shall be analysed in subsection 4.5.1.

4.3 Airframe

Since the initial concepts were developed with the test vehicle in mind, some dimensions needed to be defined from the start in order to guide the development of the entire tri-rotor aircraft. Therefore, the Mini-E's dimensions (which were provided in [27]) were analysed, as well as some limiting dimensions of the materials intended to be used for the assembly of the test tri-rotor. It was determined that the airframe of the aircraft was going to be built using a combination of balsa and plywood. These materials, widely used in the field of model aircraft development, were chosen due to the fact that they were inexpensive, easy to process, to repair, compatible and allowed for obtaining a light, but strong, frame while being available immediately.

In order to reduce the overall weight of this structure and to facilitate the assembly of the electronic components onto the vehicle, a series of holes were opened throughout the entire structure, taking into account, however, the conservation of the structural integrity of the parts.

The CAD representation of the designed structure can be found in Figure 4.2.

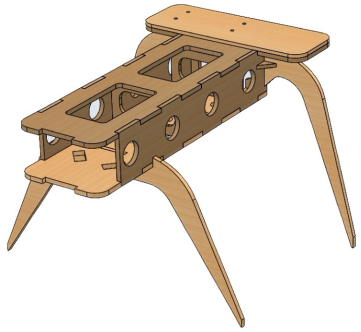

Figure 4.2: CAD model of the test tri-rotor's airframe.

4.4 Tilt Mechanisms

4.4.1 Front Mechanism

The frontal tilt mechanism is required to allow for the rotation of the frontal arms of the tri-rotor along their respective axis. This rotating action should be performed by the two rotors in solidarity, i.e., they should turn in the same direction simultaneously. However, in an effort to allow for future changes of the configuration to occur if the results yielding from the test flights are not satisfactory, and to provide redundancy to the system, a choice was made to equip the test vehicle with the ability to rotate each frontal arm independently if required. As so, the tilting action of each arm is achieved by the use of an assigned servo-motor. Nevertheless, both servos will be controlled by a single input signal in the current configuration. This choice will also facilitate the later development of the arms' retraction mechanism (7.3).

In this subsection, the components which are a part of the final iteration of the front tilt mechanism will be presented, as well as the choice of material and manufacture technique (when the component

was fabricated by the author at CfAR) associated to each. Furthermore, some stress and displacement studies will be carried out in order to validate the design choices.

Components

The list of components which compose the front tilt mechanism is available in Table 4.2. The numbering followed is respective to the numbering available in Figure 4.3, where a CAD representation of the final design is presented. Fast prototyping techniques such as 3D printing and turning were used when possible as to minimize the time between iterations and required to manufacture replacement parts.

Table 4.2: Front tilt mechanism components.

	Name	Material	Manufacturing technique	Amount	Mass [g]
1	MKS HBL 6625	(Various)	-	2	27.85
2	Servo horn	Plastic	-	2	0.50
3	Linkage	(Various)	-	2	2.14
4	Control arm	PLA	3D printing	2	1.06
5	Support	PLA	3D printing	1	31.39
6	Bushing	PTFE	Turning	2	25.13
7	Carbon arm	CFRP	-	2	7.73
8	Collar	Aluminium	-	2	8.50
9	Motor support	PLA	3D printing	2	1.38
10	XING 1404	(Various)	-	2	9.30
11	Gemfan 4024	Poly-carbonate	-	2	2.70
				Total	203.97

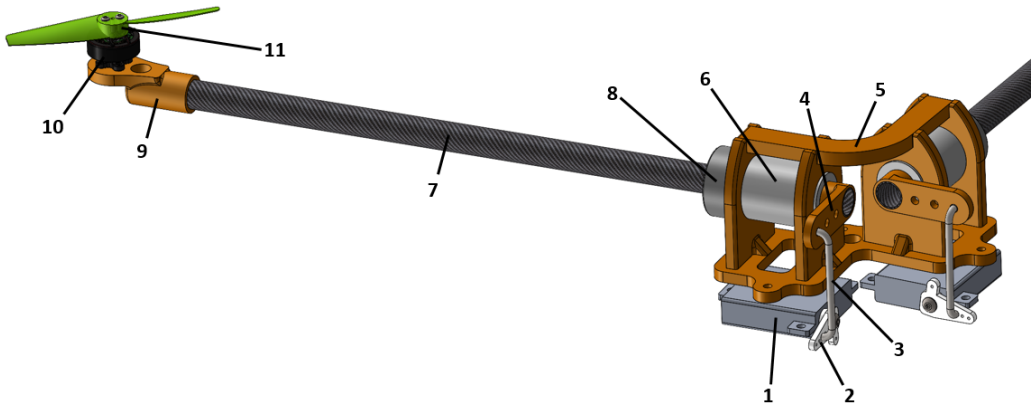

Figure 4.3: CAD model of the final front mechanism assembly.

The design of some and the choice of other elements carried some specificities with it, namely:

- *MKS HBL 6625* - this servo was chosen to be used both in the front and rear mechanisms due to its immediate availability, high load capacity and proven reliability.
- *Linkage* - the chosen linkage had the particularity of being adjustable in length, which facilitated the fine tuning of the tilting mechanism. Furthermore, by having ball bearing ends, it allows for

some light misalignment to occur while maintaining a friction-less interaction with the horn and control arm to which it is attached.

- *Control arms* - this part was designed specifically for this build. The main characteristic which distinguishes this arm is the mounting on the carbon tube. By functioning as an outside sleeve for the tube (to which it was glued) it allows for the passing of the extended motor wires from the tube to an aft region of the aircraft where the ESCs are located. Its dimension was also tuned for maximum control precision while respecting the dimensional limitations of the build.

- *Support* - this assembly was initially designed to be built using machined carbon based (sandwich) composite parts, however, it was later determined that the weight difference in relation to 3D printing would be minimal while the later manufacturing method allowed for quicker prototyping. The support consists of a base part, which defines the opening angle of the arms and that is fixed, using bolts, to the base of the wood frame, four vertical parts that accommodate the bushings (each bushing has two zones of a reduced diameter relative to the center section where they fit to the vertical supports) and a top part which prevents any relative movement to happen between the vertical parts. The height of this support was defined as the maximum vertical space available inside the wood structure, thus providing a snug fit.

- *Bushings* - the chosen material for these parts was polytetrafluoroethylene (PTFE), a synthetic polymer which is known for the very low friction coefficient it provides [61]. These were designed to offer support to the carbon tubes while distributing the loads transmitted from these to the front tilt mechanism support, which in term would transmit them to the airframe. Furthermore, these should allow for the rotating motion of the arms. Initially, roller bearings were chosen for this purpose, however, the choice turned to bushings due to not having any moving parts which could suffer damage and hinder the well functioning of the system. Silicone grease was applied to the inner face of the bushings to further facilitate the rotating motion of the carbon tubes.

- *Carbon arms* - carbon tubes were chosen for the arms given their satisfactory mechanical properties and low weight. The final length of these arms was defined based on some trade-off decisions that shall be presented in subsection 4.4.1.

- *Collars* - these were used to limit the longitudinal travel of the tubes.

- *Motor supports* - these parts were designed to have the smallest rotor coverage area possible while being robust enough to sustain the loads of the rotors. Furthermore, these allow for the passing of the motor wires into the carbon tubes in a similar fashion to the *Control arms*.

Loads Estimation

The definition of the arms' material took into consideration the materials available in the workshop. As so, $10\,mm$ diameter (pultruded) carbon fiber tubes were selected. The main criteria for the choice of this material was the minimization of the deflection of the arm when subjected to a force applied at the tip

(such as the thrust force generated by the motors) and the overall weight. By minimizing such deflections one can ensure that the thrust vectoring is performed as intended by the autopilot. Furthermore, this material presents quite satisfactory mechanical properties which should assure that it will not break during flight tests even if there is a shock.

Some simple calculations were performed where a range of possible arm lengths was considered ($50\,mm$ to $500\,mm$). The first study performed was related to the deflection at the tip when the front rotor is providing the maximum possible thrust (from the motor supplier's test sheets). In order to model this behaviour, the classical formulas for the cantilevered beam were used [62]. Firstly, the bending moment (M) at a certain point of the tube is taken as being the product of the thrust force (T) by the difference between the tube's length, L, and the z coordinate of the point. Then, the equality $M = EIv''$ is used, where the bending moment M is related to the second derivative of the displacements, v'' by means of the tube section's second moment of area I and the material's Young modulus, E, which together yield the cantilever's flexural rigidity EI. Through integration and simple algebraic manipulation and considering the boundary conditions of our problem ($v'(z = 0) = 0$ and $v(z = 0) = 0$), the following formula can be obtained for the maximum deflection (i.e., at the tip of the arms):

$$v_{max} = \frac{TL^3}{3EI} \tag{4.1}$$

Additionally, it is also necessary to determine how the material handles the stress at which it is exposed due to the force being exerted at the tip. This load will result in a shear force and in a bending moment which will be maximum at the constrained end of the tube, as it is the point of the beam furthest away from the application point of the force.

Lets consider the formula for the direct stress distribution along a section of the beam:

$$\sigma_z = \left(\frac{M_y I_{xx} - M_x I_{xy}}{I_{xx} I_{yy} - I_{xy}^2}\right) x + \left(\frac{M_x I_{yy} - M_y I_{xy}}{I_{xx} I_{yy} - I_{xy}^2}\right) y \tag{4.2}$$

Considering that the chosen, circular, tube has an outer diameter of $10\,mm$, an inner diameter of $9\,mm$, that the thrust force is modeled as being applied vertically and upwards and that $I_{xy} = 0$ due to symmetry, the maximum direct stresses will be registered in the points where y is of greatest module, i.e., the upper and lower points of the outer diameter. The direct stress registered in both of these points will be equal in module but different in sign as there will be compression in the upper point and traction in the lower one. Equation 4.2 can thus be simplified, yielding:

$$\sigma_z = \frac{M}{I} y \tag{4.3}$$

I is the second moment of area of the tube section and is defined by $I = (\pi/64)(D^4 - d^4)$, where D stands for the outer diameter and d for the inner one. Since M, the bending moment, will be maximum for $z = 0$, σ_z will also be maximum in this section and so it was the one where the study of the maximum direct stress absolute value was performed.

When it comes to the shear stress, and by making the assumption of the load being applied in the

vertical symmetry axis of the tube's cross section, and applying the common shear formulas for a closed cell [62], equation 4.4 can be derived, where α is null at the bottom point of the circular cross section of the tube and takes the value of $180°$ at the top point.

$$\tau = \frac{Tr^2 \sin \alpha}{I} \tag{4.4}$$

The representation of the evolution of both the maximum (tip) deflection and of the maximum direct stress felt at the constrained end of the carbon tube can be seen in Figure 4.4 alongside Table 4.3 where some guideline values used in this investigation are depicted.

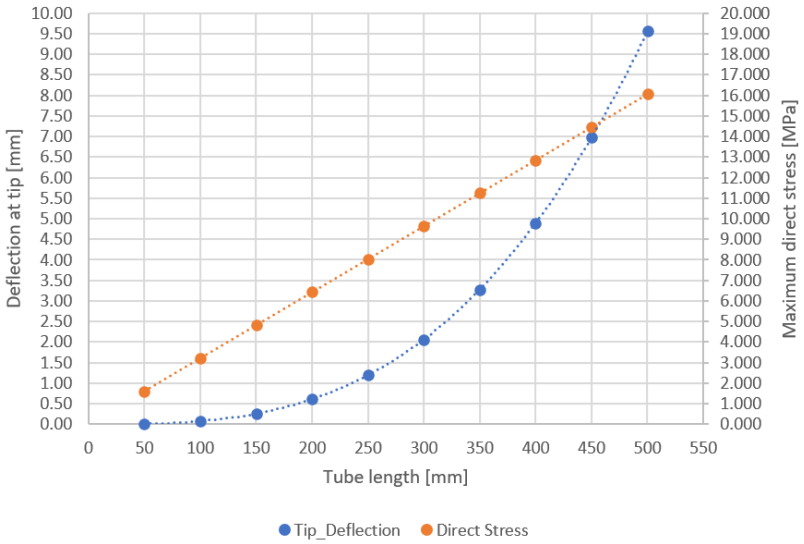

Figure 4.4: Deflections at the tip and maximum normal stress variation with the tube's length.

Table 4.3: Reference values for carbon fiber composites.

Tensile Modulus	140 GPa
Bending Strength [63]	299 MPa
Maximum allowable shear stress [64]	91.2 MPa

As for the maximum shear stress computed under maximum theoretical thrust conditions, this value amounts to $2.9\,MPa$, well under the limit value presented in Table 4.3.

The results provided above show that the carbon tubes can easily support the type of loads that will be present when serving as the tri-rotor's arms regardless of their length (within the studied range), not posing as a limiting factor in the design choices made. However, the length of such components is yet to be defined.

As referred earlier in 3.2.1, it was determined that the arms' opening angle, Γ, that would allow for a minimization of the tilting action of the frontal rotors in hovering conditions would be around $61.1°$. However, a concession needed to be made due to three factors:

- Due to the limited width of the frame where the tilt mechanisms would be mounted and since symmetry was desired due to weight distribution reasons, it was impossible to place both servos

in the intended place with a Γ as high as $61.1°$;

- In order to have the desired CG location for achieving the proof of concept, while respecting the dimensions previously defined for the rotor positioning, it was determined that, with an opening angle of the arms of $61.1°$, the total arm length would be around $424\,mm$. From the data provided above, one can determine that the deflection at the tip would then be of $5.8\,mm$ in a way that it was deemed desirable to take advantage of the cubic evolution of tip deflection with the tube's length to try and minimize this value.
- With the previously determined value of the arms' opening angle, and respecting the dimensions that were defined in 3.7, the frontal tilting mechanism was located in a more aft position of the airframe than desired, making it difficult to fit all of the electronic components needed to fly the aircraft in the space available.

As so, it was decided to shift the frontal tilt mechanism forward, reducing the arms' length, the maximum deflection at the tip, the maximum direct stress created at the arms' support region and gaining valuable space for the needed electronic systems. Furthermore, by reducing the arms' length it becomes easier, in a future design, to accommodate such parts inside the fuselage when it is time to retract them during horizontal flight. As so, and as already mentioned in 3.2.1, the arms' opening angle was fixed at $43°$, which meant that the tubes' length would be of around $280\,mm$ with a maximum tip deflection of $1.68\,mm$.

4.4.2 Rear Mechanism

The rear tilting mechanism will not serve as a primary control actuator in vertical flight conditions. However given the constraints previously imposed, namely that the final aircraft's rear motor will likely be a combustion engine, it is important to model the behaviour of the configuration featuring already a tilting mechanism. This will serve not only to test the dynamics of the VTOL system when small tilting angles are introduced but also to account for the dynamics of the required $90°$ gearbox into the system as a whole. The use of such gearbox presupposes that the motor shaft will be aligned with its input shaft, and that to achieve the required rotation of the output shaft the entire mechanism should allow tilting in such a way that the pivoting axis of the entire gearbox is always aligned with said input shaft.

Components

The list of components which comprise this system is presented in Table 4.4, with the corresponding numbering being available in the CAD representation provided in Figure 4.5.

The choice of some components that are common to the front mechanism was based on the same reasons, while other, rear mechanism specific, components were chosen/designed this way due to reasons such as:

- *Servo horn* - a custom size servo horn was designed in order to achieve the required tilt resolution;

Table 4.4: Rear tilt mechanism components.

	Name	Material	Manufacturing technique	Amount	Mass [g]
1	MKS HBL 6625	(Various)	-	1	27.85
2	Servo horn	PLA	3D printing	1	0.50
3	Linkage	(Various)	-	1	2.14
4	Gearbox control arm	Aluminium	Machining	1	4.18
5	Gearbox	(Various)	-	1	83.00
6	Bushings	PTFE	Turning	2	8.82
7	Ball bearings	Steel	-	2	11.50
8	Flexible shaft coupling	Steel/Rubber	-	1	19.00
9	XING 2806.5	(Various)	-	1	49.50
10	Propeller shaft	Aluminium	-	1	35.00
11	Gemfan 7040	Poly-carbonate	-	1	7.90
12	Support	PLA	3D printing	1	69.56

Total	339.27

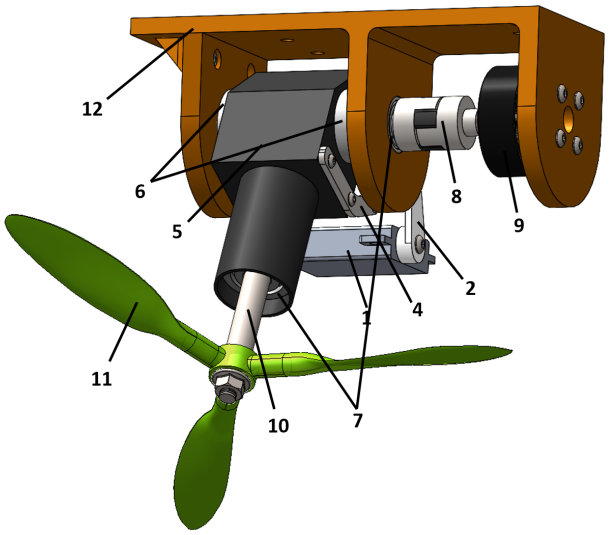

Figure 4.5: CAD model of the final rear mechanism assembly.

- *Gearbox* - the initial intention was to build a custom gearbox, however, it was found that by using an off-the-shelf part significant weight and cost savings could be made. Moreover, an off-the-shelf part would have already been tested previously and it is known to work within the limits provided by the manufacturer. As so, it was decided to opt for an helicopter rear rotor gearbox, more precisely a gearbox used in RC aerobatic helicopters. The chosen gearbox model was the one present in the $Align\,T-Rex\,700e$ [65] due to the fact that an unit was already available in the workshop and ready to be tested. This type of gearboxes are required to resist considerable power and torque

figures due to the fact that this particular helicopter model is usually used for aerobatic flight. The gearbox was modded to fit an extra *roller bearing* inside the sleeve on which the *propeller shaft* enters in order to ensure its correct alignment at all times and prevent vibrations.

- *Gearbox control arm* - this part was custom designed to control the tilting movement of the gearbox, being connected to the *linkage*.

- *Bushings* - these PTFE parts support the gearbox, ensuring the maintenance of the required alignments while allowing for slow rotating motions to occur such as the intended tilting action.

- *Flexible shaft coupling* - this component was introduced as a way to connect the motor's shaft to the gearbox's input one. This coupling serves both the obvious purpose of transmitting power between the two shafts and of absorbing some slight misalignment or vibrations that may occur during the system's operation.

4.5 Experimental Testing and Results

4.5.1 Thrust Tests

In order to validate the choice of motors, propellers and ESCs when it comes to thrust provided and to obtain other data such as consumed power or torque developed, which were necessary to further develop the computational model of the aircraft, static thrust test were conducted. The front rotors were tested on a *TytoRobotics Series 1580* test stand using the respective software, *RCBenchmark* [66]. The rear rotor (in direct drive and with the entire tilt mechanism assembly in place) was tested on the larger static thrust test stand that was available at CfAR and which was designed for larger rotor configurations. A custom LabVIEW [67] program was used to control the apparatus.

The tests were performed with all the rotors in a pusher configuration in order to mitigate the interference of the test stand's support with the registered performance and also as a safety measure for the case of the propeller's retaining bolts becoming loose during the test (Figure 4.6). Two wooden boards were also placed laterally to the setups to prevent lateral projection of debris in the case of propeller failure and the area where the test took place was interdicted to anyone except the person in charge of the tests. The control of the thrust benches was done through a computer which registered live data from the stations and where the user could also, at any time, stop the test. The setup where the rear rotor was tested was also fitted with an emergency button, which when activated would cut the power supply to the ESC and thus to the motor, providing redundancy to the safety cutoff system. Additionally, emergency cutoff parameters such as the acceptable range of input voltage and current were introduced on the programs which controlled the test benches. Finally, protective eyewear was used at all times when performing the tests.

During these tests, the measurement of the motor's angular speed was not available in the larger test stand due to technical limitations, in a way that the relations that shall be analysed will be between

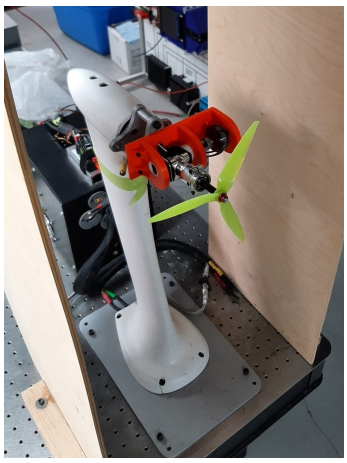

(a) Rear mechanism test setup.

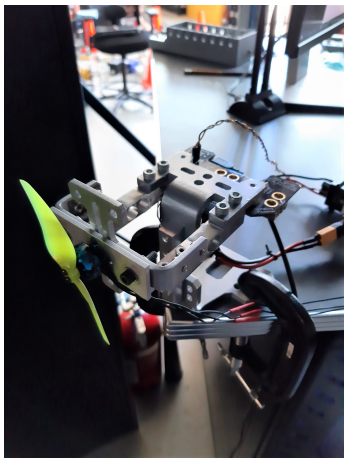

(b) Front rotors test setup.

Figure 4.6: Thrust test setup for both types of rotors.

the supplied PWM signal (throttle) and the output thrust and torque measured instead of the traditional thrust and torque constants used to relate such dimensions with angular speed.

Before collecting the actual data that shall be presented, a practice run was performed, where the settling times of the rotors' thrust were evaluated in order to determine how the tests should be conducted. From the observations made, it was decided that the throttle value would be increased by 10% at a time, followed by at least $5s$ of constant throttle, followed by another 10% increase. Afterwards, several tests were performed in order to obtain various data points for each throttle value and to minimize error in the derived motor models. In between each two tests the motors were disconnected from the battery and left to rest as to let them cool down and ensure that the sequential tests were performed under conditions as similar as possible among them. The load cells of the stands were also periodically tared. A battery with similar discharge rate and number of cells but with a higher capacity ($10000mAh$) than the ones chosen to be used in flight was also used as to ensure that the voltage drop was as limited as possible during said tests.

Front Rotors

The thrust tests performed for the *XING 1404 3000kV* motors with *Gemfan 4024* propellers and *T-Motor Air 20A* ESCs yielded the results represented in Figure 4.7, with some of the most relevant findings being highlighted in Table 4.5. The results of both motors were consistently similar.

Table 4.5: Static thrust tests results for the front rotors.

Maximum thrust claimed by manufacturer	**Maximum thrust experimentally measured**	**Relative difference**	**Thrust margin**
553 g	331 g	67.1%	66.8 %

Some interesting notes taken from such results are the approximately linear behaviour of thrust vs throttle for the tested propulsive system and the maximum thrust value that was registered - $331g$ - which fell short of the value provided by the manufacturer of $553g$. Nevertheless, this configuration will fulfill the

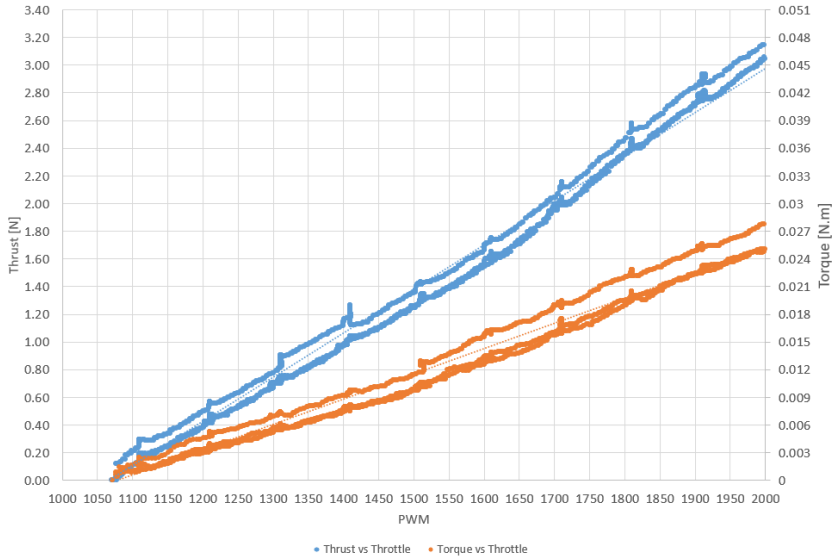

Figure 4.7: Thrust and torque curves against PWM signal provided.

intended purpose with the maximum thrust developed being far superior to the minimal required value.

Rear Rotor - Mechanical Efficiency

The introduction of additional mechanical elements between the mechanical power source, in our case the electric motor of the rear rotor and the final output shaft, where the propeller is mounted, will be translated into inevitable losses during the operation of the mechanism. Energy will be lost due to friction mostly, not only between the teeth of the gears (causing temperature increases, investigated in 4.5.1) but also in elements such as the additional ball bearings that needed to be introduced to ensure the proper alignment of the input and output shafts. Adequate maintenance of these elements can help minimize losses, mainly by making sure that all of the gears and bearings are properly clean and lubricated to make their operation as smooth as possible. Nevertheless, and as in any real-world system which is bound by the second law of thermodynamics, losses will occur during this system's operation.

In order to quantify the additional power that is required, by the rear rotor system, to produce the same value of thrust that the conventional arrangement of an equal propeller mounted directly on the same electric motor would generate, two sets of tests were performed.

First, before the rear tilting mechanism was assembled, a preliminary evaluation of the performance of the motor, propeller and ESC was done. Then, the system was assembled and further thrust tests performed. For that, the gearbox was fixed, using two wedges, in a horizontal position. Then, the assembly was mounted on the thrust test stand, with the output axis being perpendicular to the support, as it should. The results obtained from such tests can be seen in Figure 4.8, where the $Power\,vs\,Thrust$ curves for both configurations are displayed alongside the efficiency loss throughout the range.

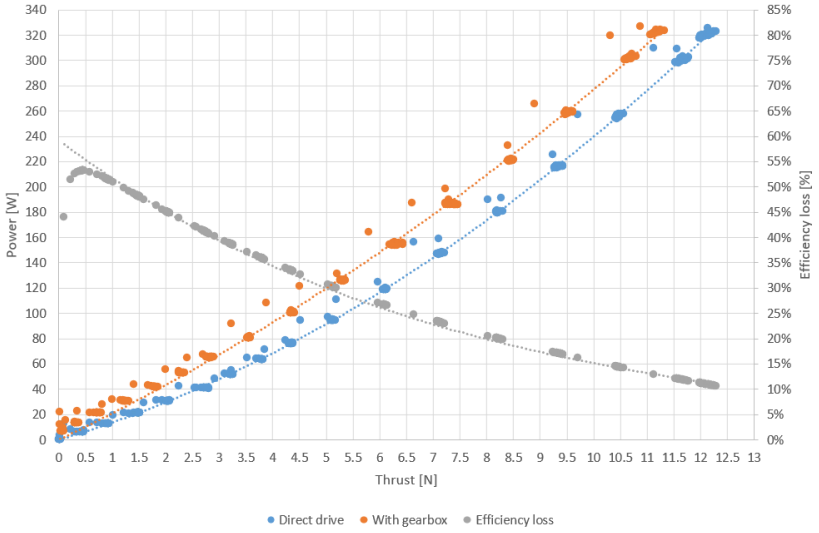

Figure 4.8: Power vs thrust curves for direct drive and for the entire rear tilting mechanism and loss of efficiency curve.

As before, some relevant data arising from these tests is presented in Table 4.6.

Table 4.6: Static thrust test results for the rear rotor.

Maximum thrust (Direct drive)	Maximum thrust (Tilt mechanism)	Power for hover (Direct drive)	Power for hover (Tilt mechanism)	Loss of efficiency in hover	Thrust Margin
1251 g	1147 g	193.60 W	230.32 W	18.96 %	23.3 %

From the results provided above it is clear to see that more power is drawn from the battery to achieve a similar thrust figure in the case of the tilting mechanism when comparing with the case where thrust is generated by mounting the propeller directly on the electric motor. Furthermore, it is verified that the efficiency loss, i.e., the percentage of energy that is lost due to the introduction of the gearbox and remaining additional components, is reduced with the increasing generated thrust. This is due to the fact that, associated to a higher thrust value being generated, a higher drag torque figure is also verified, hence placing a higher load on the gearbox. The curve obtained is consistent with the literature [28–30], where increases on gearboxes efficiency with power/loading have been previously verified.

Temperature Survey Tests

One of the concerns that arose during the design of the rear tilting mechanism was that the electric motor would overheat due to a lack of air circulation around it as this kind of motors are designed to have a propeller directly mounted on their axis, benefiting from some cooling due to being in the wake of such propeller. Thus, it was considered that a temperature survey should be performed as to ensure that the motor's performance loss due to magnet demagnetization was minimized [68, 69].

It was defined that the motor should be exposed to conditions similar to the ones it would find in a test-flight, with a constant monitoring of the temperature of the internal coils being performed, as well as of the thrust provided by the motor and of the electrical power consumed. The setup used for the tests

depicted in 4.5.1 was maintained and the static thrust tests performed with constant values of throttle being requested. These values were chosen based on the data obtained in the previous tests, in order to simulate hovering conditions.

The tests were performed with a requested throttle value of 80% and continuous operation times of $30\,s$, $60\,s$ and $120\,s$. The ambient temperature was $10°C$ and the temperatures registered at the end of such tests for both the motor and the gearbox's gears are shown in Table 4.7.

Table 4.7: Final temperature of motor and gears for different continuous thrust tests.

Time [s]	***30***	***60***	***120***
Final motor temperature [$°C$]	58	70	78
Final gear temperature [$°C$]	26	29	28

It was found that a considerable drop of the thrust provided by the rotor happened in the initial $35\,s$ of functioning, from an initial value of around $9.75\,N$ to a final value in the vicinity of $9.2\,N$. After this time, the output thrust tended to stabilize around this final value. As for temperature, the tendency was similar, with the temperature increasing considerably in the first stages of the continuous tests but with a tendency to stabilize from a time of around $45\,s$ onwards.

The gearbox gears' temperature was also monitored at the end of each test as to attest if a continuous loading such as the one provided would provoke a temperature increase that could jeopardize the gearbox well functioning. The main aspect of concern was the surface temperature of the miter gears, which has been proven to have a direct relation to the wear [70]. It was found that during the performed tests the plastic gears tended to increase their temperature quite rapidly but also achieved stability within the first 20 seconds, with the final temperatures reached posing no threat to the integrity of the components. The measured values for the gears' surface temperature at the end of the three tests is available in Table 4.7.

4.5.2 Actuator Mapping

In order to better replicate the dynamics of the real system on the computational model that was developed, as well as to facilitate the interpretation of the information retrieved in the flight logs, a mapping of both tilt mechanisms was performed where the tilting angle was measured against the PWM signal sent. For this, a digital angle gauge and a PWM signal generator were used and 4 sweeps of the range performed (two increasing the PWM values and two decreasing them). The results obtained for the front and rear tilting mechanisms can be found in Figure 4.9. Note that the rear tilting mechanism is not able to tilt by $90°$. This is due to a trade-off made to enhance the resolution of the angle adjustment near the vertical position in detriment of having the ability to tilt the propeller shaft to a fully horizontal position, which would bring no benefits to this test vehicle's operation anyway.

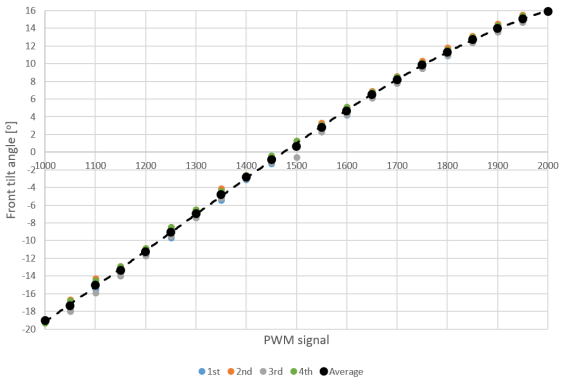

(a) Front tilt mechanism.

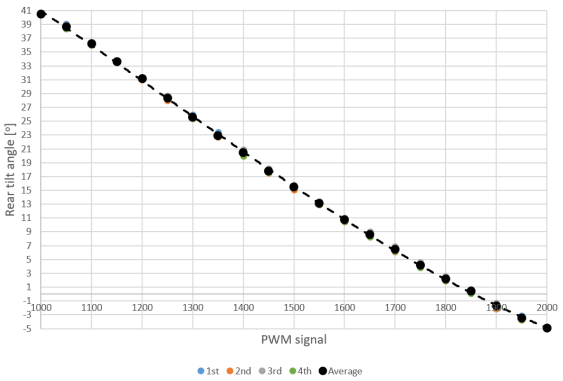

(b) Mapping of the rear tilt mechanism.

Figure 4.9: Mapping of both tilt mechanisms.

4.6 Mass Breakdown and Distribution

A detailed description of the mass of the various sub-assemblies and additional components present on the final test aircraft, the location of their individual CG and overall contribution to the total MTOM is provided in Table 4.8. The final location of the aircraft's CG is provided as well. The coordinate system used has its origin on the most aft location of the airframe and on top of its longitudinal axis.

Table 4.8: Mass breakdown and distribution on the vehicle built.

Assembly / Component	Mass [g]	X coordinate [mm]	Y coordinate [mm]	%
Airframe	130	170	0	11.13
Rear tilt mechanism	282	26	6	24.15
Rear motor and propeller	57	26	75	4.92
Front tilt mechanism	180	345	0	15.42
Front motors and propellers	24	493	0	2.06
Rear ESC	62	55	-35	5.31
Front ESCs	64	125	38	5.48
Battery	185	268	-35	15.84
PDB	36	180	30	3.08
Pixhawk 4	16	167	0	1.35
Receiver	6	55	-90	0.55
Others	125	170	0	10.71
Center of gravity	1168	167	0	

From said results (4.8), one can have an idea of the percentage of the vehicle's mass that is due to the existence of the tilting mechanisms. In total, and without considering the weight of the motors and propellers, these mechanisms account for 39.57% of the aircraft's MTOM.

The front tilt mechanism, fundamental for the proper functioning of the conceptualized test vehicle, yields relatively small room for weight optimization as it presents an already minimalist design with few parts. The main objects of change may be the 3D printed support, which can be reduced in size and thus weight, the PTFE bushings, which could be further machined, getting rid of some surplus material and thus weight, and finally the aluminium collars, which can be eliminated if the longitudinal loads are deemed negligible. A rough estimation yields that these changes might account for a weight saving of

around 45 grams (3.85% of the current MTOM value or 25% of this subsystem's mass).

In a future up-scaling of this front tilt mechanism for the Mini-E aircraft, it is expected that its contribution in relative terms to the overall MTOM will be reduced. This is justified by the fact that components such as the servos and even the support are likely to be oversized for the current vehicle and do not need to be increased proportionally to the scale increase between vehicles. In the case of the servos for example, these are already the same model that is utilized in the current iteration of the Mini-E for actuating the different control surfaces. As so, it is likely that the front tilting mechanism of the future tri-rotor iteration may utilize this very same actuator. The remaining parts, namely the arms, bushings and frontal motor supports, are likely to grow with the up-scaling (as will the front motors and propellers, for obvious reasons). Nevertheless, the overall relative mass of the entire subsystem in relation to the Mini-E's MTOM is expected to be reduced when compared to the contribution of the present iteration of the front tilt mechanism to the current test vehicle's mass.

When it comes to the rear mechanism, which accounts for 24.15% of the total weight of the test aircraft, the main contributor for the total mass balance is the 90° gearbox (including propeller shaft), with a mass of $134\,g$ (47% of the mechanism's mass), followed by the gearbox support ($70\,g$ or 24%). Despite not being the main contributor, this last component may be the one more susceptible to modification in an effort to reduce the current system's mass, as the employed gearbox already presents a fairly minimalist design, with little room for optimization.

In a future up-scaling effort, it is expected once again that the relative contribution of such subsystem to the overall MTOM will be reduced. The main reason behind this statement is that the utilized gearbox (which accounts for almost half of the mechanism's overall weight) is thought to be oversized for the current application and may be used in the future aircraft, in a way that the component may be maintained but the overall MTOM increased. This statement, although requiring further testing to be confirmed (see 7.3), is based on the fact that the gearbox's expected peak efficiency was higher than the one effectively obtained during static thrust tests (4.8), which leads to the belief that it will support larger continuous loads than the ones presented during the current vehicle's operation.

Chapter 5

Flight Testing

In the present chapter, the results obtained during the several flight tests which were performed, as well as the modifications implemented in between each set of tests will be addressed. Some of the attitude tendencies found during such flights will also be explored and compared with the results obtained in the parametric studies which were performed for the test vehicle and which are available in subsection 3.2.2.

This chapter will be divided in two sections. The first (5.1) will address the results found in the initial test flights, used to tune the autopilot and which led to the proof of concept of this novel aircraft configuration in hovering conditions. The results obtained during the forward flight test will also be presented here.

Later in this chapter (5.2), an analysis of the flights performed with the goal of gathering data for system identification will be done.

5.1 Proof of Concept

The first and main objective of this work is the proof of concept of the presented novel tilt tri-rotor configuration. As so, it was crucial that the test vehicle could accomplish, firstly, a stable, hovering flight.

To achieve this goal, and as referred earlier, a custom airframe was developed in PX4 environment to obtain an appropriate flight controller. As so, given the experimental character of this controller/configuration, preliminary testing under controlled conditions was required as to allow for the tuning of the autopilot without endangering any personnel, property or the aircraft itself.

The first experimental flights were performed at an empty hangar near CfAR. Only essential personnel was allowed during the experiments, namely the pilot, an individual responsible for media collecting and one responsible for the aircraft handling. These individuals were required to use protective eyewear at all times and a fire extinguisher was present. Furthermore, during the first round of tests the aircraft was tethered to four $5\,kg$ weights, preventing it from exiting the defined flight perimeter.

The autopilot was programmed to only arm upon request of the pilot and to disarm automatically in case a loss of connection with the transmitter spanning for over $1s$ was verified.

5.1.1 Hovering Flight and Autopilot Tuning

This test stage involved four sequential flights, with tuning of the autopilot and of the aircraft's configuration happening in between them. The initial MTOM was $1260\,g$, 14.5% over the initial estimation.

First Indoor Flight (Tethered)

This test was then performed with the aircraft tethered with enough slack for it to be able to hover at around $50\,cm$ from the ground before being disturbed by the tethers.

During this test the aircraft armed successfully and managed to hover at a height of about $5\,cm$, being able to correct its attitude when disturbances were introduced, mainly from tether tensioning. Nonetheless, the performance was not ideal, with the aircraft revealing a tendency to pitch up (which could be managed by the pilot but introducing unnecessary workload until the correct trim value was placed on the RC transmitter). Furthermore, the flight time and altitude achieved were quite limited since the rear rotor struggled to balance the weight assigned to it (80%). This was partly due to the MTOW of the aircraft being higher than initially estimated but also to the fact that the set of batteries used were not new, meaning that the discharge rate was not constant throughout the flight, diminishing as it progressed and the battery voltage dropped. Nevertheless, these batteries were used throughout the entirety of the tests since it was the only model in sufficient number to perform all of the future required outdoor flight tests without significantly changing the aircraft's mass and performance and without the need to charge batteries in between tests.

After careful analysis of the results obtained during this test, it was decided that:

1. The test aircraft should undergo a revision in order to reduce its total mass;
2. The autopilot should be tuned, aiming to reduce the aircraft's tendency to pitch up;
3. A weight distribution of $30/70$ would be tested instead of the current $20/80$. This final decision was done for three main reasons: the first was that the rear rotor's performance was worst than expected from previous testing; secondly, it was defined that this weight distribution would still allow to prove the concept and the viability of the autopilot, in a way that with small alterations of the code it could still be used in an aircraft with a $20/80$ weight distribution. Furthermore, the general tendencies of the aircraft behaviour would still be comparable to the results obtained in the trim studies previously conducted.

The main focus of the weight optimization effort was the electric power distribution system, which was completely revised. This revision, alongside other small changes, translated into an overall reduction of $92g$ or 7.3% of the initial mass.

As for the autopilot tuning, the biggest change introduced was the tuning of the configuration geometry, as the CG location was moved, and of the constant which relates the thrust provided by the rear rotor relative to the one provided by the front rotors by introducing an average value which could relate the thrust relation across the entire throttle range (through linearization of the curves) instead of the one at 100% throttle as previously done.

Second Indoor Flight (Tethered)

The second indoor flight revealed that the changes had a positive effect upon the aircraft behaviour, which was now able to hover at around $70\,cm$, with the pilot reporting a much more manageable tendency to pitch up (requiring only slight adjustment of the trim value on the RC transmitter) and a slight, but expected tendency of the aircraft to drift to the right (3.2.2), which then required a slight left roll trim value to be introduced.

Further changes in the geometry file regarding the above mentioned thrust constant were performed once again in order to assure that this constant described as faithfully as possible the relation between the thrust generated by the rear rotor relative to the front ones in the range of throttle used in previous flights (instead of across the entire throttle range as before).

Third Indoor Flight (Tethered)

In the third flight the aircraft's behaviour was further enhanced, with only minimal trim adjustments being required. This meant that the pilot had enough time to adjust the trim values in mid flight, unlike previous flights where adjustments had to be made with the aircraft on the ground to limit the workload of the pilot.

The encouraging results achieved during this test lead to the team decision of flying without the tethers as these were now acting more as disturbances on the aircraft's hovering flight (which the controller could handle, even though the disturbances introduced were fairly violent) than as a protection system.

Fourth Indoor Flight (Untethered)

During this first, free, indoor flight (Figure 5.1) the trims defined in the previous test were used (minimal pitch down and left roll trim) and the aircraft was capable of hovering stably, with the pilot reporting that the vehicle was easy to control and keep in place[1]. During this test, the pilot performed some manoeuvres along the pitch, roll and yaw axis of the aircraft with the vehicle showing predictable and stable dynamics.

This final test also allowed to validate some of the results obtained from the trim studies previously conducted, namely for zero-wind conditions. During steady hovering flight, the aircraft assumed a roll angle in the close vicinity of $-0.7°$, value predicted in the simulation for a $20/80$ mass distribution. Meanwhile, despite what was expected, the pitching angle was not null, assuming a value of around $-1.3°$. This discrepancy was later diagnosed as an effect of a modification introduced to the airframe, namely of the landing gear, in order to accommodate the fitment of two carbon skids, which introduced a $1.3°$ inclination in the whole airframe when sitting on a leveled surface. This meant that when the PixHawk's accelerometers were calibrated, a $1.3°$ bias was inadvertently introduced. This was later taken into account for the outdoor flight tests when performing the calibrations. As for the tilting angle of the front rotors, it was found that, according to the mapping performed for this system, the vehicle assumed a hover tilting angle close to $3.3°$ while the expected value was $5°$. This discrepancy may

[1] The autopilot only managed the aircraft's attitude since position control was not available, as no GPS sensor was used.

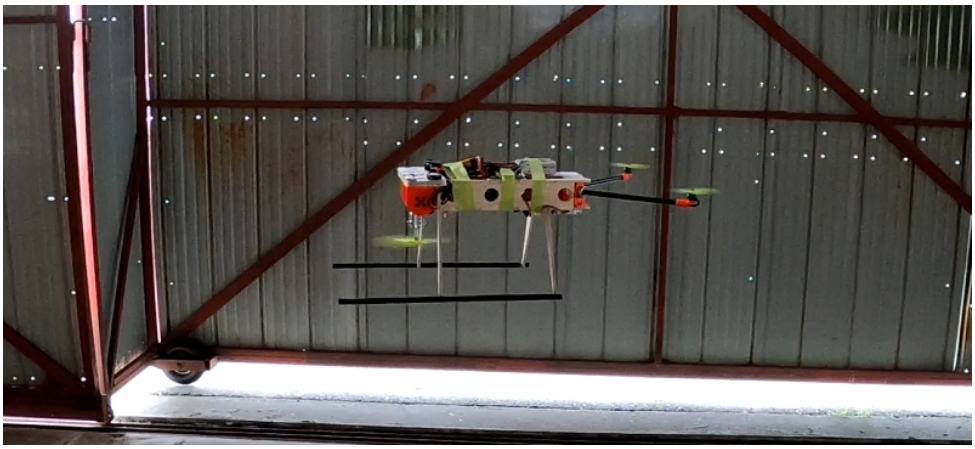

Figure 5.1: Indoor flight without tethers.

be associated to possible errors in the estimation of the rotors' drag torques and to the slightly smaller loading of the rear rotor and larger of the frontal ones in relation to the initial simulations, yielding a smaller torque imbalance along the yaw axis. Nevertheless, these results were quite coherent with the findings of the previous studies, thus helping to validate the work previously done.

With this test, the viability of the proposed concept was also proved, thus allowing to proceed to outdoor flight testing as to assess the airworthiness of the designed vehicle in real-world, outdoor conditions.

5.1.2 Forward Flight

After the indoor tests proved the viability of the proposed concept for a VTOL tri-rotor with frontal rotors tilt aircraft to achieve stable hovering flight, recover from external disturbances and perform small manoeuvres in all of the three axis, it was still needed to prove that such aircraft was able to achieve stable forward and leveled flight when the rear rotor was tilted. This test would thus evaluate if the proposed concept could be applied to a fixed wing aircraft which should transition from vertical to horizontal flight by means of tilting the output shaft and propeller from a vertical position all the way to a horizontal position in horizontal flight. The test vehicle, however, was designed to prove solely the multi-rotor concept. As so, the PixHawk ® and the transmitter were programmed to tilt the rear rotor by 5°, in order to allow for it to provide enough vertical thrust to sustain the vehicle in leveled flight while developing an horizontal contribution that allowed to gain horizontal momentum.

To perform these outdoor tests, the aircraft was registered with *Transport Canada*, an appropriate location was chosen (Class G airspace), and all of the requirements enlisted in the University of Victoria's Center for Aerospace Research Standard Operation Procedure for flight testing met. The flight test team was composed of a certified Pilot, a Visual Observer, a Range Safety Officer and an individual responsible for media collection and aircraft handling. Safety and operational checklists were developed and followed, as well as custom test cards, where the required manoeuvres for all of the tests were described. The flight testing area was defined using traffic cones and access limited to essential personnel. The flights were performed only after the nearby terrain and airspace were deemed clear and

any possible dangers ruled out.

With all of the safety measures in place, the vehicle was armed, the take-off manoeuvre performed and the aircraft positioned. After a few second of hovering, the pilot introduced a rear tilt angle of $5°$ and the aircraft started gaining forward speed (Fig. 5.3). During forward flight the aircraft revealed a considerably stable attitude with minimal to no need for the pilot to introduce corrections during such period (as noticeable in Figure 5.2, where *Aux1* defines the rear tilt mechanism action and *Y/Roll*, *X/Pitch*, *Yaw* and *Throttle [0, 1]* refer to manual inputs provided to the respective axis/values). After $6s$ the pilot switched the rear tilting angle back to $0°$. With the obtained results it was considered that the ability of such conceptual aircraft to perform stable forward flight while in multi-rotor configuration was fully proven.

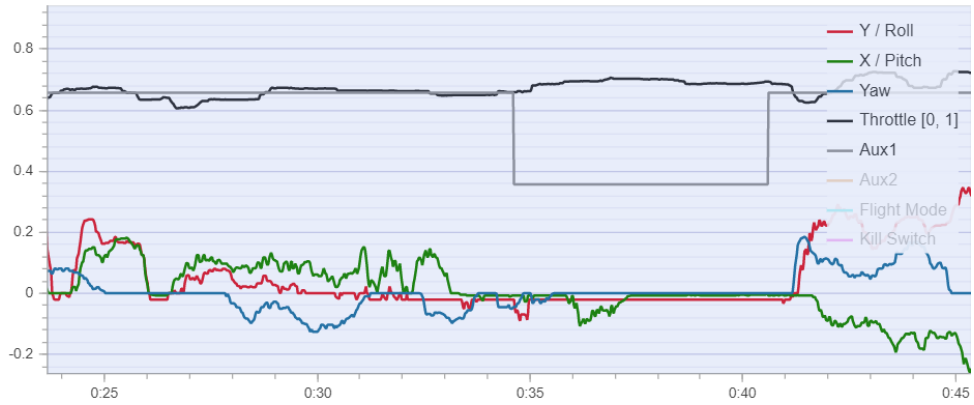

Figure 5.2: Manual control inputs from the pilot during the moments that preceded and during the forward flight stage.

Figure 5.3: First outdoor forward flight.

5.2 System Identification Flights

In order to gather data for system identification, test flights where specific manoeuvres, meant to evaluate the dynamics of the tri-rotor along the different attitude axis, were performed. It was defined that these tests would consist of five flights. In the first preliminary flight the pilot would practice some of the manoeuvres that would be requested in the following flights and try to expand the flight envelope of the aircraft (which until this point had only performed hovering flight and small indoor manoeuvres).

In the next three flights, several sets of *chirps* (high frequency oscillation manoeuvre) and *doublets* (2.3) were performed, as to evaluate what the aircraft response would be to such inputs. These three sequential flights were then dedicated to the roll, pitch and yaw axis, respectively. The fifth test was performed as a validation flight where *chirps* and *doublets* exciting the three axis of the aircraft (one at a time) were performed, as to evaluate the performance of the dynamic models arising from system identification.

These flights were performed with the trim settings defined in the final indoor flight, in a way that there was a small pitch down and left roll trim in place.

During the first system identification flight (roll axis), the aircraft revealed an unexpected tendency to roll further to the left than to the right. Although the initial cause of such behaviour had been attributed to the fact that the aircraft had some left roll trim introduced, it was later found that it was mostly due to an unconscious bias introduced by the manual input of the pilot, which was minimized in later manoeuvres.

For the case of the yaw axis flight, it was firstly found that during the initial high frequency part of the chirp manoeuvres the aircraft revealed limited response even though the log file showed that the front tilting mechanism was actuating according to the manual input provided. Such behaviour can be due to the existing delay in the servos' actuation which for high frequency manoeuvres such as these may be translated in the oscillations being severely reduced, as the actuator does not have the time to rotate at the same rate as the PWM signal's information is provided. With the diminishing frequency of the input the aircraft started oscillating in yaw, as supposed, with a slight tendency of yawing to the right. This was primarily due to a small bias registered in the manual control inputs.

It is also interesting to note that the front tilting mechanism will oscillate around a trim point instead of around the neutral position of the servos (front motors in a fully upward position). This means that the requested oscillations in the PWM signal sent to the servos caused by the *chirp* or *doublet* inputs will be registered around the value of 1550 (inclination required to hover steadily) instead of 1500 (as shown in Figure 5.4, where *Output 3* stands for the front tilting mechanism servos' input signal during two chirp manoeuvres), thus meaning that while the aircraft is chirping the front rotors will spend a larger amount of time tilting towards the right than to the left. This however is not the cause for the previously mentioned tendency as the oscillations, if perfectly symmetrical, would occur around the trim point.

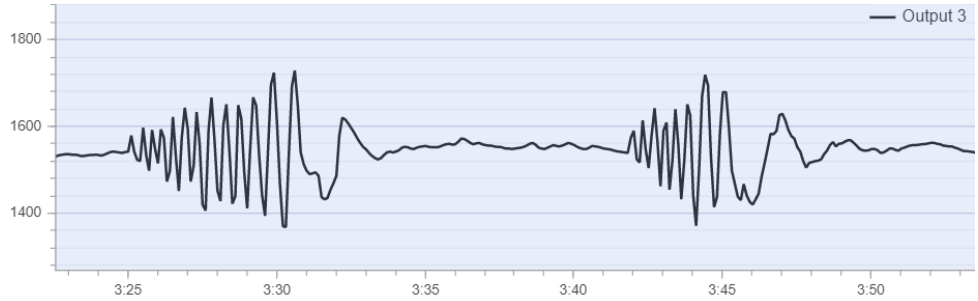

Figure 5.4: Front servos PWM signal over two chirp manoeuvres.

When it came to the pitch axis test flight, the vehicle showed an initial tendency of drifting backwards during the chirp manoeuvres. This drifting movement was slow and easily manageable by the pilot

after the manoeuvre was complete (as were all of the drifting movements registered during the other, previously described, test flights), with a posterior analysis of the log file of this flight revealing that this drift was not due to the aircraft itself but rather to an unconscious bias of the manual input provided by the pilot, who had the tendency of requesting a bigger amplitude in pitch up than down during the chirps. Furthermore, and as expected due to the inherent configuration of the RC transmitter, some slight perturbations in the roll axis were also introduced during these high frequency pitch manoeuvres, given that the same stick is used to control the pitch and roll axis. This perturbation revealed itself during the flight as a slight drifting movement to the left (due to negative roll input) during some of the chirp manoeuvres. When it came to the doublets performed along this axis the results were satisfactory, with only a slight tendency of backward drift being noticed during one of the manoeuvres, which was due once again to an unconscious bias introduced through the manual controller.

Finally, a validation flight was done, where several sets of chirps and doublets were performed for each of the axis (one at a time) with the objective of performing the validation of the models obtained through system identification and which shall be explored later.

Overall, these real world tests served the ultimate purpose of proving the airworthiness of the novel tri-rotor concept presented in this work, not only in fully multicopter mode but also with the introduction of a rear rotor tilting angle, paving the way for a future, deeper investigation of the transition conditions between vertical and horizontal flight phases. Additionally, these tests provided useful data which allowed not only to further validate the parametric studies previously pursued in 3.2 but also to perform the upcoming studies on system identification of the developed test vehicle.

Chapter 6

System Identification

System Identification techniques can present numerous advantages when applied to aircraft design and development due to the robustness of results provided and to the possible reduced time needed to acquire them. Such methodology provides engineers with the ability to save precious development time in specific steps of the aircraft design process, such as autopilot development and tuning, while also endowing them with the ability to make considerable changes to the actual aircraft without the need to revise the entire preliminary flight dynamics model. This ability is particularly interesting when applied to aircraft with varying payload or configuration, or in an early stage of flight testing where the vehicle's design can suffer several modifications which can change its dynamics. By applying SID techniques to obtain new dynamic models, it becomes just a matter of doing a rather quick battery of test flights with the aircraft's most recent configuration (as long as this design maintains the previous airworthiness of the vehicle), perform an array of pre-defined manoeuvres and then run the collected data through a system identification algorithm which provides the team with a FDM of the most recent aircraft configuration. This FDM can then be used, for example, to perform autopilot tuning or to update the computational model of a flight simulator for future pilot training.

Due to the quick turnaround time made possible by the application of this technique, it becomes indicated for use in projects with a rather restrictive time-frame (2.3), such as the one presented in this thesis, where the full development of a novel configuration aircraft, from the conceptual design phase to flight testing is done.

As so, two distinct system identification approaches will be explored with two different goals:

1. *Time based approach* - the first method will be based on the pre-existent flight dynamics model and will have the goal of providing more robust estimations of certain design parameters that were previously arbitrated. In order to do so an optimization algorithm will be employed alongside the existent Simulink® FDM.

2. *Transfer-function approach* - the second method will serve as an alternative to the existent FDM and as a means of comparing two distinct techniques. This will use data from flight testing to estimate a set of transfer functions which can describe the dynamics of the vehicle without the need to have previous insight into the aircraft's physical characteristics.

6.1 Time Based Approach

Throughout the development process of the test vehicle, it was possible to continuously revisit and update the flight dynamics model initially presented in Chapter 3. This was done by replacing the initial mass and inertia estimations by more mature values and introducing more developed actuator models, where the delays were accounted for, as well as the mapping obtained for the developed tilting mechanisms and the rotor performance curves obtained during the static thrust tests.

In order to perform system identification, the model was fed with real flight control inputs and a cost function block was added to the existent computational model of the aircraft. This block compared the attitude and rates of the simulated aircraft to the ones obtained in the analogous time frame of the real flight, providing a cost value which could then be imported to Matlab at the end of each simulation.

Having a cost function defined, it was thus possible to implement an optimization algorithm. To do so, the variables of interest were defined, as well as the allowable ranges of variation and initialization point for each one. In total, 42 variables were studied, addressing the inertial characterization of the aircraft's body (6 variables), the thrust and torque curves associated to each rotor (14 variables), rotor positioning (9 variables), front tilt mechanism actuation (1 variable), the possible misalignment of the flight controller relative to the airframe (3 variables) and errors/biases in the orientation of the rotors (9 variables). The goal was to provide the model with the best possible chance of replicating the real world flight while starting with the pre-existent FDM. The allowable lower and upper boundaries for each variable were defined based on the assumptions previously made throughout the development of the FDM and on the data collected during the ground testing phase of the aircraft's development.

The study methodology consisted of starting the simulation with relatively small timeframes ($0.5s$) and progressively enhance the range. Different start points of the flight tests' data were considered as to provide flexibility to the model. Manual iterations in between optimizations were also done as to perform sensitivity analysis into the influence of changing certain values on the global behaviour of the model.

Initially, the optimization was performed using the Matlab® function *fmincon* and the *interior-point* algorithm. Iterations were also performed using *sqp* without noticeable improvements. The *fminsearch* function was also used with both algorithms as to try to find feasible solutions of this unconstrained problem. However, this later procedure proved, unlike what was expected, less prone to conveniently explore the assigned design space than the initial setup, with a strong tendency to provide solutions in the close vicinity of the initial point that was supplied.

It was then found that, when expanding the optimization time frame from the initial $0.5s$ intervals, the algorithm had a tendency to find feasible design points where the cost function was minimized but that did not offer a close follow-up of the intended behaviour. Furthermore, when exploring time intervals which spanned over more than $2s$, the simulation revealed a strong tendency to diverge. This behaviour, although unwanted, was not entirely unexpected when considering the natural bare-airframe instability that is a characteristic of most rotorcraft configurations.

This tendency is in fact mentioned in the literature, with most authors referencing the work of Mark B. Tischler, developer of the CIFER® software (Comprehensive Identification from Frequency Responses)

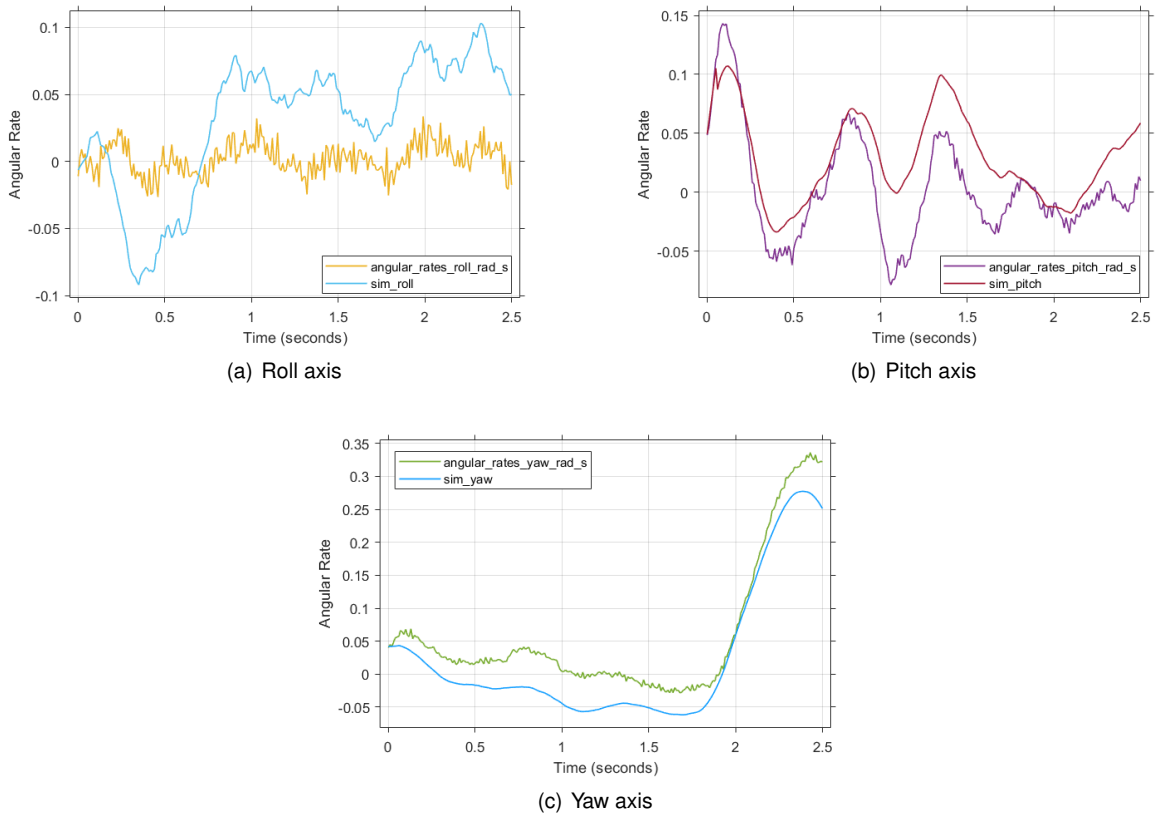

(a) Roll axis

(b) Pitch axis

(c) Yaw axis

Figure 6.1: Comparison between simulated and real dynamics for the same control inputs.

which is taken as the industry standard for full scale rotorcraft SID (already applied successfully to smaller scale UAVs [71]) and author of one of the main reference books in the area, "*Aircraft and rotorcraft system identification*" [39]. In this document, Tischler explores the difficulties associated to conducting system identification of physical systems with highly coupled dynamics (such as the proposed tri-rotor) using time-domain algorithms due to the complexity of the problem, which includes, apart from the control derivatives of interest, bias and reference-shift terms that make the task of the algorithm even more difficult due to their correlation to the parameters of interest. In the same document, this author refers that as the order of the investigated system is increased, time-domain algorithms are particularly affected by the need to identify those extra parameters, increasing the required processing time and reducing the accuracy of the obtained results. In parallel, frequency-based system identification techniques have proven to yield much more satisfactory results in the field of rotorcraft SID, being now more widely used. As so, the logical next step of this work was to employ a frequency-response approach to the collected data in order to obtain a dynamic model of the developed aircraft.

6.2 Transfer-Function Approach

The followed, transfer-function based, system identification strategy can be classified as a parametric approach, since the goal is to identify a restrict number of quantities, under the shape of numerator and denominator coefficients (a_i and b_i as shown in equation 6.1), that allow to achieve the best fit between

the frequency-responses of the obtained model and the data acquired in validation flights. Even though classified as a parametric model, the obtained parameters *per se* do not represent physical quantities as in the previous method, where the goal was to get estimations for different design parameters of the aircraft.

$$T(s) = \frac{a_0 s^n + a_1 s^{n-1} + ... + a_n}{s^m + b_1 s^m + ... + b_m} \tag{6.1}$$

Moreover, the devised algorithm treats the dynamics of the aircraft as uncoupled, unlike the previous method where the coupled dynamics were reflected by the model. That way, the program will consider each attitude axis of the aircraft as a single-input-single-output (SISO) system where the output rate on each axis is solely dependent on the control input (rate setpoint) provided to it.

The algorithm works by providing it with the data obtained in the test flight where the target attitude axis was object of excitation. Furthermore, the data is split in several time intervals (see Figure 6.2) where a specific manoeuvre is performed (*chirps* and *doublets*) or where the aircraft was in hover. Then, the program will take said intervals and build several data sets with all the possible combinations between them in order to provide the model with as many ”training” cases as possible through the execution of a single test flight. After this step, the program estimates a transfer function for each case (using *tfest* [72]) and compares all of the obtained transfer functions for fitment against a separate validation flight data which was not used in the previous step, as to determine the one which offers the best representation of the aircraft's dynamics along the explored axis. As for the configuration of the transfer function, i.e., number of poles and zeros, a minimum and a maximum number of poles, as well as a minimum number of zeros is defined by the user. This way, the program will also test different transfer function configurations in the previously described step.

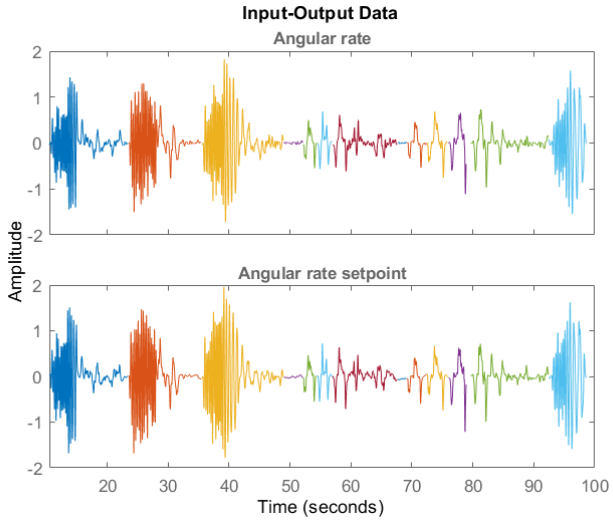

Figure 6.2: Example of flight data selection.

This process is then repeated for the remaining axis, with the program outputting three transfer functions and three graphical representations of the simulated dynamics that correspond to each transfer function against the real flight data as previously mentioned. Furthermore, the Normalized Root Mean Square value is also presented, as a measurement of the goodness of fitment for each axis. This is

done through the use of the *compare* Matlab® function [73]. The transfer functions obtained for each axis, as well as the respective goodness of fitment value are shown in Table 6.1.

Table 6.1: Frequency-response SID method results.

Axis	Transfer-function	Goodness of fitment [%]
Roll	$\frac{-12.09s^2+1077.51s-7.82}{s^3+50.52s^2+1065.96s+56.07}$	79.57
Pitch	$\frac{-0.22s^3+3.71s^2+92.86s+170.49}{s^3+18.39s^2+138.65s+291.62}$	67.62
Yaw	$\frac{3.74s^2+0.14s+0.93}{s^3+3.68s^2+0.25s+0.91}$	62.04

The graphical representation of the dynamic responses of the aforementioned transfer functions against the ones obtained from the real validation flight are presented in Figure 6.3.

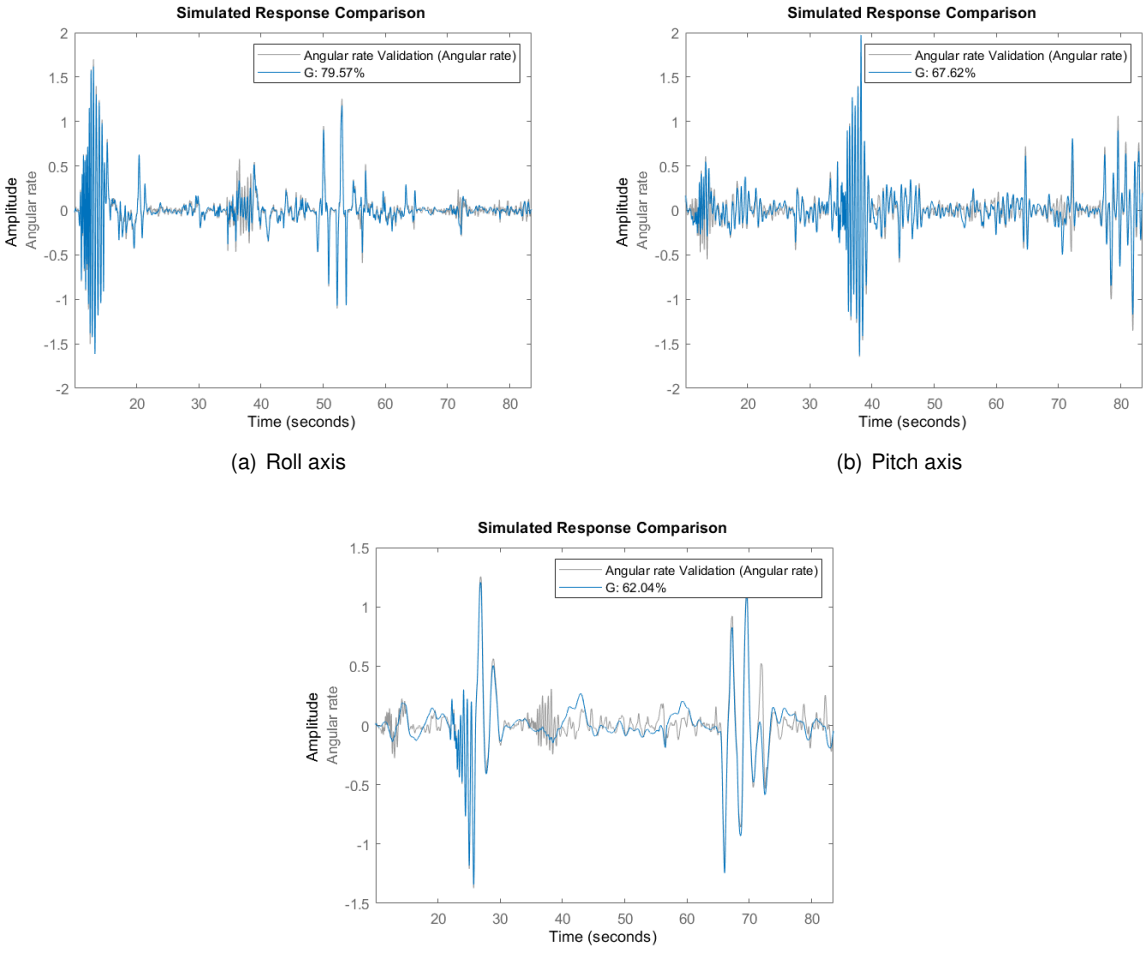

(a) Roll axis

(b) Pitch axis

(c) Yaw axis

Figure 6.3: Comparison between simulated and real dynamics for the same control inputs.

From these results it is interesting to note both the considerably high level of fitment that was achieved with the data of only one flight for each axis and also the neglecting of the coupled dynamics that is patent in some intervals. This tendency presents itself as the main cause for reducing the overall goodness of fitment values. The following analysis will benefit of the joint interpretation of both the figures presented in 6.3 and of the data provided on appendix C, where the inputs and outputs registered for each axis

during the validation flight are presented.

Drawing attention to the timeframe that encapsulates the *chirp* manoeuvre performed along the pitch axis ($\sim 35 - 40s$), it is clear that the method neglects the coupled dynamics of the vehicle. Considering the graph that is relative to the roll axis, an oscillation of similar frequency to the pitch *chirp* is in fact registered. However, this is due to a low amplitude roll setpoint oscillation that was verified simultaneously and that might have appeared due to the fact that the control stick that receives the pilot's inputs in roll is the same as for pitch. Nonetheless, in the actual flight, the magnitude of the roll oscillations during this period (displayed in grey) was higher than the replicated movement due to the existence of coupling dynamics between pitch and roll that are not considered by this technique.

Considering now the simulation of the aircraft's behaviour in yaw, it is clear that the lower fitment that is verified on the last graph is mostly due to the neglecting of the coupled dynamics. In the initial stages of the simulation, when the roll *chirp* is performed (not reflected on the yaw rate setpoint), the oscillations registered on the real flight are not replicated by the model. If one considers the time interval where the pitch *chirp* manoeuvre is conducted once more, it is noticeable that the yaw model neglects the oscillations that were in fact verified in yaw and that derived not only from the coupling of the pitch and yaw axis but of the roll and yaw axis as well. However, considering the configuration of the vehicle, is easy to understand that the coupling between both axis and the yaw axis should not be entirely neglected as both the control in roll and pitch presupposes action of the front rotors which, alongside the front tilting mechanism, also manage the yaw attitude of the vehicle. As so, when the rotational speed of the front rotors is altered to perform a manoeuvre in roll or pitch, and considering that these are inclined due to the action of the front tilt mechanism, this will derive in an inadvertent action along the yaw axis.

In the opposite sense, it is interesting to verify that actions upon the yaw axis have a considerably small influence upon the dynamics of the remaining axis. This is mostly due to the intentional decoupling of controls that was done when devising the autopilot for this aircraft, as already explored in section 3.3.

Additionally, in order to further understand the relatively low fitment value obtained for the yaw axis, the obtained transfer function was applied to the final indoor flight's data. This yielded a goodness of fitment of 70.54%, 8.5% above the studied case. This was mostly due to the fact that the manoeuvres performed in both pitch and yaw in this indoor flight had a smaller amplitude and frequency than the ones performed in the outdoor validation flight. This meant that the coupled dynamics were not as pronounced and that, therefore, the model could more faithfully replicate the behaviour of the vehicle.

The presented method reveals particular ease in the replication of well defined manoeuvres in all of the axis when these arise from an autopilot/pilot command and not from natural coupling of the axis' dynamics. This yields that the method may be particularly interesting when used to analyse aircraft systems which present more uncoupled dynamics. Nevertheless, and even though the presented vehicle shows a strong tendency for coupled motion, this frequency-response technique allowed to obtain a model which could effectively replicate the dynamics of the designed vehicle, even if uncoupled. Furthermore, the model presented flexibility, as it was capable of replicating more than one flight unlike the time based ones, which had a tendency to diverge even when only the initialization point within a specific flight was changed.

Chapter 7

Conclusions

In this chapter, an overview of the work done will be presented, highlighting the main conclusions and milestones reached, as well as a final balance of the achievements, discussing possible improvements on the concept and some of the work that may follow.

7.1 Summary

The main goal of this thesis work was to prove the airworthiness of a novel tri-rotor configuration for future application to the Mini-E aircraft for the realization of a fixed wing aircraft with Vertical Take-Off and Landing capabilities. However, there were several secondary objectives which had to be met in order to achieve this global result.

The first milestone of the project was the derivation of the equations which successfully described the dynamics of a vehicle with a tri-rotor configuration and $20/80$ thrust distribution, as to obtain an initial flight dynamics model. Having reached this point, it was then possible to develop, in Simulink® environment, an attitude controller for the Mini-E tri-rotor configuration in hovering conditions. The results obtained from the simulations that were carried out showed that the proposed configuration could not perform completely level hovering flight while maintaining position, as it showed a tendency of drifting to the right due to the thrust vectoring strategy required to maintain the yaw attitude. Therefore, the following step was to determine the attitude and actuation required for the simulated aircraft to achieve steady hovering flight.

The parametric studies which followed, and that provided these answers, were done through the use of an optimization process customly developed for the purpose. The use of such program allowed for the study of the required hovering conditions under several wind scenarios for both the Mini-E and test vehicle, allowing for an initial hovering flight envelope to be created based on the results and providing valuable insight into the limitations of the configuration under several flight conditions. This algorithm also allowed for the study of the relation between the rear rotor shaft tilting angle and the forward speed that the aircraft could achieve, paving the way for future transition condition studies to be performed for the Mini-E aircraft. Although the test vehicle did not have any lifting surfaces, a similar study was carried

out as to gain insight on the influence of the rear tilting angle on the capability of the aircraft to gain forward momentum while in leveled flight.

After the initial studies were concluded and with the preliminary sizing of the aircraft completed in parallel, it was possible to start designing both the airframe and the tilting mechanisms. Both the front and rear tilting mechanisms were designed, with several iterations and revisions in the process until a final concept was achieved. These were then built, their actuation mapped and the performance of all three rotors studied. An investigation on the loss of efficiency that is caused by the introduction of a gearbox between the output shaft of the rear motor and the tilting propeller shaft was also performed, in an effort to understand the phenomena and possible ways to minimize it.

Before flight testing could begin, and after all ground testing was completed, a custom autopilot was devised for this unprecedented configuration in PX4 environment and tested under controlled conditions.

Next, the flight testing phase began, where a series of tethered indoor flights were performed with the objective of tuning the aircraft, as to obtain an airworthy vehicle capable of performing stable hovering flight and manoeuvering in all axis. As a result, the vehicle was finally able to fly untethered, showing satisfactory maneuverability and stability. These initial tests also allowed to validate the findings of the trim parametric studies previously performed for zero wind conditions.

The next step was the commissioning of the vehicle and registration with Transport Canada to enable outdoor flight testing. In these tests, the vehicle proved capable of performing hovering flight in real world conditions and successfully executed several manoeuvres in all axis throughout the various flights aimed at collecting data for system identification. Finally, a forward flight test was conducted where a 5° tilting angle was commanded to the rear tilting mechanism, with the vehicle revealing stability while gaining horizontal speed as expected. Unfortunately, due to technical difficulties, it was not possible to fit the vehicle with a GPS sensor for this last flight in a way that no adequate speed data could be collected as to validate the values obtained in the parametric studies. However, it is considered that the aerodynamic model used in such studies, for the case of the test vehicle, might have underestimated the contribution of the drag, yielding that considerable speeds could be achieved with too small deflections. Nevertheless, from video footage, an average speed of $7m/s$ was estimated during the $6s$ that composed this test, with the vehicle revealing a tendency to continue gaining speed if not for reaching the limit of the defined test perimeter.

Finally, the last goal of this work was to perform system identification of the vehicle developed. For that, two techniques were used, with the first being a time-based method, usually applied to fixed wing aircraft, where the existent FDM was used in iterative simulations and its parameters adjusted in order to provide a more accurate fitment to the test flight data. However, due to the naturally unstable bare-airframe characteristics of the studied configuration, it was not possible to accomplish a flight simulation of more than $2s$ with satisfactory results. Nevertheless, the tendency of the program to change the initial parameters by small amounts allowed for concluding that the estimations made initially were not far from reality (as also proved by the indoor test flight results). In order to successfully perform system identification of this aircraft, a frequency-response method was used, as usually suggested in the reference literature for rotorcraft SID. Using this technique, a dynamic model was obtained, which provided a more

satisfactory representation of the aircraft dynamics.

7.2 Achievements

The main goal of this thesis work was to prove the airworthiness of a conceptual tri-rotor configuration. This goal was successfully met, since the test vehicle managed not only to achieve stable hovering flight in real world conditions but also perform various manoeuvres with varying frequencies in all axis. Moreover, the vehicle proved capable of performing stable forward flight as would be required in the transition phase of a VTOL fixed wing aircraft.

It is also considered that all of the project objectives initially set in section 1.4 were met, from the initial theoretical study of the expected behaviour of the configuration in hover to performing system identification of the final test aircraft.

7.3 Future Work

On the topic of system identification, it would prove of interest to assess the performance of an established tool such as CIFER® on the task of identifying a FDM for the novel rotorcraft configuration presented in this thesis. This algorithm allows for the identification of a state space model, which can capture the nonlinearities of the system and obtain values for the variables of interest while avoiding the time-consuming effort of performing time-based system identification, as attempted during the course of this work. Nevertheless, the linear model obtained from the frequency-response transfer function method herein presented is useful as it can replicate with satisfactory accuracy the dynamics of the vehicle, making it possible, for example, to perform autopilot optimization based on the obtained functions.

When it comes to the vehicle design, and as referred multiple times throughout this document, the underlying objective for the development of this novel multi-rotor configuration is the introduction, in a future iteration of the Mini-E aircraft, of the developed tilt-rotor configuration, as to optimize its overall performance by increasing the design L/D ratio and by either reducing the overall weight of the aircraft or enhancing the size of the battery it can carry.

However, even though the devised VTOL configuration is aimed at being introduced in the future version of the Mini-E, the ultimate goal is that it can be used in a larger aircraft (the Eusphyra), of which the Mini-E is a reduced scale model and that will feature an hybrid propulsion system, being this the reason for the initial requirement of having a fixed motor in the rear tilting mechanism. However, the development of such vehicle is progressing in multiple fronts, in a way that the project restrictions may still be changed.

One possible change is in fact related to the propulsion system, where a series hybrid configuration may yet arise, meaning that the aircraft will have an Internal Combustion Engine but that this will no longer be required to power the rear rotor directly. In that case, this subsystem may diverge from the proposed design and culminate in a tilt rotor design where the rear electric motor will be able to rotate jointly with the propeller. While this option would allow for the removal of the gearbox from the

equation, alongside the losses and mass that are associated to it, it will require for other components to be introduced, such as an extra electric motor and associated parts. A trade-off study should be performed at that point in order to determine which option would potentiate the overall efficiency of the system.

The previous investigation may be complemented by a study of the capabilities of the tilting mechanism currently used in the test vehicle. As already referred in section 4.6 of this work, where the relative contribution of this mechanism's mass towards the Mini-E's final MTOM was discussed, it was referred that the current gearbox might be oversized for the current application, with a greater operating efficiency being expected. While this lower efficiency may be due to limitations inherent to the gearbox itself, it can also be associated to an under-loading of the system (2.2). As so, to conclude on this matter, further tests, where loading is increased, can be done, as to determine if the same gearbox could be used for the Mini-E with a lesser loss in efficiency than verified for the test vehicle. If the gearbox is deemed capable and efficiency gains are obtained, the current rear tilting mechanism can be adapted to fit the motor chosen to power the rear rotor of the tri-rotor Mini-E, with the appropriate propeller being fitted to the output shaft. Static thrust tests such as the ones presented in subsection 4.5.1 should then be carried out. In the case of such testing yielding that this lesser efficiency is not due to under-loading the gearbox, but simply to its efficiency being lower than expected, it is also possible to replace the gearbox's gears by a set of higher performance after-market parts that are available for this gearbox model and examine if such modifications are reflected in efficiency gains.

Still on the topic of the rear rotor tilting mechanism, and considering the requirement of this subsystem to not only provide thrust in both vertical and horizontal segments of the aircraft mission but also to do so while drawing mechanical power from an ICE, it would be of interest to assess the possible benefits and downsides of employing a variable pitch propeller system instead of a fixed pitch propeller as used in the test vehicle. This could potentiate not only the performance of the propeller in various flight conditions but also help in the optimization of the engine's efficiency by helping to run it at its most efficient setting. Furthermore, and as verified in the rear tilt mechanism static thrust testing, gearbox efficiency usually increases with loading in a way that the introduction of a variable pitch propeller can also provide an extra degree of control over the gearbox's loading condition and ultimately over its efficiency.

When it comes to the integration of the devised front tilting mechanism into the design of the Mini-E (and of the Eusphyra), it will be necessary to take into account its retracting action. This was considered, alongside other factors, such as having system redundancy, when it was decided to fit each frontal arm with its own servo. This will allow for the separation of the front tilt mechanism support into two separate rotating parts, allowing for the retraction of the arms into the fuselage. This feature was not introduced into the test vehicle as it would not be used, while adding unnecessary weight to the aircraft.

The front rotors can also be modified in order to generate thrust in an upward pusher configuration instead of the current one. Although rotor coverage is reduced, this may provide marginal performance improvements but most importantly generate a more compact design that can more easily be retracted into the aircraft's fuselage.

Bibliography

[1] J. Gertler. U.S. Unmanned Aerial Systems. CRS Report for Congress 7-5700, Congressional Research Service, Jan. 2012.

[2] J. F. Keane and S. S. Carr. A brief history of early unmanned aircraft. *Johns Hopkins Apl Technical Digest*, 32(3):558–571, Dec. 2013.

[3] New Mexico Museum of Space History. Archibald M. Low. URL https://www.nmspacemuseum.org/inductee/archibald-m-low/. Accessed on 2022-04-08.

[4] National Museum of the United States Air Force. Kettering Aerial Torpedo "Bug". URL https://www.nationalmuseum.af.mil/Visit/Museum-Exhibits/Fact-Sheets/Display/Article/198095/kettering-aerial-torpedo-bug/. Accessed on 2022-04-08.

[5] J. G. Leishman. The breguet-richet quad-rotor helicopter of 1907. *Vertiflite*, 47(3):58–60, 2002.

[6] J. D. Blom. *Unmanned Aerial Systems: A Historical Perspective*. Number 37 in Occasional Paper. US Army Combined Arms Center - Fort Leavenworth, Kansas, 2010. ISBN: 978-0-9823283-0-9.

[7] The Editors of Encyclopaedia Britannica. Francis Gary Powers. URL https://www.britannica.com/biography/Francis-Gary-Powers. Accessed on 2022-04-08.

[8] Mine Kafon. Mine kafon airborne demining system. URL https://minekafon.org/. Accessed on 2022-04-08.

[9] A. Momont. Ambulance drone. URL https://www.tudelft.nl/en/ide/research/research-labs/applied-labs/ambulance-drone/. Accessed on 2022-04-08.

[10] G. J. Holland, P. J. Webster, J. A. Curry, G. Tyrell, D. Gauntlett, G. Brett, J. Becker, R. Hoag, and W. Vaglienti. The aerosonde robotic aircraft: A new paradigm for environmental observations. *Bulletin of the American Meteorological Society*, 82(5):889–902, May 2001. doi: 10.1175/1520-0477(2001)082⟨0889:TARAAN⟩2.3.CO;2.

[11] S. Salazar-Cruz, R. Lozano, and J. Escareño. Stabilization and nonlinear control for a novel trirotor mini-aircraft. *Control Engineering Practice*, 17(8):886–894, 2009. ISSN 0967-0661. doi: 10.1016/j.conengprac.2009.02.013. URL https://www.sciencedirect.com/science/article/pii/S0967066109000331.

[12] X. Gu, B. Xian, and J. Li. Model free adaptive control design for a tilt trirotor unmanned aerial vehicle with quaternion feedback: Theory and implementation. *International Journal of Adaptive Control and Signal Processing*, 36(1):122–137, 2022. doi: 10.1002/acs.3344. URL https://onlinelibrary.wiley.com/doi/abs/10.1002/acs.3344.

[13] A. Prach and E. Kayacan. An mpc-based position controller for a tilt-rotor tricopter vtol uav. *Optimal Control Applications and Methods*, 39(1):343–356, 2018. doi: 10.1002/oca.2350. URL https://onlinelibrary.wiley.com/doi/abs/10.1002/oca.2350.

[14] C. Bliamis, I. Zacharakis, and P. K. K. Yakinthos. Aerodynamic and stability analysis of a vtol flying wing uav. *IOP Conference Series: Materials Science and Engineering*, pages 293–297, 2021. doi: 10.1088/1757-899X/1024/1/012039.

[15] B. Sababha, H. Alzubi, and O. Rawashdeh. A rotor-tilt-free tricopter uav: Design, modelling, and stability control. *International Journal of Mechatronics and Automation*, 5:107–113, Dec. 2015. doi: 10.1504/IJMA.2015.075956.

[16] F. Çakici and M. K. Leblebicioğlu. Control system design of a vertical take-off and landing fixed-wing uav. *IFAC-PapersOnLine*, 49(3):267–272, 2016. ISSN 2405-8963. doi: 10.1016/j.ifacol.2016.07.045. URL https://www.sciencedirect.com/science/article/pii/S2405896316302415.

[17] M. Tyan, N. V. Nguyen, S. Kim, and J. W. Lee. Comprehensive preliminary sizing/resizing method for a fixed wing – vtol electric uav. *Aerospace Science and Technology*, 71:30–41, 2017. ISSN 1270-9638. doi: 10.1016/j.ast.2017.09.008. URL https://www.sciencedirect.com/science/article/pii/S1270963817300871.

[18] K. Muraoka, N. Okada, and D. Kubo. *Quad Tilt Wing VTOL UAV: Aerodynamic Characteristics and Prototype Flight*. doi: 10.2514/6.2009-1834. URL https://arc.aiaa.org/doi/abs/10.2514/6.2009-1834.

[19] O. Dündar, M. Bilici, and T. Ünler. Design and performance analyses of a fixed wing battery vtol uav. *Engineering Science and Technology, an International Journal*, 23(5):1182–1193, 2020. ISSN 2215-0986. doi: 10.1016/j.jestch.2020.02.002. URL https://www.sciencedirect.com/science/article/pii/S2215098619316489.

[20] S. Sonkar, P. Kumar, D. Philip, and A. Ghosh. Low-cost smart surveillance and reconnaissance using vtol fixed wing uav. *2020 IEEE Aerospace Conference*, pages 1–7, 2020. doi: 10.1109/AERO47225.2020.9172554.

[21] H. Gu, X. Lyu, Z. Li, S. Shen, and F. Zhang. Development and experimental verification of a hybrid vertical take-off and landing (vtol) unmanned aerial vehicle (uav). *2017 International Conference on Unmanned Aircraft Systems (ICUAS)*, pages 160–169, 2017. doi: 10.1109/ICUAS.2017.7991420.

[22] R. Baránek and F. Šolc. Modelling and control of a hexa-copter. *Proceedings of the 13th International Carpathian Control Conference (ICCC)*, pages 19–23, 2012. doi: 10.1109/CarpathianCC.2012.6228609.

[23] M. Tielin, Y. Chuanguang, G. Wenbiao, X. Zihan, Z. Qinling, and Z. Xiaoou. Analysis of technical characteristics of fixed-wing vtol uav. *2017 IEEE International Conference on Unmanned Systems (ICUS)*, pages 293–297, 2017. doi: 10.1109/ICUS.2017.8278357.

[24] U. Ozdemir, Y. O. Aktas, A. Vuruskan, Y. Dereli, A. F. Tarhan, K. Demirbag, A. Erdem, G. D. Kalaycioglu, I. Ozkol, and G. Inalhan. Design of a commercial hybrid vtol uav system. *Journal of Intelligent Robotic Systems*, 74:371–393, 2014. doi: 10.1007/s10846-013-9900-0.

[25] Dronecode Foundation. PX4 Autopilot. URL `https://px4.io/`. Accessed on 2022-05-17.

[26] M. Kara-Mohamed and A. Lanzon. Design and control of novel tri-rotor uav. *Proceedings of the 2012 UKACC International Conference on Control, CONTROL 2012*, pages 304–309, Sep. 2012. doi: 10.1109/CONTROL.2012.6334647.

[27] S. Pedro. Sizing and integration of an electric propulsion system for a vtol uav. Master's thesis, Instituto Superior Técnico, Dec. 2020.

[28] B. Clavac and Z. Korka. Efficiency investigation on a helical gear transmission. *Analele Universităţii "Eftimie Murgu" Reşiţa, Fascicola Inginerie*, XXIV:pp. 55–66, Oct. 2017.

[29] K. Michaelis, B. R. Hoehn, and M. Hinterstoißer. Influence factors on gearbox power loss. *Industrial Lubrication and Tribology*, 63:46–55, Feb. 2011. doi: 10.1108/00368791111101830.

[30] N. Goudarzi and W. Zhu. Studying the potential of a novel multiple-generator drivetrain in wind energy conversion systems. Volume 4B: Dynamics, Vibration and Control, Nov. 2013. doi: 10.1115/IMECE2013-63017. URL `https://doi.org/10.1115/IMECE2013-63017`.

[31] N. E. Anderson and S. H. Loewenthal. Effect of Geometry and Operating Conditions on Spur Gear System Power Loss. *Journal of Mechanical Design*, 103(1):151–159, Jan. 1981. ISSN 0161-8458. doi: 10.1115/1.3254854. URL `https://doi.org/10.1115/1.3254854`.

[32] M. A. Chowdhury, M. S. Mia, M. Kchaou, M. B. A. Shuvho, and U. K. Debanath. Friction coefficient and performance evaluation of plain journal bearing using sae 5w-30 engine oil. *Proceedings of the Institution of Mechanical Engineers, Part J: Journal of Engineering Tribology*, 234(8):1222–1232, 2020. doi: 10.1177/1350650120903927.

[33] R. P. Sekar. Determination of load dependent gear loss factor on asymmetric spur gear. *Mechanism and Machine Theory*, 135:322–335, 2019. ISSN 0094-114X. doi: 10.1016/j.mechmachtheory.2019.02.011. URL `https://www.sciencedirect.com/science/article/pii/S0094114X19300060`.

[34] F. Wang, X. Xu, J. Xia, and H. Que. Effect of tooth surface modification on dynamic transmission efficiency of double helical gear trains. *International Journal of Acoustics & Vibration*, 26(4), 2021. doi: 10.20855/ijav.2021.26.41793.

[35] F. Lopot, M. Dub, J. Flek, D. Hadraba, M. Havlíček, L. Kučera, O. Štoček, T. Veselỳ, and J. Janáček. Gearbox mechanical efficiency determination by strain gauges direct application. *Applied Sciences*, 11(23):11150, 2021. doi: 10.3390/app112311150.

[36] R. M. Wang, S. R. Zheng, and Y. P. Zheng. 11 - other properties of polymer composites. In *Polymer Matrix Composites and Technology*, Woodhead Publishing Series in Composites Science and Engineering, pages 513–548. Woodhead Publishing, 2011. ISBN 978-0-85709-221-2. doi: 10.1533/9780857092229.3.513. URL https://www.sciencedirect.com/science/article/pii/B9780857092212500114.

[37] G. Ionascu, C. Rizescu, L. Bogatu, L. A. Cartal, and E. Manea. Study of influence of surface microtexture and roughness on friction coefficient. *DEStech Transactions on Engineering and Technology Research*, May 2017. doi: 10.12783/dtetr/icmme2017/9012.

[38] E. M. Almas. Course notes, Machine Elements. Department of Mechanical Engineering, IST, 2020. Accessed on 2022-05-07.

[39] M. B. Tischler and R. K. Remple. *Aircraft and Rotorcraft System Identification - Engineering Methods with Flight Test Examples*. American Institute of Aeronautics and Astronautics, Inc., second edition, 2012. ISBN: 978-1-60086-820-7.

[40] K. Kirkpatrick, J. May, and J. Valasek. Aircraft system identification using artificial neural networks. *51st AIAA Aerospace Sciences Meeting including the New Horizons Forum and Aerospace Exposition 2013*, Jan. 2013. doi: 10.2514/6.2013-878.

[41] Z. Wang, Z. Lyu, D. Duan, and J. Li. A novel system identification algorithm for quad tiltrotor based on neural network with foraging strategy. *Proceedings of the Institution of Mechanical Engineers, Part G: Journal of Aerospace Engineering*, 235(11):1474–1487, 2021. doi: 10.1177/0954410020976598.

[42] W. Wei, M. Tischler, and K. Cohen. System identification and controller optimization of a quadrotor unmanned aerial vehicle in hover. *Journal of the American Helicopter Society*, 62, Oct. 2017. doi: 10.4050/JAHS.62.042007.

[43] W. Wei, M. Tischler, N. Schwartz, and K. Cohen. Frequency-domain system identification and simulation of a quadrotor controller. *AIAA Modeling and Simulation Technologies Conference*, Jan. 2014. doi: 10.2514/6.2014-1342.

[44] D. Tomás. Design, development and manufacture of a new vtol, canard uav. Master's thesis, Instituto Superior Técnico, Dec. 2020.

[45] J. Oliveira. Apontamentos de estabilidade de voo. Department of Mechanical Engineering, IST, 2018. Accessed on 2022-03-23.

[46] W. F. Phillips. *Mechanics of Flight*. Wiley, second edition, Dec. 2009. ISBN: 978-0-470-53975-0.

[47] National Aeronautics and Space Administration (NASA). Drag equation of the early 1900's. URL https://www.grc.nasa.gov/WWW/K-12/airplane/wrights/dragold.html. Accessed on 2022-04-06.

[48] Engineering ToolBox. Drag coefficient, 2004. URL https://www.engineeringtoolbox.com/drag-coefficient-d_627.html. Accessed on 2022-04-06.

[49] J. Roskam. *Airplane Flight Dynamics and Automatic Flight Controls*. Design, Analysis and Research Corporation, third edition, 2001. ISBN: 1-884885-17-9.

[50] Holybro. Pixhawk 4, May 2018. URL http://www.holybro.com/product/pixhawk-4/. Accessed on 2022-05-17.

[51] Dronecode Project. QGroundControl, 2019. URL http://qgroundcontrol.com/. Accessed on 2022-05-17.

[52] Dronecode Project. Airframes reference. URL https://dev.px4.io/master/en/airframes/airframe_reference.html. Accessed on 2022-05-17.

[53] Dronecode Project. PX4 Autopilot User Guide (v1.12), Jul. 2021. URL https://docs.px4.io/v1.12/en/. Accessed on 2022-05-17.

[54] AeroTéc. UAV - Alameda Research Team, 2022. URL https://aerotec.pt/uav. Accessed on 2022-07-16.

[55] iFlight. XING X1404 Toothpick Ultralight Build (unibell). URL https://shop.iflight-rc.com/quad-parts-cat20/motors-cat26/xing-motors-cat148/xing-x1404-toothpick-ultralight-build-unibell-pro895. Accessed on 2022-04-19.

[56] Gemfan. 4024-2 Toothpick Props. URL https://www.gemfanhobby.com/show.aspx?id=267&cid=46. Accessed on 2022-04-19.

[57] T-Motor. AIR 20A 4S. URL https://store.tmotor.com/goods.php?id=376. Accessed on 2022-04-19.

[58] iFlight. XING 2806.5 FPV Cinelifiter Motor. URL https://shop.iflight-rc.com/xing-x2806-5-fpv-nextgen-motor-pro1001. Accessed on 2022-04-19.

[59] Gemfan. Flash 7040-3. URL https://www.gemfanhobby.com/show.aspx?id=218&cid=49. Accessed on 2022-04-19.

[60] T-Motor. T 80A. URL https://store.tmotor.com/goods.php?id=376. Accessed on 2022-04-19.

[61] Engineering ToolBox. Friction - friction coefficients and calculator, 2004. URL https://www.engineeringtoolbox.com/drag-coefficient-d_627.html. Accessed on 2022-05-07.

[62] F. Moleiro. Course notes, Aircraft Structures. Department of Mechanical Engineering, IST, 2021. Accessed on 2022-05-04.

[63] RG Faserverbundwerkstoffe - Composite Technology. Carbon fibre tubes pultruded, 2022. URL http://www.ezentrumbilder.de/rg/pdf/td_en_740908SKZ.pdf. Accessed on 2022-05-04.

[64] S. Swanson, M. Messick, and G. Toombes. Comparison of torsion tube and iosipescu in-plane shear test results for a carbon fibre-reinforced epoxy composite. *Composites*, 16(3):220–224, 1985. ISSN 0010-4361. doi: 10.1016/0010-4361(85)90605-6. URL https://www.sciencedirect.com/science/article/pii/0010436185906056.

[65] Align TRex Helis. Align Dominator T-Rex 700X, 2018. URL https://aligntrexhelis.com/t-rex-helis/700-helis/t-rex-700x-super-combo. Accessed on 2022-05-07.

[66] TYTO Robotics. Series 1580 test stand - dynamometer for drone propulsion systems, 2022. URL https://www.tytorobotics.com/pages/series-1580-1585. Accessed on 2022-05-14.

[67] National Instruments Corp. What Is LabVIEW?, 2022. URL https://www.ni.com/pt-pt/shop/labview.html. Accessed on 2022-05-14.

[68] P. Zhou, D. Lin, Y. Xiao, N. Lambert, and M. A. Rahman. Temperature-dependent demagnetization model of permanent magnets for finite element analysis. *IEEE Transactions on Magnetics*, 48(2): 1031–1034, 2012. doi: 10.1109/TMAG.2011.2172395.

[69] S. Ruoho, J. Kolehmainen, J. Ikaheimo, and A. Arkkio. Interdependence of demagnetization, loading, and temperature rise in a permanent-magnet synchronous motor. *IEEE Transactions on Magnetics*, 46(3):949–953, 2010. doi: 10.1109/TMAG.2009.2033592.

[70] K. Mao, W. Li, C. Hooke, and D. Walton. Friction and wear behaviour of acetal and nylon gears. *17th International Conference on Wear of Materials*, 267(1):639–645, 2009. ISSN 0043-1648. doi: 10.1016/j.wear.2008.10.005. URL https://www.sciencedirect.com/science/article/pii/S0043164809001501.

[71] B. Mettler, M. B. Tischler, and T. Kanade. System identification of small-size unmanned helicopter dynamics. *Annual Forum Proceedings- American Helicopter Society*, 2:1706–1717, 1999.

[72] MathWorks®. tfest - estimate transfer functions, . URL https://www.mathworks.com/help/ident/ref/tfest.html. Accessed on 2022-08-01.

[73] MathWorks®. compare - compare identified model output and measured output, . URL https://www.mathworks.com/help/ident/ref/compare.html. Accessed on 2022-08-01.

Appendix A

Custom PX4 Files

A.1 Configuration File

```
#!/bin/sh
#
# @name Front Tilt Tricopter Y+ Geometry
# @type Tricopter Y+
# @class Copter
#
# @output MAIN1 motor 1
# @output MAIN2 motor 2
# @output MAIN3 motor 3
# @output MAIN4 yaw servo
#
# @maintainer Ant nio Arco
#
# @board bitcraze_crazyflie exclude
# @board px4_fmu-v2 exclude

. ${R}etc/init.d/rc.mc_defaults

# MAV_TYPE_TRICOPTER 15
param set-default MAV_TYPE 15

set MIXER tri_yft_yaw+
```

A.2 Mixer File

```
# Front Tilt Tricopter Y+ Configuration Mixer
# Yaw Servo +Output ==> +Yaw Vehicle Rotation

# Motors
R: 3fty

# Yaw Servo
M: 1
S: 0 2  10000  10000      0 -10000  10000
```

A.3 Geometry File

```
# Tri Front Tilt Y

[info]
key = "3fty"
description = "Tri Front Tilt Y"

[rotor_default]
axis      = [0.0, 0.0, -1.0]
Ct        = 1.0
Cm        = 0.0
direction = "CCW"

[[rotors]]
name      = "front_right"
position  = [0.32836, 0.20704, 0.0]

[[rotors]]
name      = "front_left"
position  = [0.32836, -0.20704, 0.0]

[[rotors]]
axis      = [0.0, 0.0, -1.0]
Ct        = 5.2
Cm        = 0.0
direction = "CW"
name      = "rear"
position  = [-0.1407, 0.0, 0.0]
```

Appendix B

Actuation Matrix ($\mathbb{B}$)

$$
\begin{bmatrix}
-2k_{T_1}\Omega_{0_1}\sin\delta_{arms_0}\cos\Gamma & 2k_{T_2}\Omega_{0_2}\sin\delta_{arms_0}\cos\Gamma \\
2k_{T_1}\Omega_{0_1}\sin\delta_{arms_0}\sin\Gamma & 2k_{T_2}\Omega_{0_2}\sin\delta_{arms_0}\sin\Gamma \\
-2k_{T_1}\Omega_{0_1}\cos\delta_{arms_0} & -2k_{T_2}\Omega_{0_2}\cos\delta_{arms_0} \\
-2k_{T_1}\Omega_{0_1}y_f\cos\delta_{arms_0}+2k_{\tau_1}\Omega_{0_1}\sin\delta_{arms_0}\cos\Gamma & 2k_{T_2}\Omega_{0_2}y_f\cos\delta_{arms_0}-2k_{\tau_2}\Omega_{0_2}\sin\delta_{arms_0}\cos\Gamma \\
2k_{T_1}\Omega_{0_1}x_f\cos\delta_{arms_0}-2k_{\tau_1}\Omega_{0_1}\sin\delta_{arms_0}\sin\Gamma & 2k_{T_2}\Omega_{0_2}x_f\cos\delta_{arms_0}-2k_{\tau_2}\Omega_{0_2}\sin\delta_{arms_0}\sin\Gamma \\
2k_{T_1}\Omega_{0_1}x_f\sin\delta_{arms_0}\sin\Gamma+2k_{T_1}\Omega_{0_1}y_f\sin\delta_{arms_0}\cos\Gamma+2k_{\tau_1}\Omega_{0_1}\cos\delta_{arms_0} & 2k_{T_2}\Omega_{0_2}x_f\sin\delta_{arms_0}\sin\Gamma+2k_{T_2}\Omega_{0_2}y_f\sin\delta_{arms_0}\cos\Gamma+2k_{\tau_2}\Omega_{0_2}\cos\delta_{arms_0}
\end{bmatrix}
\tag{B.1}
$$

$$
\begin{bmatrix}
2k_{T_3}\Omega_{0_3}\cos\mu & (-k_{T_1}\Omega_{0_1}^2+k_{T_2}\Omega_{0_2}^2)\cos\delta_{arms_0}\cos\Gamma \\
0 & (k_{T_1}\Omega_{0_1}^2+k_{T_2}\Omega_{0_2}^2)\cos\delta_{arms_0}\sin\Gamma \\
-2k_{T_3}\Omega_{0_3}\sin\mu & (k_{T_1}\Omega_{0_1}^2+k_{T_2}\Omega_{0_2}^2)\sin\delta_{arms_0} \\
2k_{\tau_3}\Omega_{0_3}\cos\mu & (k_{T_1}\Omega_{0_1}^2-k_{T_2}\Omega_{0_2}^2)y_f\sin\delta_{arms_0}+(k_{\tau_1}\Omega_{0_1}^2-k_{\tau_2}\Omega_{0_2}^2)\cos\delta_{arms_0}\cos\Gamma \\
-2k_{_3}\Omega_{0_3}x_r\sin\mu & -(k_{T_1}\Omega_{0_1}^2+k_{T_2}\Omega_{0_2}^2)x_f\sin\delta_{arms_0}-(k_{\tau_1}\Omega_{0_1}^2+k_{\tau_2}\Omega_{0_2}^2)\cos\delta_{arms_0}\sin\Gamma \\
-2k_{\tau_3}\Omega_{0_3}\sin\mu & (k_{T_1}\Omega_{0_1}^2+k_{T_2}\Omega_{0_2}^2)x_f\cos\delta_{arms_0}\sin\Gamma+(k_{T_1}\Omega_{0_1}^2+k_{T_2}\Omega_{0_2}^2)y_f\cos\delta_{arms_0}\cos\Gamma-(k_{\tau_1}\Omega_{0_1}^2+k_{\tau_2}\Omega_{0_2}^2)\sin\delta_{arms_0}
\end{bmatrix}
$$

Appendix C

Validation flight data

C.1 Rates Setpoints and Respective Responses

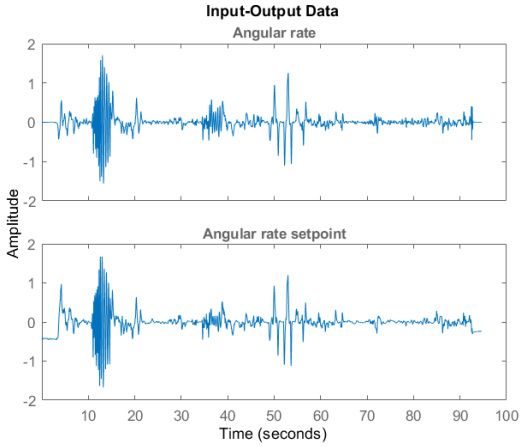

(a) Roll axis

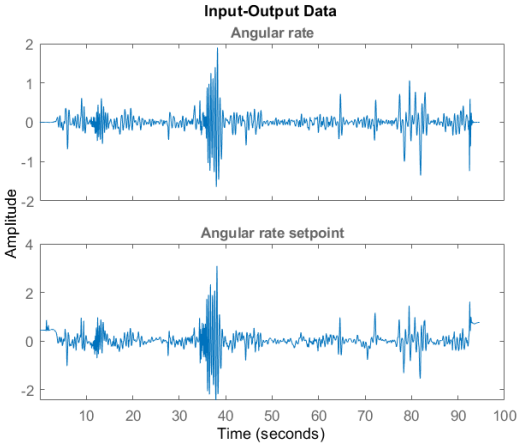

(b) Pitch axis

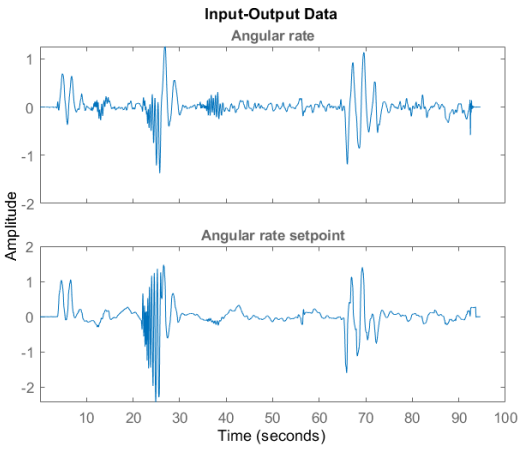

(c) Yaw axis

Figure C.1: Rates setpoints and responses along the various axis during the validation test flight.